Label-Free Studies of Single Biological Nanoparticles Using Optical Nanotweezers

by

Matthew Peters
B.Eng. Electrical Engineering, University of Victoria, 2022

A thesis Submitted in Partial Fulfillment of the
Requirements for the Degree of

Master of Applied Science

in the Department of Electrical Engineering

Label-Free Studies of Single Biological Nanoparticles Using Optical Nanotweezers

by

Matthew Peters
B.Eng. Electrical Engineering, University of Victoria, 2022

Supervisory Committee

Dr. R. Gordon, Supervisor
(Department of Electrical Engineering)

Dr. L. Smith, Departmental Member
(Department of Electrical Engineering)

Supervisory Committee

Dr. R. Gordon, Supervisor
(Department of Electrical Engineering)

Dr. L. Smith, Departmental Member
(Department of Electrical Engineering)

ABSTRACT

This thesis has two parts. In the first, we demonstrated tracking and imaging of single proteins without a fluorescent label or tether, well below the previously achieved smallest protein. This result made use of interference effects similar to interferometric scattering microscopy, with additional interference enhancement from the enhanced electromagnetic field. We use the tracking to obtain a single proteins velocity and size the protein. In the second part, we explored the use of optical scattering from an unlabelled. single extracellular vesicle to be used for cancer diagnostics. We trained a 1D-convolutional neural network using the transmission signal of an extracellular vesicle trapped in a double nanohole. We achieved a greater than 90% accuracy in classifying an extracellular vesicle with its parent cell. Three different parent cells were used, MCF10A (non-malignant), MCF7 (non-invasive, cancerous), and MDA-MB-231 (invasive, cancerous).

Contents

List of Tables

List of Figures

ACKNOWLEDGEMENTS

I would like to thank most of all my supervisor **Dr. Reuven Gordon** for allowing me the opportunity to volunteer in the lab as an undergraduate student and continue with my master's.

I am grateful to the members of the Nanoplasmonics Lab for their collaborations and discussions, and for teaching me Farsi and sharing their food with me. **Dr. Elham Babaei, Amrita Pati, Elham Hosseini, Behnam Khosravi, Sherin George, and Annie Yang**.

Thank you to **Dr. Mirali Seyed Shariatdoust** for sitting patiently with me as an undergraduate while I inundated you with questions and guiding me in PhD admissions.

Thank you most of all to **Dr. Demelza Wright** for teaching me something new everyday, for always making time for my questions and ideas, for giving me helpful advice for my future, and for being a friend.

I would like to thank: **my buddies Jordan, Matt Fred, Sabby, Mason, Emilio, John, Jax, Anubhav, George, Jackson, Colton, Jerry, Josh, Osama, George, Alexei, and Buba**, my friends **Ali and Kelly** for being voices of reason, **Hannah and Lily** for bringing a smile to my face everyday, the people in Victoria that made my life so much better **Brooke and Ana**, my lacrosse friends **Taylor, Bridgitte, and Brendan**, and my roommate **Adam** for making my life in Victoria more enjoyable.

Lastly I would like to thank **PUP**, **Alvvays**, **Ethel Cain**, **Phoebe Bridgers**, and **The Marias** for blessing my ears during the long days.

DEDICATION

To the future members of the Nanoplasmonics Lab, I wish you luck, and hope you find something useful in here.

If I could give you advice to succeed, take charge of your work, be passionate, and be endlessly curious.

Chapter 1

Introduction

1.1 Motivation for Thesis

Understanding molecular mechanisms of proteins and other biomolecules remains a challenge for researchers. Synthesis, folding, and interactions are all integral to life, but these events are heterogeneous in nature. By measuring ensembles of proteins, this heterogeneity is averaged out and crucial details about mechanisms are lost. Most single biomolecule measurements thus far have been enabled by the addition of a fluorescent label. While this effectively highlights the biomolecule of interest, it perturbs the native structure of the biomolecule and results could differ from the native state of the molecule. Label-free methods have been developed to overcome fluorescent limitations but diverse applications are yet to be widely demonstrated. This thesis aims to present two markedly different applications of label-free, single molecule studies.

1.1.1 Label-Free Imaging and Tracking of Proteins

Among optical methods of studying biomolecules, fluorescence has been the dominant approach for seeing the particle of interest. Of particular interest are videos of proteins as this can provide much more information than static shots. The use of fluorescence has allowed for researchers to achieve particle tracking, structural information, conformational dynamics, and interactions with other biomolecules; however, fluorescent labels modify the protein from its native state and thus these results may

not be wholly accurate. Some progress has been made using interference imaging to observe proteins without fluorescence but has typically been limited to larger proteins and is unable to track their movement without an alternative label, such as a gold nanoparticle. There is a significant need to push the detection limit of unlabelled proteins to below 30 kDa and expand capabilities to diffusion tracking to obtain information about entirely native proteins.

1.1.2 Identifying Cancer Through Unlabelled, Single Extracellular Vesicles

A major challenge in cancer prognostics is finding early biomarkers that can accurately identify cancer. Circulating tumor cells are rare and circulating tumor DNA cannot provide information about the originating cell. Extracellular vesicles contain cell specific information, are abundant in fluids, and have unique properties between cancerous and non-cancerous. Fluorescence measurements have limitations relating to observation times and structural modifications, so a label-free approach that is highly specific at the single EV level is desirable.

1.2 Organization of Thesis

Chapter 2 discusses a background on single molecule techniques and single protein imaging present in research today with their advantages and disadvantages. Theory behind plasmonics, optical tweezers, and subwavelength apertures is discussed.

Chapter 3 reviews the methods of fabricating double nanohole gold samples for trapping, making solutions for trapping, setting up an optical tweezer system, and how to operate the system for successful trapping. Information on computer vision techniques used is presented as well.

Chapter 4 presents and discusses the results of my work for imaging single proteins without fluorescence and sizing them through diffusion.

Chapter 5 shows the use of double nanohole optical tweezers and a convolutional neural network for classifying singly trapped extracellular vesicles based on their parent cell.

Chapter 6 highlights two other projects I was a part of during my time in the

Nanoplasmonics Lab. The first, pulse laser trapping, discusses the need for finding vibrational modes of proteins, the new approach, the current literature, and the results. The second, quantum corrected surface plasmon polariton propagation length, attempts to reason why theory and experiment differ when it comes to surface plasmon polariton propagation length on ultrasmooth silver surfaces.

Chapter 7 concludes this thesis and discusses the future work.

1.3 Author's Contribution

The work presented in "Chapter 4 - Label-free tracking of proteins through plasmon enhanced interference" was published in ACS Nanoscience Au under CC BY-NC-ND 4.0 DEED.

Matthew Peters, Declan McIntosh, Alexandra Branzan Albu, Cuifeng Ying, and Reuven Gordon ACS Nanoscience Au 2024 4 (1), 69-75 DOI: 10.1021/acsnanoscienceau.3c00045

M.P. devised and performed experiments, data analysis, and wrote the manuscript. D.M. provided advice on computer vision. A.B.A. provided advice on computer vision. C.Y. assisted in interpreting results and writing the manuscript. R.G. advised on experiments, analysis, and writing the manuscript.

The work presented in "Chapter 5 - Classification of cancerous and non-cancerous single extracellular vesicles using a convolutional neural network and double nanohole optical tweezers" was submitted to the Journal of Physics: Photonics.

M.P. performed experiments and data analysis, and wrote the manuscript. S.H. prepared the extracellular vesicles, performed nanoparticle tracking analysis, flow cytometry, and western blots, and contributed to the manuscript. T.Z. developed the convolutional neural network and assisted in writing the manuscript. A.Y.S. assisted in data analysis and figure preparation. K.C.W. advised on extracellular vesicle preparation and analysis. R.G. advised on experiments and analysis and contributed to the manuscript.

Chapter 2

Background

2.1 Introduction

This chapter will introduce different techniques of single molecule imaging section 2.2.
Optical tweezing will be reviewed in Section 2.3.
In Section 2.4, subwavelength apertures are discussed.

These sections provide the relevant background information and motivation for studying single protein dynamics in a nanoaperture optical trap.

2.2 Single Molecule Imaging and Studies

Obstructed by collective averaging, biologists needed to develop techniques to observe and measure single biomolecules. Many biological processes are governed by heterogeneous events that requires researchers to observe these behaviour distributions. Many different techniques have been created to aid our understanding of biological processes: single molecule fluorescence, total internal reflection, protein labelling, single molecule Förster resonance energy transfer, super resolution microscopy interferometric scattering, plasmonic scattering microscopy, and nanofluidic scattering microscopy are some of the most popular techniques relying on visual information [22, 23, 24, 25, 26, 27, 28, 10, 29]. Alternatively, protein and small molecule

measurements have been made possible by nuclear magnetic resonance spectroscopy (NMR), Fourier transformed infrared spectroscopy (FTIR), and Hydrogen-Deuterium exchange mass spectrometry [30, 31, 32]. These techniques do not give images of the biomolecules of interest but do provide great insight into structure and dynamics. These are often ensemble measurements to improve the signal-to-noise ratio (SNR), which, as mentioned before, hides the heterogeneity of many molecules. A brief look at two popular methods of studying proteins and cells is given here.

2.2.1 Super Resolution Microscopy

Conventional light microscopy is hindered by the diffraction limit that causes two objects separated by less than 200 nm to appear as one object [33]. It is possible to overcome this resolution limit through super resolution microscopy in stochastic or targeted schemes. Fluorescent labelling allows light microscopes to highlight specific biomolecules of interest, while fluorescence has drawbacks, it has enabled light nanoscopy. A fluorescent molecule has a ground state and an excited state, when a laser of a specific wavelength is shone on it, the ground state is excited and fluoresces. Importantly, the atoms of the fluorescent molecule wiggle when excited and the photon is red-shifted slightly, which allows for the elimination of the excitation wavelength when imaging [34]. As Dr. Stefan W. Hell described in his Nobel lecture, the issue comes from conventional optical lenses focus light only as tight as 200nm [34]. To overcome this, some of the molecules are kept in a non-signalling state so that the detector does not get overwhelmed. Since all the molecules will be excited at the same time by the excitation laser, a stimulated emission laser is introduced to deplete certain fluorophores. Giving rise to stimulated emission depletion microscopy (STED), where the depletion laser has a longer wavelength. The beam is modified so that it has a ring shape with decreasing intensity towards the center, turning off the fluorophores everywhere but the center [34]. Stochastic optical reconstruction microscopy and photoactivated localization microscopy operate by the stochastic switching on and off of fluorophores and acquiring sequential images [35]. Super resolution microscopy is a fantastic technique, recognized with the Nobel prize; however, it still has its disadvantages in using fluorophores. Label-free techniques are beneficial as they do not modify the biomolecule of interest in a way that could affect conformation, binding sites, steric hindrance, and in some cases there are not any suitable labels [36] and overcome issues with photoblinking and bleaching [37].

2.2.2 Interferometric Scattering (iSCAT)

Alternatively, all nanoparticles biological or not, scatter light proportional to the incident light intensity and scattering cross section. Photon flux in fluorescent imaging techniques is limited by saturation of the fluorophores, in this case, there is an endless supply of photons to scatter and detect. With no background medium, this would be a perfect solution to the problems with fluorescent techniques. In reality, biomolecules are in solution when being imaged. Kukura et al. state that for a large silica bead (160 nm), a 532 nm laser with beam size of 3×10^{-10} cm^2 results in only 1% of photons being scattered by the particle [37]. Dark field microscopy allows for a simple way to increase the signal-to-noise ratio where only the scattered light is collected. Alternatively, a total internal reflection prism can be used that creates an exponentially decaying field that scatters light from particles within 100 nm of the surface [37]. The basic principle of iSCAT is that a reference beam is superimposed with the scattered light of the sample. The coverslip can thus be used to provide the reference beam and can be averaged out using a median filter. Overall this technique provides a strong method of single protein imaging down to 40kDa (with anomaly detection this has been pushed to 9 kDa), but **over half of the human proteome is below 35 kDa [38]**.

2.2.2.1 Scattering as Detection

Scattering efficiency depends on the interaction between the light and the nanoparticle. Given that we are working in the Rayleigh regime, the scattered field is given by $E_s = |s|e^{i\phi}E_i$ and scales with the polarizability (α) of the particle, ϕ in this case is the phase of the scattered light. The scattering amplitude is given by Kukura [37] and is written as:

$$s(\lambda) = \eta\alpha(\lambda) = \eta\varepsilon_d(\lambda)\pi\frac{D^3}{2}\frac{\varepsilon_p(\lambda) - \varepsilon_d(\lambda)}{\varepsilon_p(\lambda) + 2\varepsilon_d(\lambda)}, \tag{2.1}$$

where $\varepsilon_{d/p}$ refers to the medium or the particle dielectric constants, D is diameter of the particle, and η is a constant that accounts for detection efficiency.

The detected intensity is thus given by,

$$I_{det} = |E_b + E_s|^2 = |E_i|^2(b^2 + |s|^2 - 2b|s|\sin(\phi)) \tag{2.2}$$

where E_b describes the background field and $|E_i|^2 b^2$ the background intensity. It can be seen from this that even with most of the incident light intensity suppressed, detection is still limited by background scattering from the surface.

This issue has somewhat been resolved by interferometric techniques that replace the background light field by the reflected light field.

$$I_{det} = |E_r + E_s|^2 = |E_i|^2(r^2 + |s|^2 - 2r|s|\sin(\phi)) \tag{2.3}$$

A glass-water interface has an r approximately 0.065 which is much greater than $|s|$ for particles less than 50nm in diameter. The signal contrast is then given by

$$\frac{I_{particle}}{I_{background}} = 1 - \frac{2r|s|\sin(\phi)}{r^2}. \tag{2.4}$$

The key result here is that the signal contrast scales linearly with scattering amplitude, or the particle volume and makes detection of smaller particles possible [37].

The results here are directly applicable to the camera recordings seen in our optical nanotweezers work. Although we replace a glass/water interface with a gold/water interface that leads to a significantly higher reflected signal. This reflected signal overpowers the surface imperfections that dominate the iSCAT noise, so we are just left with a constant laser noise that can be averaged out.

2.2.3 Plasmonic Scattering Microscopy

Plasmonic scattering microscopy (PSM) has been shown to image non-specific single protein binding using interference from surface plasmon resonance sensors and analytes [10]. The evanescent field only extends $\simeq$100 nm away from the surface so bulk impurities in solution do not affect the imaged results, and images the transmitted signal to avoid the strong reflection from the gold surface. Currently, this has been shown to image binding of a 66 kDa protein in solution, but is unable to track its diffusion [39, 40, 41]. PSM excites surface plasmon waves using angled light through

an oil-immersion objective onto a gold coated glass slide. Surface plasmon resonance microscopy is described by

$$I \approxeq |E_p + E_s + E_r|^2, \tag{2.5}$$

where E_p is the excited plasmonic wave, E_s is the scattering of the plasmonic wave from a protein, and E_r is the reflection of the incident wave. The image contrast is given by interference from the E_p and E_s terms, $2|E_p||E_s|\cos(\theta)$, where θ is the phase difference between the two. However, E_r creates a large background signal that masks the weak scattering from the stationary protein. To combat this issue, PSM utilizes an objective placed above the sample where a camera can see the scattering. PSM intensity is given by

$$I \approxeq |E_b|^2 + 2|E_b||E_s|\cos(\beta) + |E_s|^2, \tag{2.6}$$

where β is the phase difference between the scattering from the protein and gold surface and E_b is the background scattering from nanoscale roughness on the gold surface. Similar to other evanescent imaging techniques, the scattering pattern is notably more complex than an airy disk. Differential imaging provides the necessary background removal to highlight the protein binding events [10].

2.2.4 Nanofluidic Scattering Microscopy

Nanofluidic scattering microscopy (NSM) utilizes subwavelength channels combined with dark-field microscopy to track the diffusion of single proteins through interference with the channel. This method is able to size single proteins using the optical contrast of a differential image and demonstrates tracking down to 66 kDa [29]. Nanofluidic channels are fabricated into an optically transparent material, the length of the channel exceeds the microscope field-of-view, but the width is variable depending on the biomolecule of interest. Considering a single biomolecule diffusing through a nanochannel, both the biomolecule and channel scatter light coherently into the collection optics with intensity $I_t = \frac{cI_0L|\alpha_t|^2k^3}{4}$, depending on the incident light intensity (I_0), wavenumber of the light (k), length of illuminated part of the nanochannel (L), collection efficiency (c), and optical properties of the biomolecules and nanochannel (α_t) [29]. This technique seems to have been the first to directly track unmodified

proteins diffusing in solution, albeit in a confined geometry.

2.2.5 Label Free Single Molecule Studies Motivation

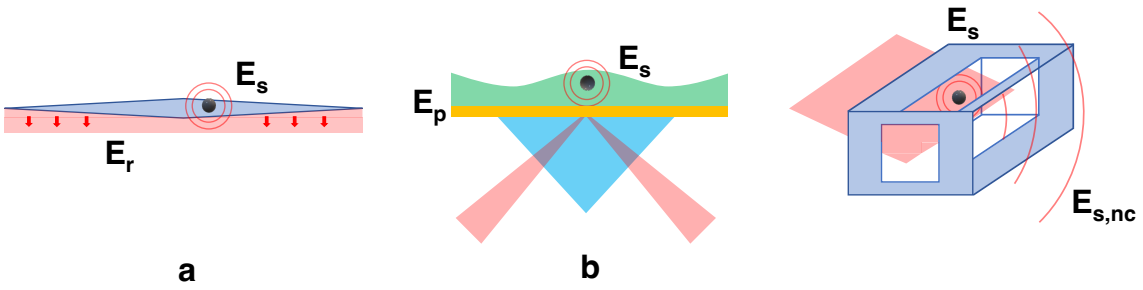

Figure 2.1: Schematic representations of (a) iSCAT, (b) PSM, and (c) NSM. E_s is the scattered field from protein, E_r is the reflected field, E_p is the plasmonic field, and $E_{s,nc}$ is the scattering from nanochannel.

Optical scattering methods, schematically represented in Figure 2.1, all have great benefits with proven track records for studying biomolecules down to the single protein level. But all are limited in some form: whether it is labelling for tracking, ensemble measurements, low SNR, size limits, or diffraction limits restrict the use cases.

2.3 Optical Tweezers

Single-molecule studies were born out of a desire to understand behaviours of molecules in real time and without averaging over an ensemble. Optical tweezers have become a popular method of performing single-molecule experiments since it's invention in 1986 by Arthur Ashkin [42]. The single-beam optical tweezer utilized a tightly focused laser beam to hold dielectric particles in three dimensions [42]. The Gaussian profile of the laser beam causes the particle to be pulled back to the point of highest intensity. A year later, Ashkin demonstrated tweezing of bacteria, cells, and organelles [43, 44]. He used infrared (IR) light to reduce the optical damage and showed *Escherichia coli* and yeast reproduction [44].

The theory behind optical tweezing is governed by the fact that photons carry energy, linear momentum, and angular momentum, resulting in two forces exerted on an object: scattering and gradient forces. The direction of the scattering force is in

the direction of laser propagation whereas the gradient force acts in the direction of the field intensity gradient. For particles in the Rayleigh regime ($r << \lambda$), the electrical dipole model can be used and the response of the particle to an electric field is characterized by a polarizability (α). The Lorentz force is a measure of the force acting on a single point charge in a magnetic and electric field

$$F = (\mathbf{p} \cdot \nabla)\mathbf{E} + \frac{d\mathbf{p}}{dt} \times \mathbf{B}, \tag{2.7}$$

where $\mathbf{F}$ is the force, $\mathbf{E}$ is the electric field, $\mathbf{B}$ the magnetic field, and $\mathbf{p}$ is the dipole moment.

Through the use of polarizability, the dipole moment can be defined as $\mathbf{p} = \alpha\mathbf{E}$ and equation 2.7 can be redefined as follows

$$F = \alpha(\mathbf{E} \cdot \nabla)\mathbf{E} + \alpha\frac{d\mathbf{E}}{dt} \times \mathbf{B}, \tag{2.8}$$

where the polarizability α is shown in equation 2.9, assuming a spherical particle with radius r and refractive index n_p with a background medium n_m [45].

$$\alpha = (\frac{n_p^2 - n_m^2}{n_p^2 + 2n_m^2})n_m^2 r^3 \tag{2.9}$$

This leads us to the gradient force acting on the particle shown in equation 2.10.

$$F_{grad} = \frac{1}{2}\alpha\nabla E^2 \tag{2.10}$$

The E^2 term represents the intensity of the photons from the laser and thus the strongest force will occur where the photon intensity is the highest, i.e. the waist of the focused beam and the particle is attracted to the center of the beam [46].

The scattering force acts against the gradient force resulting in the trap position being slightly below the maximum intensity of the focused laser [45].

$$F_{scat} = \frac{I_0}{c}\frac{128\pi^5 r^6}{3\lambda^4}(\frac{n_p^2 - n_m^2}{n_p^2 + 2n_m^2})^2 n_b \tag{2.11}$$

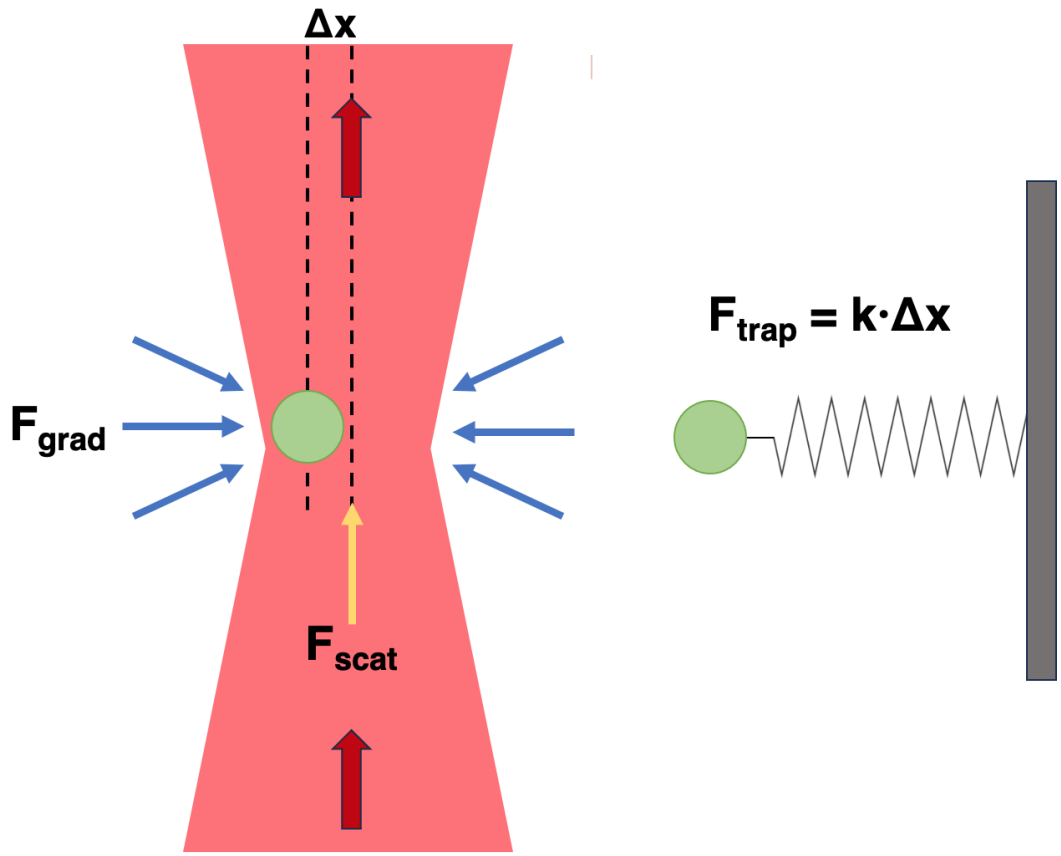

Figure 2.2: Scattering and gradient force acting on a dielectric particle trapped in a focused laser beam with the equivalent model of the trapping forces using Hooke's law.

By looking at equations 2.10 and 2.11, we can see that the scattering force will decay significantly faster than the gradient force as the particle gets smaller. A third force can be considered in optical trapping as well: Stokes' Law gives the force on a sphere of radius r moving through a fluid with viscosity η at speed v and is directly proportional to the radius of the particle [47].

$$F_{stokes} = 6\pi r\eta v \tag{2.12}$$

As the size of the particle becomes sufficiently small, the forces acting to trap the particle become too weak. The thermal motion of the particle increases with decreasing size creating a reduction in the viscous drag or the Stokes force. This presents three solutions: increasing laser power, attaching the particle of interest to a larger

particle, or generate a larger gradient force through nanostructures.

Increasing the laser power is not a viable approach for biological particles as this can damage the particle, or in the biological case, kill it. The second solution is a widely used method of indirectly studying small particles. In 1990, Block et al. demonstrated function of single kinesin proteins by coating a silica bead with a protein and manipulating the bead near a microtubule [48]. In 1997, force-extension relationships were measured for DNA under various buffer conditions, the DNA was immobilized to a glass coverslip on one end and the other attached to a microscopic bead. A piezo stage was then used to stretch the DNA while recording the position of the bead [49]. Numerous examples of optical tweezers studying individual proteins, DNA, and RNA molecules are present in the literature [50, 51, 52, 53, 54, 55, 56, 56, 57]. However, trapping of individual proteins with a laser has proven to be difficult due to their small size (1-50nm) in relation to the beam size and power needed from optical tweezers. By adding a nanostructure into the laser path, a self induced back action effect is added that, when a particle is trapped, changes the surrounding field to enhance the trap [58, 59]. This work proposed a double nanohole in a gold film to enhance trapping of 12nm silica nanospheres.

2.4 Subwavelength Apertures

Generally, subwavelength optics studies the interactions of electromagnetic waves with objects that are smaller than half the wavelength. Lord Rayleigh showed that there is a cut-off condition exists where there is no propagation of light [60]. This cut-off is derived from the boundary conditions of EM field within the hole, and below cut-off, the boundary conditions can not be satisfied. Bethe expanded on this and showed that transmission decreases as a ratio of radius to wavelength [61]. Using a quasi-static approach, we can assume that the spatial variation of the field is much faster than the temporal variation and can neglect the time dependence. The conditions for this problem are as follows: a circular hole in an infinite perfect electric conductor (PEC) with diameter significantly smaller than the wavelength, the plane wave is normally incident to the PEC and the electric and magnetic fields parallel to the PEC. With these conditions, the diffracted light can be approximated as the emission of a magnetic dipole. By solving the boundary conditions of the magnetic potential at both sides of the PEC, the transmitted power in free space can be described as:

$$T = \frac{1}{2}\frac{4Z_0\pi^3}{3\lambda^4}(\frac{8r^3H_0}{3})^2 \propto \frac{r^6}{\lambda^4}, \tag{2.13}$$

where Z_0 is the free-space impedance, r is the hole radius, λ is the free-space wavelength, and H_0 is the magnetic field of the incident wave.

The area of a circle is given by πr^2, so after normalizing the transmission we conclude that $T \propto (\frac{r}{\lambda})^4$.

Extraordinary optical transmission (EOT) is a phenomenon where a subwavelength aperture in an opaque film transmits more light than expected and is counter to Bethe's aperture theory. This was discovered by Ebbessen et al. in 1998 where they demonstrate a greater than 2x transmission of light in a silver film with periodic holes varied from 150nm to 1μm with spacing between 0.6 and 1.8μm [62]. This is in contradiction to Bethe's theory that predicts transmission efficiency to scale as $(\frac{r}{\lambda})^4$, indicating the array is an active element in the transmission of light. This can be described by resonant coupling to surface plasmon modes on the surface of the metal [63].

2.4.1 Aperture Shapes

The previous section generally focused on simple circular holes on an infinitely thin PEC. In reality, there is a finite thickness and different materials have different properties that affect the transmission. In addition to materials, the shape of the aperture can greatly affect the transmission properties and cut-off wavelengths. Nano-optical tweezers have become a great tool in single protein studies as they enable direct measurement of individual proteins down to 4kDa [4]. Nanostructures are added to the tweezing laser path to create a subwavelength trapping volume, greatly increasing the gradient force. Current researchers use a variety of metallic, generally gold, nanostructures such as double nanopyramids, double nanoholes, bowties, coaxial apertures, single and double nanopillars, and photonic crystal resonators [64].

2.4.2 Self Induced Back Action Tweezing

Gordon and Quidant et al. proposed a form of optical tweezing that has the trapped particle play an active role in stability of the trap. They proposed and demonstrated that a nanostructure in a metal film near its cut-off resonance provides superior

trapping for particles in the Rayleigh regime. If the dielectric medium changes near the aperture, the equivalent wavelength is altered by a factor of 1/n, therefore a larger transmission is expected.

$$T = \frac{1}{2}\frac{4Z_0\pi^3 n^4}{3\lambda^4}(\frac{8r^3 H_0}{3})^2 \tag{2.14}$$

Thus an increase in the refractive index will increase the power of the transmission and will change the electromagnetic field, as shown in Figure 2.3. As the particle begins to move away from the trap, the field is changed and the particle is drawn back to the trap [58]. The double nanohole aperture shape is beneficial for its ability to localize the gradient force to a small region near its cusps below the diffraction limit.

2.4.3 Protein Sizing

DNH optical tweezers success comes from their ability to trap small proteins. In fact, they are capable of trapping and sizing significantly smaller proteins than the leading competitors iSCAT and NEOtrap. Figure 2.4 shows that DNH tweezers are capable of trapping down to 4kDa, smaller than both NEOtrap and iSCAT. It should be noted with iSCAT, that the precision drops to 75% at 18kDa and 60% at 9kDa and require machine learning to detect [65, 9, 4].

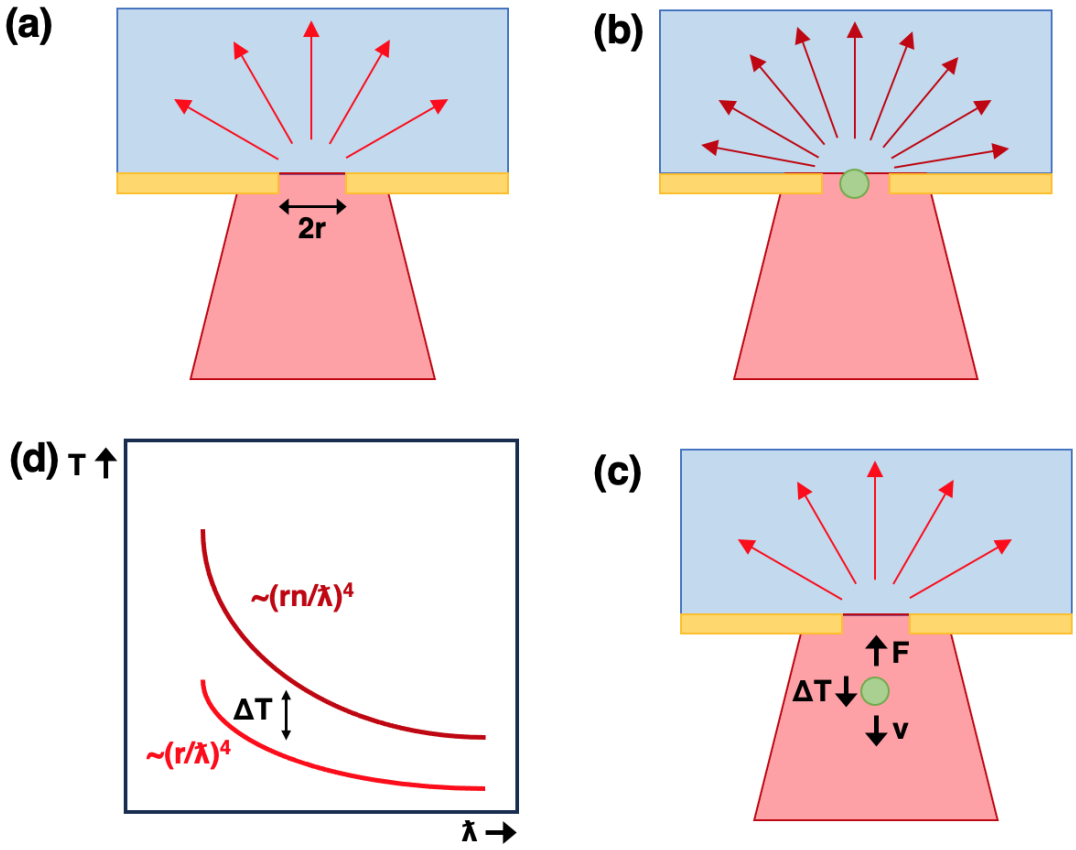

Figure 2.3: Optical transmission through a subwavelength aperture (a) No particle. (b) Particle trapped in the aperture with an increased transmission. (c) Decrease in transmission when particle moves away from the trap. (d) Dielectric loading increases transmission through an aperture.

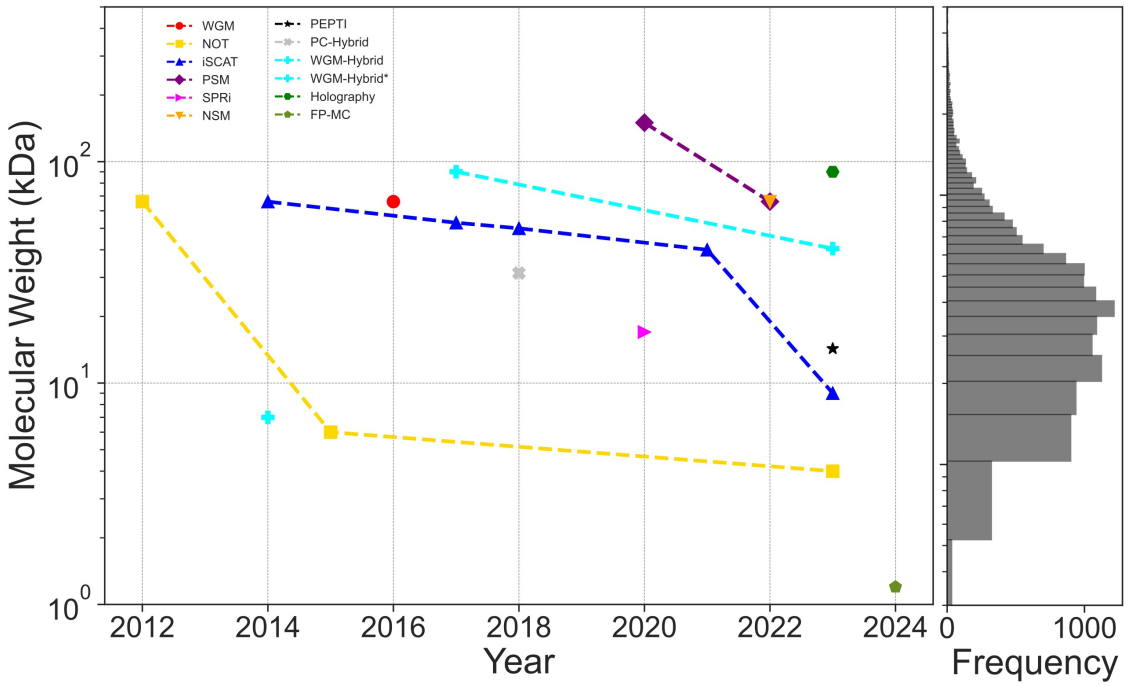

Figure 2.4: Molecular weight sensitivity of label-free single biomolecule technique advancements over time. Whispering gallery mode (WGM) ([1]), nanoaperture optical tweezer (NOT) ([2, 3, 4]), interferometric scattering (iScat) ([5, 6, 7, 8, 9]), plasmonic scattering microscopy (PSM) ([10, 11]), surface plasmon resonance imaging (SPRi) ([12]), nanofluidic scattering microscopy (NSM) ([13]), plasmon enhanced protein tracking through interference (PEPTI) ([14]), photonic-plasmonic hybrid (PC-Hybrid) ([15]), plasmonic-WGM hybrid (WGM-Hybrid) ([16, 17]), WGM-Hybrid* measured nucleic acids ([18]), holography ([19]), FP-MC [20]. Corresponding histogram of human proteome size/frequency is shown to the right ([21]).

Three methods are typically used to size the trapped proteins: autocorrelation, corner frequency, and normalized root mean square deviation (NRMSD).

Autocorrelation is the similarity between observations of a random variable as a function of the delay between them. An exponential decay time (τ) is seen and provides a measurement of the trap stiffness. From Newton's second law of motion the trap stiffness can be discovered.

$$F = mx'' = -\kappa x - \gamma x' + F_L \tag{2.15}$$

The Stokes' drag is specified by γ, stiffness by κ, and F_L is the Langevin term ac-

counting for Brownian motion. A simplification assuming the inertia to be 0 provides the formula for τ.

$$\tau = \frac{\gamma}{\kappa} = \frac{6\pi\eta r}{\alpha\nabla|E|^2} \tag{2.16}$$

The corner frequency of the power spectral density simply a $\frac{1}{\tau}$ relation with

$$f_c = \frac{1}{\tau} = \frac{\kappa}{\gamma}, \tag{2.17}$$

and can be calculated from a Lorentzian fit of the power spectral density of the trapped signal. The idea is that the frequency information of the particle motion is related to the trap strength.

Additional drag forces are present due to the nanostructure boundaries and the Stokes' drag can be reformulated as follows.

$$\gamma = \frac{6\pi\eta r}{1 - \frac{9}{16}(\frac{r}{h}) + \frac{1}{8}(\frac{r}{h})^3 - \frac{45}{256}(\frac{r}{h})^4 - \frac{1}{16}(\frac{r}{h})^5} \tag{2.18}$$

Where η is the viscosity, r is the radius of the particle, and h the distance from the nanostructure wall to the center of the particle [66].

Skylar Wheaton demonstrated molecular weight characterization of globular proteins having a linear dependance when using RMSD [3]. The potential energy of a Rayleigh particle is written as:

$$U = \frac{1}{2}\alpha|E|^2, \tag{2.19}$$

remembering that α scales with r^3, or the volume. The potential energy is proportional to the intensity so their RMS values will be proportional as well.

$$\sqrt{I^2} \propto \sqrt{U^2} \tag{2.20}$$

Using equations 2.19 and 2.20 we can see that the RMSD scales with the polarizability, and thus the volume.

$$\sqrt{I^2} \propto \alpha \frac{|E|^2}{2} \tag{2.21}$$

2.5 Concluding Remarks

This chapter has provided an overview of common single protein imaging techniques, describing the theory of interferometry and scattering as detection, optical tweezer forces, and the analysis and interpretation of optical tweezer data. Of importance is that the polarizability of a protein is related to its molecular weight, and thus optical tweezers are able to size trapped particles. Furthermore, the scattered field scales with polarizability, making scattering detection of single proteins difficult.

Chapter 3

Methods

3.1 Introduction

This Chapter will cover the methods used in the experiments performed for this thesis.
Section 3.2 will introduce the colloidal lithography techniques and sample fabrication.
Trapping solutions will be covered in section 3.3.
Section 3.4 will detail the microscope setup used to perform the experiments.
Lastly, Section 3.5 reviews computer vision for biological imaging.

3.2 DNH Sample Fabrication

Past works from the Nanoplasmonics Lab have shown the colloidal lithography used to fabricate the double nanohole samples [67].

3.2.1 Colloidal Lithography

A 75x50x1mm glass microscope slide (Fisherbrand) is cut into three pieces using a diamond scribe, the dust is removed by rinsing with ethanol and blow dried with nitrogen. These pieces are then sonicated in ethanol for 10 minutes, rinsed with ethanol and acetone, and blow dried again with nitrogen gas. A final visual inspection is done to ensure that there are no large pieces of dust remaining on the slide and

that there are no scratches.

Polystyrene spheres (PS) are used to form the mask, 10 μL* of the PS and 1mL of ethanol are mixed gently. Following the mixing, 10 μL of the diluted PS solution is deposited in a zig-zag pattern using a micropipette. The coated slides are left overnight for the ethanol to evaporate where the PS will form dimers at random. After evaporation, the coated slides are treated with a plasma cleaner for 170 seconds** using a Harrick PDC plasma cleaner to control the dimer cusp size. Each chip needs to be plasma etched individually, ensuring the placement in the machine is the same each time, and the plasma is consistent.

* Amount of polystyrene solution is dependent on the brand used.
Thermofisher 300 nm: 20 μL
Alpha Nanotech 200-400 nm: 10 μL
Sigma Aldrich 300 nm: 6 μL

** Plasma cleaning time is dependent on polystyrene brand and size
Thermofisher 300 nm: 140 s - 170 s
Alpha Nanotech 200 - 400 nm: 170 s
Sigma Aldrich 300 nm: 170 s

Titanium*** and gold are sputtered onto the coated slides using a MANTIS QUBE system. Double sided polyamide tape is used to adhere the samples to the mounting plate with the coated side facing outwards. The following steps are then performed:

1. Run the initial process to ensure everything is in its initial condition.
2. Deposit a 7 nm layer of titanium to help gold adhere. Ensure material properties are correct in the recipe.
3. Deposit a 70 nm layer of gold. Ensure material properties are correct in the recipe.

The samples are removed from the MANTIS system and then sonicated for 5 minutes**** in a beaker with ethanol. The samples are placed in the beaker so they lean against the side to ensure that the PS falls off and the gold isn't scratched. The samples are rinsed with ethanol and blow dried with nitrogen.

*** The adhesion layer metal is not limited to Titanium, other metals such as Chromium or Chromium (III) Oxide may be used, as well as varying thicknesses. Past experimental work has shown that 13 nm Chromium adhesion layers show a +43 degree Celsius increase in temperature when illuminated at 5 mW/μm^2, a 6 nm Ti adhesion layer showed a +19 degree Celsius increase in temperature, and no adhesion layer showed a +4.3 degree Celsius increase. Adhesion layer thicknesses of 6 nm for Ti, Cr, and Cr_2O_3 showed a similar temperature increase, indicating the thickness is more important than material [68].

**** Sonication time is dependent on PS brand used.
Thermofisher 300 nm: 10 minutes
Alpha Nanotech 200-400 nm: 2 minutes
Sigma Aldrich 300 nm: N/A, sonication does not work

If sonication does not work, then a tape lift off procedure should be used. In this case, using scotch tape, dab the tape on your gloved hand until most of the adhesive is removed. Then gently tap the gold with the tape, ensuring you tap every area of the gold to remove the PS.

The above steps are simplified and shown in figure 3.1.

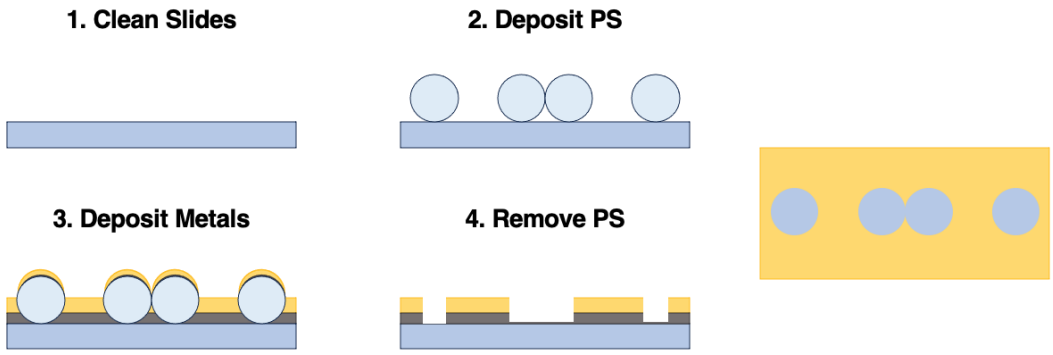

Figure 3.1: Colloidal lithography technique for making DNH samples.

The gold samples are cut into fours using the diamond scribe and blow dried to

remove dust. The last step involves either plasma cleaning or UV/ozone treating the surface.

1. Plasma cleaning: Samples are treated using the same Harrick system for 10 minutes and immediately placed in a jar of water until use.

2. UV/ozone: Samples are placed in a UV/ozone machine. The stage temperature is set to 0 deg C and the lamp is turned on. Oxygen is flowed in for 10 minutes and then turned off. The UV lamp is left on for another 40 minutes.

I have optimized this method for the aperture dimensions ideal for my work. By plasma etching individually I have been able to achieve apertures with a 5 nm cusp distance variation, whereas focused ion beam milling of double nanoholes has achieved between 8 nm [69] and 15 nm [70] variation.

3.2.2 Characterization

A Hitachi S-4800 in the Advanced Microscope Facility maintained by CAMTEC at the University of Victoria is used to characterize the fabrication. The diameter of the holes and cusp separation are measured to ensure that the fabrication was successful. A successful fabrication would be characterized by a clean sample, smooth edges of the holes, and a cusp separation less than 80nm, although the preferable distance is 15-25nm. Typical SEM parameters used are a 4mm working distance, 2kV, 10μA electron beam.

3.3 Trapping Solutions

Prior to preparing any trapping solution, a 24x60-1.5 coverslip (Fisherbrand 22266882) is rinsed with isopropyl alcohol, acetone, and ethanol. The coverslip is blow dried with nitrogen gas and placed on new lens paper. An image spacer (Grace Bio-Labs GBL-654008-100EA) is stuck on the coverslip and the trapping solution is pipetted into the spacer. The DNH sample is placed on top of the spacer so the gold is in contact with the solution. An overview of this process is shown in figure 3.2.

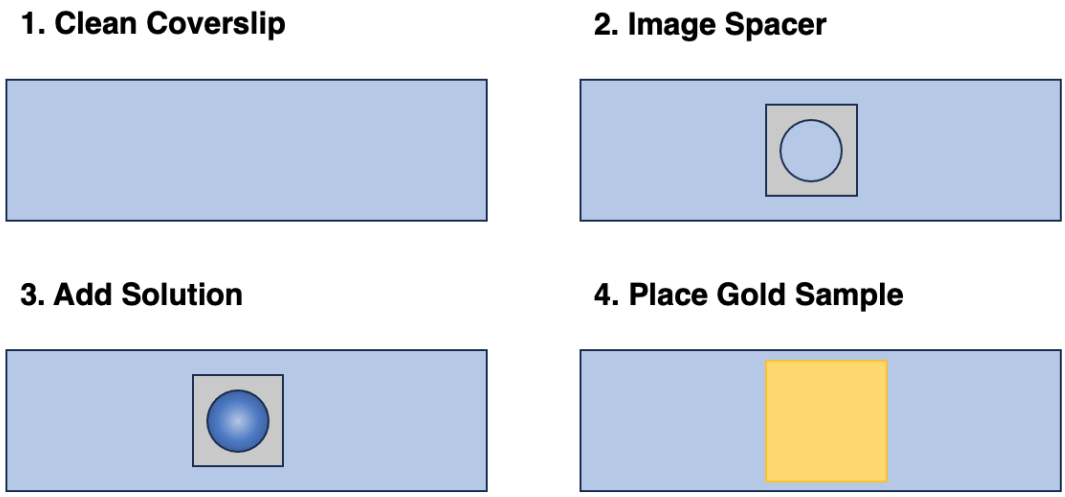

Figure 3.2: Four step process for creating trapping samples.

3.3.1 Polystyrene

The following procedure is the same for each of 20nm, 30nm, and 60nm polystyrene trapping solutions. A 1.5mL eppendorf tube is filled with 1mL ultrapure water, 20μL of the desired polystyrene size is mixed gently with the water by rolling the tube. The final trapping solution consists of 9.5μL of the diluted polystyrene solution.

3.3.2 Proteins

Proteins are from a Sigma Aldrich size-standard kit (MWGF200-1KT). Bovine Serum Albumin (BSA), Carbonic Anhydrase (CA), and Cytochrome C (CTC) were prepared with a concentration of $0.1\frac{wt}{v}\%$. The proteins were weighed in 1.5mL eppendorf tubes. Phosphate-buffered saline (PBS) and Tris-HCL buffers were used interchangeably and no noticeable difference was found, so PBS was used for the experiments.

3.3.3 Extracellular Vesicles

A 24×60-1 microscope cover glass (globe Scientific Inc.) was cleaned using isopropyl alcohol and dried under nitrogen. An image spacer (Grace Bio-Labs GBL-654008-100EA) was placed in the center of the coverslip and 9.37 μL of the solution was pipetted into the spacer. The gold DNH sample was placed on top of the spacer so the gold is in contact with the solution. EVs were diluted in phosphate buffered saline (PBS) to a concentration of 0.112 μg/μL (MCF10A), 0.494 μg/μL (MCF7), and 0.191 μg/μL (MDA-MB-231).

3.4 Optical Trapping Setup

The optical trapping setup consists of an 850 nm laser for trapping. Two mirrors are used at the fibre launcher to help with ensuring the laser path is level and straight. A half-waveplate and linear polarizer are placed in the beam path to control the polarization and orientation of the polarization for detecting a double or single nanohole. The beam is then expanded and collimated using two lenses where it is incident on a dichroic mirror and enters the microscope column. A 100x oil-immersion objective focuses the beam tightly onto the DNH sample. When the laser is incident on the DNH, there is a transmitted beam that is collected with a 10x objective and a reflected beam that follows the excitation laser path. A white light LED emits from

the top of column through the 10x objective, through the sample, through the 100x objective, and passes through the aforementioned dichroic mirror. A lens focuses this light onto a charge-coupled device (CCD) camera. The reflected laser beam is strong enough that some of it passes through the dichroic and this is also incident on the CCD and overpowers the LED signal. The transmitted signal hits a dichroic mirror and is sent to a lens that focuses on an avalanche photodiode (APD) where the trapping signal is detected. The samples are held on a 3-axis piezo controller to precisely control the positioning. Figure 3.3 shows a simplified diagram of an optical nanotweezer setup.

3.4.1 Optical Tweezing

The optical trapping setup consists of an 850 nm or 980 nm laser for trapping, although any wavelength near a resonance works. The specific type of laser does not seem to play a significant role in trapping: successful trapping has been performed with an 850 nm (Thorlabs LP852-SF60, solid state), 980 nm (JDS Uniphase 27-7602-200-TE, solid state, fiber Bragg grating stabilized), 532 nm (Renishaw RL532C50, solid state) and 633 nm (Renishaw RL633, HeNe). Two mirrors are used at the fibre launcher to ensure the laser path is level and straight. A half-waveplate and linear polarizer are placed in the beam path to control the polarization and orientation of the polarization for detecting a double or single nanohole. The beam is then expanded and collimated using two lenses where it is incident on a dichroic mirror and enters the microscope column. A 100x oil-immersion objective focuses the beam tightly onto the DNH sample. When the laser is incident on the DNH, there is a transmitted beam that is collected with a 10x objective and a reflected beam that follows the excitation laser path. A white light LED emits from the top of column through the 10x objective, through the sample, through the 100x objective, and passes through the aforementioned dichroic mirror. A lens focuses this light onto a charge-coupled device (CCD) camera. The reflected laser beam is strong enough that some of it passes through the dichroic and this is also incident on the CCD and overpowers the LED signal. The transmitted signal hits a dichroic mirror and is sent to a lens that focuses on an avalanche photodiode (APD) where the trapping signal is detected. The samples are held on a 3-axis piezo controller to precisely control the positioning.

Immersion oil is placed on the prepared coverslip and the whole sample is placed on the 100x objective so that the laser is incident through the solution first.

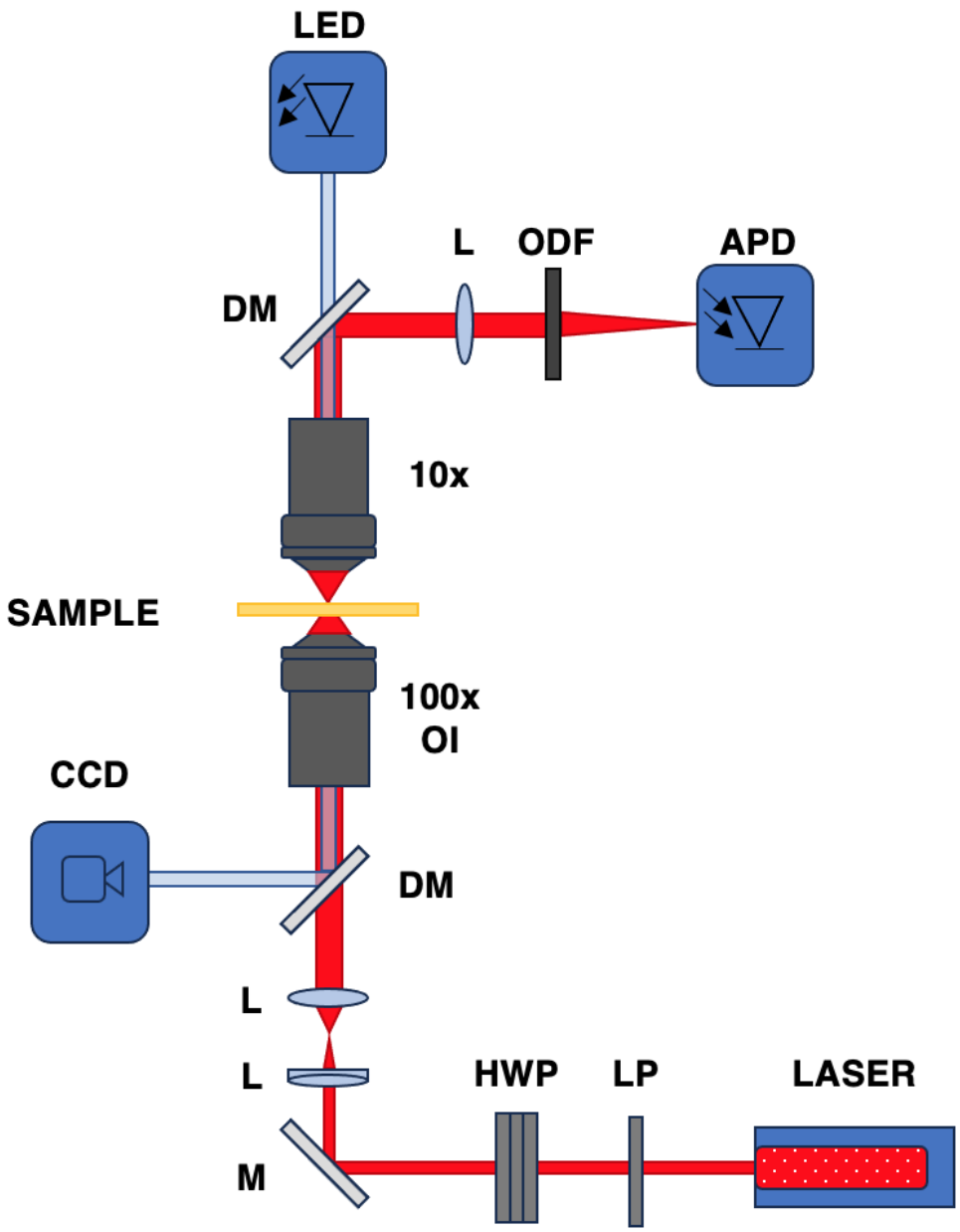

Figure 3.3: Schematic of optical setup: APD: Avalanche Photodiode. ODF: Optical Density Filter. LED: Light Emitting Diode. L: Lens. DM: Dichroic Mirror. M: Mirror. CCD: Charge-Coupled Device. OI: Oil-Immersion. LP: Linear Polarizer. HWP: Halfwave Plate.

Identifying a double or single nanohole is performed in two steps. The first step is purely qualitative and done by eye. On the camera, a double nanohole, while sub-wavelength, will appear as an oval shape and slightly brighter than a single nanohole, which appears as a circle. The second step, once the laser is aligned on the double nanohole, is to rotate the half-waveplate and observe the transmission change. A single nanohole is a symmetric structure, and thus rotating the linearly polarized light should yield little to no change in transmission. A double nanohole, being asymmetric, will show a large change in transmission as the linearly polarized light is rotated from the short axis to the long axis of the structure.

3.4.2 Trapping Tips

Trapping is sensitive to the alignment to the double nanohole. Here are some tips for ensuring the best trapping.

1. Turn the laser on at low power.
2. Using the coarse stage adjust, position the DNH at the center of the laser spot.
3. Using the fine piezo control, align the double nanohole so that the APD signal is maximized.
4. Rotate the half-waveplate until the transmission is maximized, this corresponds to an orientation along the long axis.
5. The optimal trapping position is where the APD signal is maximized, corresponding to the maximum transmission through the DNH. This occurs in the x-y position when the laser is centered, in the z position, the laser is underfocused such that a larger area is illuminated.
6. Something that helps me, is to adjust the x-y position, then adjust the z, adjust the x-y again, and adjust the z again. I will repeat this until I am convinced I have the maximum transmission.
7. Increase the laser power to your trapping power. Typically below 10 mW.
8. Members of our group, as well as other groups that perform optical trapping have noted that trapping on a floated table is integral to successful trapping.

Data Acquisition

An Advantech USB-4711A data acquisition unit (100 kS/s, 12-bit) collected the APD signal. Advantech DAQ Data Logger Express was used to display the live data. Data was analyzed in both MATLAB and python.

Data Analysis

All analysis of APD data was performed in python. A low pass filter with cutoff frequency of 10 Hz was used when plotting the avalanche photodiode signal.

Power Spectral Density. The power spectral density was calculated using a 5 second portion of the trapped data. The absolute value squared is taken and then Fourier transformed. The positive spectrum is used and fit to a Lorentzian function of the form $\frac{A}{f^2+f_c^2}$, where f_c is the corner frequency. The autocorrelation function measures the similarity between a signal and its time-delayed version whereas the power spectral density function gives the distribution of average power in the frequency domain. Since the autocorrelation shows an exponential dependence, and the PSD is the Fourier transform of autocorrelation, the corner frequency is the inverse of the time constant [71].

Time Constant. The time constant is related to the corner frequency obtained from the power spectral density by $\frac{1}{2\pi f_c}$.

Normalized RMSD. The trapped signal was divided into sections based on the length of the signal divided by window length (5,000). The RMSD was calculated for each section as $\sqrt{\frac{1}{n}\sum_{i=1}^{n}(\hat{x}_i - x_i)^2}$, and then divided by the mean of the trapped signal, and the average of all of these sections was taken. This was repeated for the laser signal before trapping. The laser RMSD was then subtracted from the trapped RMSD.

Image Processing

Videos were recorded with a Thorlabs DCU224C-BG camera (1280 $\times$ 1024 pixels, 1.31 Megapixel) and uc480 software from ThorLabs as well. A minimum exposure time and gain was used as allowed by the camera, RGB channel gains were equal. The object detection algorithm contained 9998 frames from the videos and a total of 19672 images obtained from augmenting the dataset. Training set contained 14661 images (75%), validation set contained 2935 (15%), and test set contained 2076 (10%). A

manual check for all videos was performed to ensure accuracy.
Distance Calculations. An $x - y$ coordinate was obtained from the detected protein in the video. The interpoint distance was calculated from $\sqrt{(x_2 - x_1)^2 + (y_2 - y_1)^2}$.

3.5 Computer Vision

Images and videos recorded during experiments contain a wealth of information about the size, shape, orientation, and dynamics of the biomolecules of interest. Image processing refers to the methods that alter images to highlight specific aspects. These include contrast, filtering, segmentation, and deconvolution [72]. Image analysis refers to making sense of an image and obtaining information. Computer vision deals with image analysis and is present in industries from robotics to surveillance to biology [73, 74, 75, 76, 77]. Human processing of images and videos is not scalable and is inherently subjective, the goal of computer vision is to scale up to many thousands of images and remain self-consistent in the information it outputs. Early developments of computer vision for biological purposes were in cell mitosis defects and counting/tracking cells where the computer resulted in sufficiently good results compared to human classification [78, 79]. Often, distinguishing between biological processes and events in images and videos is extremely difficult, or requires an exceptionally trained human. In the case of optical tweezing, particle movement is confined in subwavelength spaces with random motion: light is scattered according to this motion but is near impossible to characterize by the human eye.

3.5.1 Background Removal Techniques

Akin to iSCAT, optical nanotweezers (ONTs) are able to "see" proteins when they are orbiting the trapping site. The signal however, is dominated by the fringe pattern generated from the incident laser on the gold surface. This behaviour is regular until an object perturbs the environment. An issue arises when attempting to remove the background laser noise as the fringes are still present when a protein is trapped, albeit slightly different. With many background removal techniques, this can cause certain areas of the video to have black spots where there is useful information. A brief background on three methods of removal are presented here and the results are shown in Chapter 4.

3.5.1.1 Frame Averaging

Frame averaging is a simple approach to background removal that is as the name suggests. Each frame is a matrix of pixels, and for a specified number of frames, these matrices are are averaged to generate a single matrix that likely represents the background. Defining the background model as BG, the current frame as F, and the number of frames for averaging, this method can be described as follows:

$$BG(x,y) = \frac{1}{N}\sum_{i=1}^{N} F_i(x,y) \tag{3.1}$$

Once the background model is created, the difference between each frame and the background is given by:

$$D_i(x,y) = F_i(x,y) - BG(x,y) \tag{3.2}$$

where D_i is the current frame difference [80].

3.5.1.2 Sequential Removal

In sequential frame removal, there is no background model to create, each frame has the previous frame subtracted from it.

$$F_i(x,y) = F_i(x,y) - F_{i-1}(x,y) \tag{3.3}$$

Where F_i is the current frame and F_{i-1} is the previous frame.

This technique is rather simple but can be beneficial to show frame by frame changes that may be obscured by other techniques. This can also be expanded to remove the last 2, 3, 4... etc. frames from the current frame.

$$F_i(x,y) = F_i(x,y) - \frac{1}{N}\sum_{k=1}^{N} F_{k-N}(x,y) \tag{3.4}$$

Where N is the number of previous frames to remove.

3.5.1.3 Gaussian Mixture Models

Gaussian mixture models (GMMs) are a more advanced and robust method of background removal than the previous two methods. Given a regular background environment, it can be modelled statistically with a probability density function (PDF) for each pixel. In the next frame, each pixel is compared to the PDF to decide if it is a background (BG) or foreground (FG) object [81]. The value of the pixel at a time t is denoted as $\vec{x}^t$ and the Bayesian decision R is decided as follows:

$$R = \frac{p(BG|\vec{x}^t)}{p(FG|\vec{x}^t)} = \frac{p(\vec{x}^t|BG)p(BG)}{p(\vec{x}^t|FG)p(FG)} \tag{3.5}$$

Typically the foreground objects are unknown so $p(FG) = p(BG)$ and a uniform distribution is assumed for the foreground object and $p(\vec{x}^t|FG) = c_{FG}/$ It can then be decided if the pixel belongs to the background or foreground if $p(\vec{x}^t|BG) > c_{thr}(= R_{c_{FG}})$ where c_{thr} is the threshold value. A training set χ_T is used to create $p(\vec{x}^t|BG)$, in the case of ONTs, a section of recorded video where there is no particle is the training set. GMMs traditionally update the training set to adapt to changes in the environment. Each new sample reestimates the background model, but this can mean that FG objects get included in the background estimation. This estimate can be denoted as $p(\vec{x}^t|\chi_T, BG + FG)$. For a model with N components:

$$p(\vec{x}^t|\chi_T, BG + FG) = \sum_{n=1}^{N} \hat{\pi}_n \mathcal{S}(\vec{x}; \vec{\mu}_n, \hat{\sigma}_n^2 I), \tag{3.6}$$

where $\hat{\vec{\mu}}$ is an estimate of the mean and $\hat{\sigma}$ is an estimate of the variance of the Gaussian components. These two components, along with the mixing weight, $\hat{\pi}_n$ are updated for each new sample recursively. With this approach, the FG objects that may have been contained in the new training set can be represented as cluster with low mixing weights and the BG model can be approximated as [81]:

$$p(\vec{x}^t|\chi_T, BG) \approxeq \sum_{n=1}^{N} \hat{\pi}_n \mathcal{S}(\vec{x}; \vec{\mu}_n, \hat{\sigma}_n^2 I). \tag{3.7}$$

3.5.2 Convolutional Neural Network

MATLAB convolution1dLayer was used as the platform for sequence classification. A filter size of 5, 32 filters, 1 feature, 3 classes, mini batch size of 5, 200 epochs, and learning rate of 0.001 was used for the training. The files are split between training and testing and split into smaller time segments (1 second). Additional files were kept outside of the model generation and tested afterwards. The optical signal was normalized to remove the DC offset due to day-to-day differences and small aperture variations as well as to enhance the features present in the data. The normalization was of the form Voltage = 10*(Voltage-mean(Voltage)) + 2*(mean(Voltage)), this allows for amplification of the fluctuation features in the data and the amplitude of the signal. The normalized data was then downsampled to 500 Hz from 100 kHz and all files were ensured to have the same length.

3.6 Concluding Remarks

This Chapter has provided a thorough description of the colloidal fabrication of double nanoholes, alignment and use of the optical tweezer microscope, data analysis, image processing, and sample preparation.

Chapter 4

Label-free tracking of proteins through plasmon enhanced interference

4.1 Introduction

The dominant approaches to observing single proteins, their dynamics and interactions, modify the protein with fluorescent labels and/or tethers [82]. These modifications often alter the protein's biophysical properties and limit the observation time due to quenching [83, 84, 85]. When investigating unknown targets, labelling can be challenging since interactions are not pre-defined. For example, new methods of kinetic screening of antibodies developed from hybridoma technologies aid monoclonal antibody development [86]. Thus it is desirable to seek out methods that can directly observe single unmodified proteins to complement fluorescent measurements. This remains challenging since particles much smaller than the wavelength of light have scattering that diminishes with the sixth power of the radius [87].

Several techniques have emerged to quantify single proteins without labels. Interferometric scattering (iSCAT) has imaged single proteins in solution without modifications [37, 88, 89, 90]. Due to inherent contrast limitations, iSCAT has been limited to 40 kDa detection, but with machine learning and lengthy frame averaging, has pushed detection to 9 kDa, albeit with only 60% precision [9]. Additionally, tracking

of proteins has not be performed without the addition of strong scatterers such as gold nanoparticles to amplify the movement [91, 6, 92, 93].

Plasmonic scattering microscopy (PSM) has been shown to image non-specific single protein binding using interference from surface plasmon resonance sensors and analytes [10]. The evanescent field only extends $\simeq$100 nm away from the surface so bulk impurities in solution do not affect the imaged results, and images the transmitted signal to avoid the strong reflection from the gold surface. Currently, this has been shown to image binding of a 35 kDa protein in solution, but is unable to track its diffusion [39, 40, 41].

Nanofluidic scattering microscopy (NSM) utilizes subwavelength channels combined with dark-field microscopy to track the diffusion of single proteins through interference with the channel. This method is able to size single proteins using the optical contrast of a differential image and demonstrates tracking down to 66 kDa [29].

These methods rely on an interference between the particle scattering and a reference signal and the signal scales with the volume of the particle. Even with high laser powers and long averaging, these techniques are typically not able to observe proteins below 30 kDa, which accounts for half the human proteome [38].

By combining the surface plasmon interference with the reflected laser beam interference, we observe light scattering to track the diffusion of single unmodified proteins in real time adjacent to a nanoaperture in a gold film. We track proteins as small as 14 kDa with copious signal (so smaller proteins will be resolvable in the future) in a technique we have named Plasmon Enhanced Protein Tracking through Interference (PEPTI). We observe that diffusion is faster for smaller proteins, as expected from their reduced Stokes' drag. The observed signal has fringes showing interference scattering, but also contains a surface plasmon contribution due to the adjacent gold surface; therefore, we believe the extraordinary sensitivity achieved combines the physical principles that have enabled iSCAT and PSM so far. We observe the trajectory of various proteins as they approach the nanoaperture and are trapped. Once trapped, further analysis on the protein is performed using nanoaperture tweezer techniques previously established [94].

4.2 Single Protein Trapping

Optical nanotweezers (ONTs) are already a well established technique for single protein measurements [2, 95, 96, 97, 98, 70, 94]. Figure 4.1(a) shows a representative trapping event for three size-standard proteins: Bovine Serum Albumin (BSA), Carbonic Anhydrase (CA), and Cytochrome C (CTC). The transmitted light through the double nanohole (DNH) is recorded by an avalanche photodiode (APD), with a trap characterized by an increase in transmission due to dielectric loading of the nanoaperture and an increase in the "noise" of the signal, due to the Brownian motion of the trapped protein. Analyzing the trapped signal provides information about the molecular weight of the protein. Figure 4.1 (b-c) show the relation between molecular weight and the time constant and normalized root-mean-squared-deviation (RMSD) of the signal. The RMSD is representative of the Brownian motion of the protein in the trap, including a vertical displacement. Self induced back action trapping of dielectric nanoparticles showed similar trap stiffness measurements for X motion and Z motion, indicating that the vertical displacement is similar to the horizontal [58]. The time constant is obtained by fitting a Lorentzian to a power spectral density analysis of the trapped signal, with the corner frequency, and thus the time constant, relating to the trap stiffness. The RMSD is a representation of the amplitude of the trapped signal and correlates linearly with the molecular weight. The time constant and RMSD of the trapped proteins both follow the expected trends for sizing single proteins in previously established methods [3]. The exponent of the time constant fit is -0.70 (expected -0.667), showing good agreement with past works. By taking a slice of the recorded frame, as shown in Figure 4.1 (e), the reflected light can be correlated with the transmitted, as seen in Figure 4.1 (f). The time evolution of the slice shows a distinct trapping point despite the significantly slower sampling rate (30 Hz) compared to the APD (100 kHz). The fringes in the video are shown as distinct bands in the waveform, with the highest intensity correlating to the center lobe. By recording the center pixel intensity and overlaying it with the corresponding APD signal, the reflected light shows the expected reciprocal of the transmitted light, allowing us to confirm that the camera and APD are both recording a single protein.

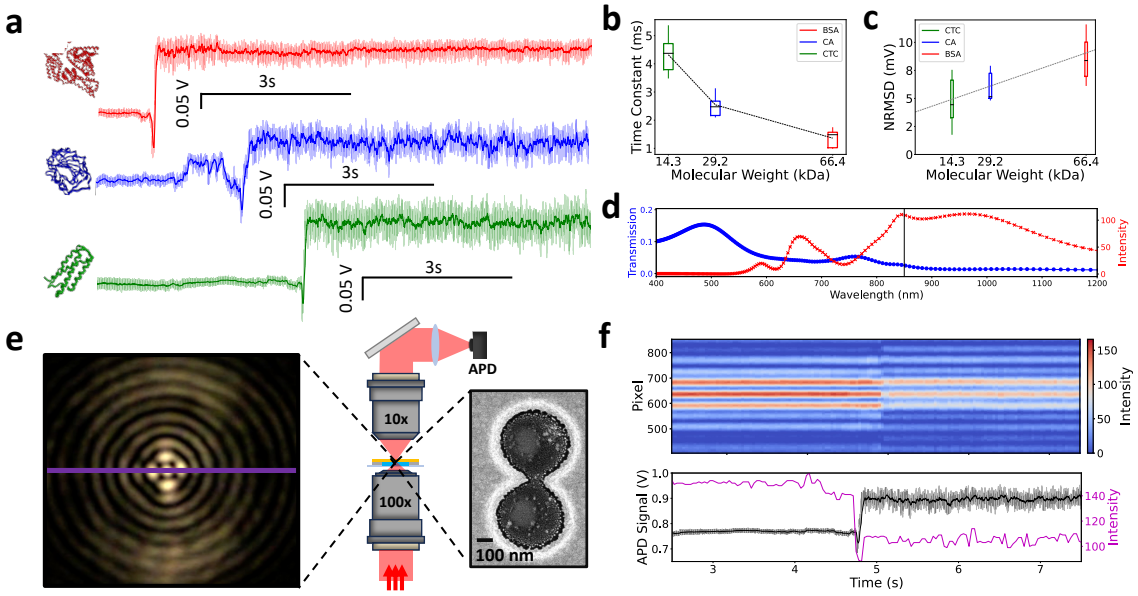

Figure 4.1: (a) Representative trapping signals for Bovine Serum Albumin (red), Carbonic Anhydrase (blue), and Cytochrome C (green). (b) Measured time constant of the protein in the trap, obtained through power spectral density analysis of the photodiode signal. (c) Normalized root-mean-squared-deviation measurement of the trapped protein, obtained from photodiode signal. (d) Transmission and intensity enhancement of a double nanohole simulated using Ansys Lumerical. (e) Simplified plasmonic optical trapping diagram showing an image captured from the reflected laser beam and a scanning electron microscope image of a souble nanohole. APD: Avalanche Photodiode. (f) Time evolution of a line of pixels recorded in reflection and a single pixel recorded over time overlaid on the corresponding photodiode signal measured in transmission.

4.3 Unmodified Single Protein Tracking

Surface plasmon waves are launched by focusing an 850 nm laser on a nanostructure in gold. The surface plasmon waves interfere with the scattering of the protein. Direct observation of protein scattering is masked by laser reflections; however, the fringes act as a semi-constant medium that is perturbed by the enhanced plasmon-protein scattering. The phase difference between the surface plasmons and protein scattering give rise to a strong interference term, and an additional interference effect is present from the gold reflection and protein scattering that further enhances the signal. While the overall scattering (E_s), including interference from the aperture scattering (E_p) with the direct reflection from the gold film (E_r), shows dynamic variation, the ability

to track the protein arises by differential analysis seen in Figure 4.2 (a). The single frame subtraction is computationally efficient, allowing for real-time tracking without the need for frame averaging. The previous frame was subtracted from the current frame giving rise to an image with negative and positive components. The absolute value of the differential image was taken and then smoothed with a Gaussian filter (σ=8) and a median filter to reduce the noise. A Roboflow 3.0 object detection model was trained on 19672 frames from 15 videos, and contained augmented images as well. This algorithm was used to detect the protein and track the position. The detection and tracking algorithm runs with linear order, enabling scalable quasi-real time detection. The results of tracking can be seen in Figure 4.2 (b) for the three proteins. The interference effect was verified by using a common reference for background removal seen in Figure 4.2 (c). This showed a similar result to differential subtraction, indicating that the plus/minus signal is due to phase difference and not movement of the protein between frames.

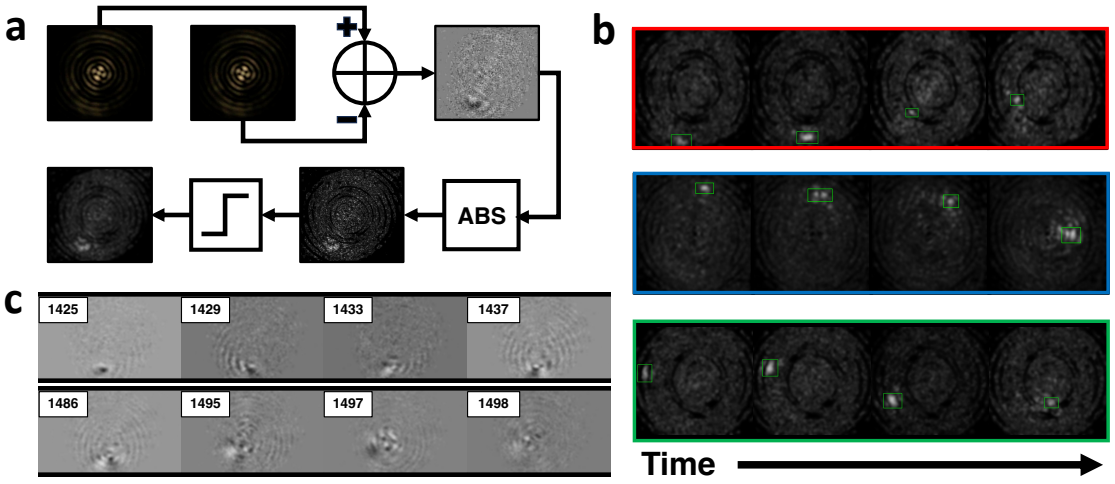

Figure 4.2: (a) Flow chart representation of the image processing. ABS: Absolute Value. (b) Single proteins tracked over time for BSA, CA, and CTC. (c) Interference images of CTC recorded over time using a static reference frame.

The scattering intensity is related to the distance from the surface: the evanescent nature of the surface plasmon contribution means that the smaller proteins are able to get closer to the surface (on the order of nanometers), and the interaction is stronger. PSM does not see this same scaling because they image proteins binding to antibodies at a fixed distance from the surface, not making full use of the evanescent

field directly adjacent to the surface. The SNR of PEPTI is remarkable compared with iSCAT, typical iSCAT for a 40 kDa protein has an SNR of 3 [9]. We show in Figure 4.3 (a-b) detection and tracking of a 14.3 kDa protein with an SNR of 3.5, with only a single frame subtraction, as well as larger proteins of 29.3 kDa and 66.5 kDa. Since the contrast has not shown scaling with the volume of the protein, the lower limit of detection should be much smaller. Due to the complex nature of the bright spot obtained, sizing the protein through a 2D Gaussian fit is not possible. Instead, it is possible to size the protein through the speed it diffuses, seen in Figure 4.3 (a). The contrast of the protein image does not follow the usual third power scaling for interference effects: for proteins with molecular weight 14.3 kDa, 29.3 kDa, and 66.4 kDa, the maximum pixel intensity is 141 ± 19, 127 ± 17, and 137 ± 28, shown in Figure 4.3 (c).

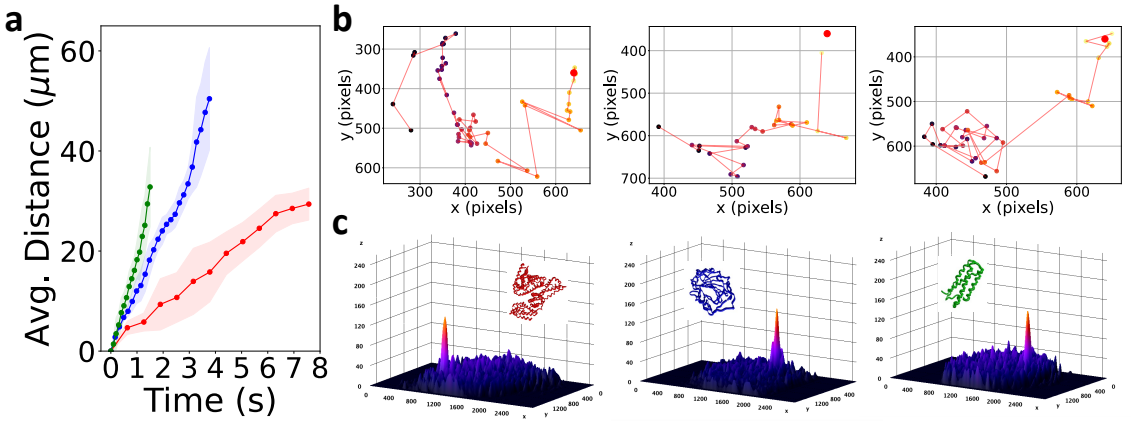

Figure 4.3: (a) Average cumulative distance travelled with standard deviation for each protein. Total events were 4 BSA, 5 CA, and 6 CTC. (b) Single protein tracking for BSA, CA, and CTC. (c) 3D surface plots of the single protein highlighting the large signal-to-noise ratio.

The diffusion speed can be obtained by measuring the cumulative distance the protein travels over time. The diffusion seems to follow the molecular weight with the distance travelled: CTC, CA and BSA travel 29.2 μm, 18.5 μm and 7.9 μm in 1.5 seconds, showing the expected trend that smaller proteins diffuse faster. As the protein moves closer to the trapping point, the diffusion becomes constrained by the trapping volume and forces present in the area. The diffusion near the trap is packed as seen in some trajectories of Figures 4.5, 4.6, and 4.7. Overall, the diffusion is slower than expected from unconstrained 3D diffusion.

4.4 Discussion

The plasmonic scattering from the DNH is polarization sensitive, and it was found qualitatively that aligning the laser polarization to excite both polarization components of the aperture (i.e., between the extrema in transmission) gave a suitable trade-off between image quality and trapping ability. Finite-difference-time-domain simulations were performed and show the reflection depends on polarization, seen in Figure 4.4.

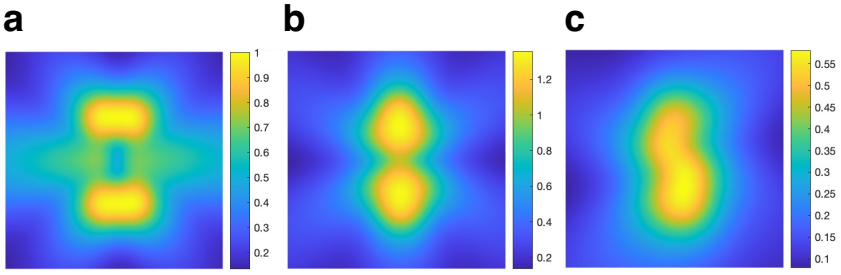

Figure 4.4: Finite-difference-time-domain simulations for linear polarized light incident along (a) short axis, (b) long axis, and (c) 45 degree angle.

The imaging area is governed by the reflected laser signal seen in the camera as the perturbations in the fringes are used to highlight the protein. The number of fringes and size of the pattern is dictated by the focus of the laser on the gold. Imaging was performed successfully in a range of areas from 280 μm^2 to 580 μm^2. When trapping proteins, maximum transmission through the aperture is desired and this results from being under focused on the aperture. A larger imaging area can be achieved by being further under focused at the expense of trapping performance. A signal with significantly larger contrast and brightness is seen when compared to PSM and iSCAT, so that neither plasmonic interference, nor reflection interference scattering play the sole role in PEPTI. In fact, a combination of effects must be present: the surface plasmon-scattering interference as described by the PSM must work in conjunction with scattering from the protein due to the incident laser beam and the reflected laser off of the gold to provide an exceptionally strong signal. While past works on PSM have shown a departure from 6th power to 3rd power scaling in experiments due to surface plasmons [10], here the scattering contrast for the 14 kDa and 66 kDa proteins is approximately the same. We do not believe that we can predict the observed size dependence with electromagnetic simulations alone. The benefit of

PEPTI is the minimal processing required, single frame removal enables real-time imaging of single proteins. Other algorithms were tested, including frame averaging combined with differential removal and a Gaussian Mixture Model, but none of them proved superior for tracking. While not analysed here, the videos contain information after trapping related to the protein position inside the nanoaperture and the stiffness of the trap.

The videos used for tracking have a frame rate of 30 frames per second, much less than the APD sampling rate and many high performance cameras. This is not a fundamental limit, and future studies should be able to make use of high-speed cameras with frame rates approaching a million frames per second even; especially since we use filters to attenuate the laser signal to avoid saturation and also reduce the camera gain, and so there is copious signal for faster imaging. This is especially interesting for observing fast folding and conformational dynamics while not requiring tethering, and for studying interactions with proteins, DNA, RNA, antibodies or other biomolecules.

4.5 Summary

We have demonstrated detection and tracking of single proteins in solution, down to 14 kDa, with copious signal to push detection limits even further. This technique does not require fluorescent labels, nor does it require binding to a substrate. Compared to similar methods (iSCAT, PSM, NSM), our approach is able to detect significantly smaller proteins, with the caveat that iSCAT has used machine learning to detect small proteins, albeit with only 60% precision. We observe size dependent diffusion with the smallest proteins diffusing fastest, as expected based on drag, and can combine this technique with optical trapping to perform complementary analysis on the protein. Future directions could aim to look at protein interactions and high speed dynamics.

4.6 Supporting Information

Figures 4.5, 4.6, and 4.7 show the tracked positions for Bovine Serum Albumin, Carbonic Anhydrase, and Cytochrome C respectively. The red dot indicates the point of trapping and the colour gradient indicates the time evolution.

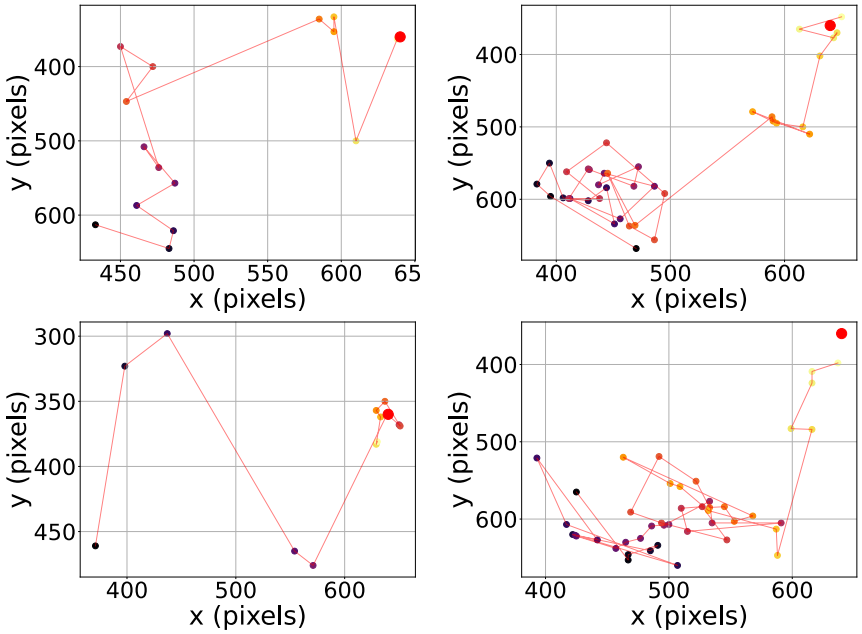

Figure 4.5: Tracking of Bovine Serum Albumin.

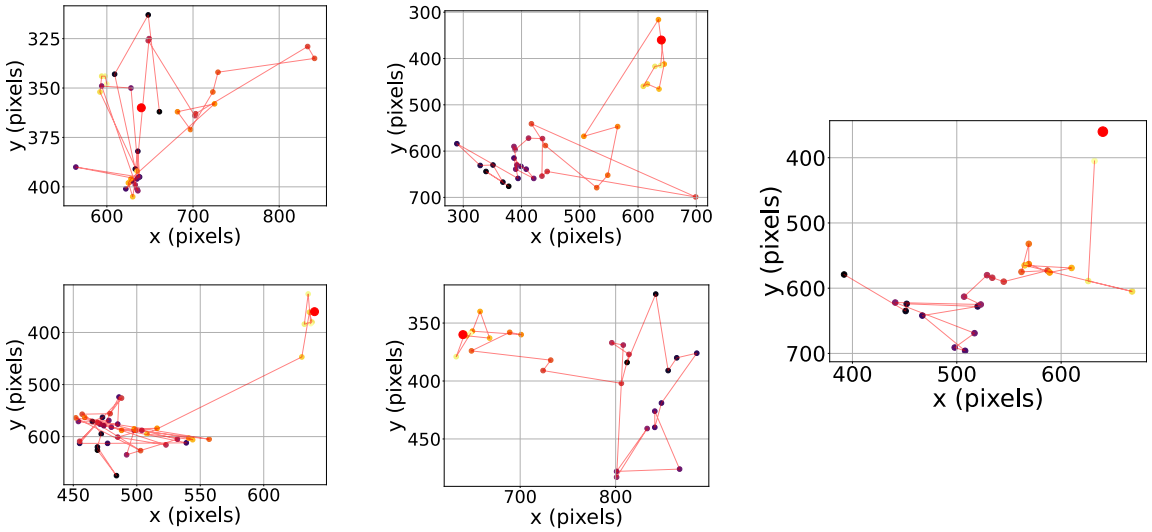

Figure 4.6: Tracking of Carbonic Anhydrase.

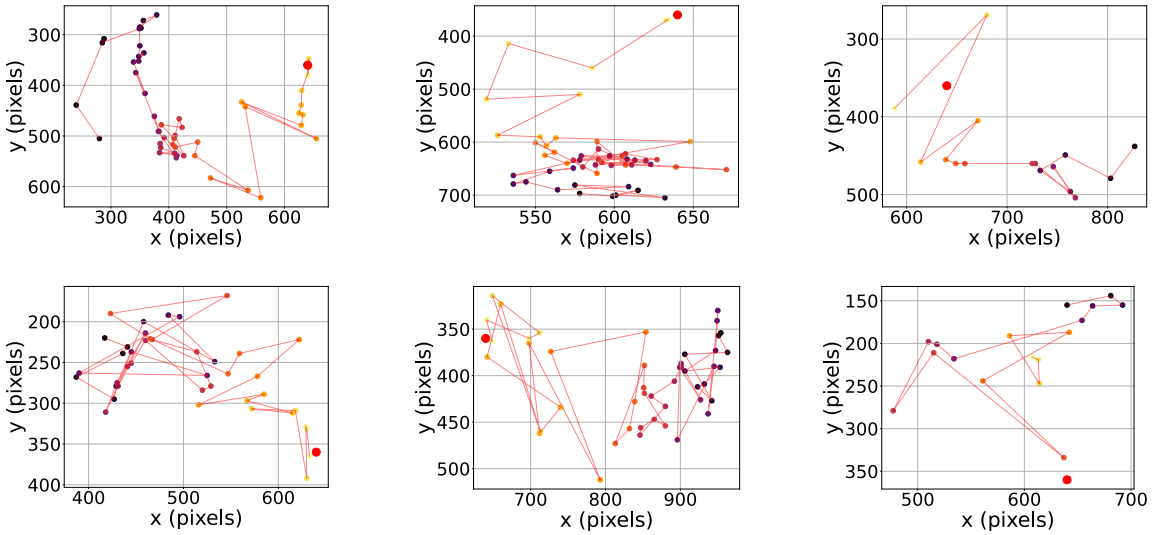

Figure 4.7: Tracking of Cytochrome C.

Properties of the proteins used in the experiments are shown in table 4.1.

Table 4.1: Properties of proteins used in experiments.

Protein	**Mass (kDa)**	**Hydrodynamic Radius (nm)**	**Isoelectric Point**	**Charge (ref. pH 7)**
CTC	14.3	1.78 [99]	9.44 [100]	+
CA	29.2	2.01 [101]	5.5 [102]	-
BSA	66.4	5.45 [103]	4.5 [104]	-

Chapter 5

Classification of cancerous and non-cancerous single extracellular vesicles using a convolutional neural network and double nanohole optical tweezers

A major challenge in cancer prognostics is finding early biomarkers that can accurately identify cancer. Circulating tumor cells are rare and circulating tumor DNA can not provide information about the originating cell. Extracellular vesicles contain cell specific information, are abundant in fluids, and have unique properties between cancerous and non-cancerous. Fluorescence measurements have limitations relating to observation times and structural modifications. Here, we demonstrate a label-free approach to classification of 3 different extracellular vesicles, derived from non-malignant, non-invasive cancerous, and invasive cancerous cell lines. Using double nanohole optical tweezers, the scattering from single trapped extracellular vesicles is measured, and using a 1D convolutional neural network, we are able to classify the time series optical signal into its respective extracellular vesicle class.

5.1 Introduction

Cancer diagnostics, monitoring, and prognostics are rapidly growing fields and biomarkers present in blood such as circulating tumor cells (CTC), circulating tumor DNA (ctDNA), and extracellular vesicles (EVs) provide a promising avenue for early-stage detection [105]. CTCs present in blood are rare, posing challenges to early detection [106, 107] and ctDNA is unable to be used for identification of the originating cell. In contrast, EVs provide good diagnostic capabilities as they contain lipids, proteins, and nucleic acids from the parent cell, enclosed within a lipid bilayer. Released by all cells through exocytosis (exosome; 30-150 nm) or budding and pinching off (ectosome; $\sim$0.1-1 μm), EVs are stable and plentiful in biological fluids (2-6 $\times$ 10^{10} EVs/mL). Due to their different cellular origin and formation, exosomes and ectosomes provide different information about the cell. The biophysical properties of cancer-derived EVs are unique: the lipid composition, nucleic acid and protein content, and membrane rigidity are altered compared to healthy cell-derived EVs. These suggest that EV liquid biopsies present an advantage over other approaches [108, 109, 110, 111].

One of the biggest challenges in cancer detection is finding early biomarkers, requiring disruptive technologies that can accurately identify the early cancer biomarkers [105]. Labelling is common in EV cancer analysis with staining or fluorophore bonding being common techniques. Fluorescent measurements have limitations from intrinsic fluorescent background signals, photobleaching, non-specific labelling, and EV structural modifications [112].

However, EVs are released by all cells and thus the population of EVs in a patient will be non-specific to cancer. Therefore, a method of interrogating single exosomes to distinguish between cancerous and non-cancerous is imperative. Given the broad size range of EVs, isolating exosomes from ectosomes becomes important for cancer detection. Current methods for isolating exosomes include ultracentrifugation [113], ultrafiltration [114], immunoaffinity capture [115], precipitation [116], or microfluidic based methods [117], but have low reproducibility and low throughput [118]. A preferred detection platform would be able to work with solution containing ectosomes and exosomes while providing accurate cancer detection.

Single EV analysis is desired to eliminate the background from healthy cell-derived EVs, which has led other researchers to consider laser tweezers to trap single EVs and take their Raman spectrum [119, 120, 121]. This approach requires large laser

powers damaging the EVs, low gradient forces inhibiting trapping of exosomes and small ectosomes, and weak Raman signals requiring lengthy integration times. Signal from single EVs can also be acquired using plasmonic antennas [122, 123, 124] and surface plasmon resonance imaging [125, 126, 127].

Double nanohole (DNH), and similarly shaped apertures, optical tweezers have previously been used to study small biomolecules such as proteins or DNA, as well as other nanoparticles [128, 96, 129, 70, 58, 59, 130, 131, 132, 133, 134, 135, 136, 137, 138, 139]. DNH optical tweezers have shown promise in interrogating single EVs at non-damaging optical powers [140, 141]. These works focused on fluorescently labelled EVs. Ideally, the DNH platform can be used to determine the nature (non-cancerous vs cancerous) of single EVs without labels. Because cancerous EVs are rare, extremely high-throughput is required with high sensitivity and specificity.

We report low-power, high-throughput optical trapping of single EVs using mass fabricated DNHs. This approach is label-free, using the optical signal and machine learning to accurately classify EVs from three different cell lines, non-malignant, non-invasive cancerous, and invasive cancerous. While greater accuracy will be required for clinical applications, this is a promising first step towards label-free diagnostics.

5.2 Double Nanohole Optical Trapping

The DNH provides an enhanced gradient force allowing for more stable trapping at lower powers compared to optical tweezers, as well as introducing a spatial confinement that reduces the effective trapping volume. The optical properties of the apertures used in these experiments are shown in in Figure 5.1.

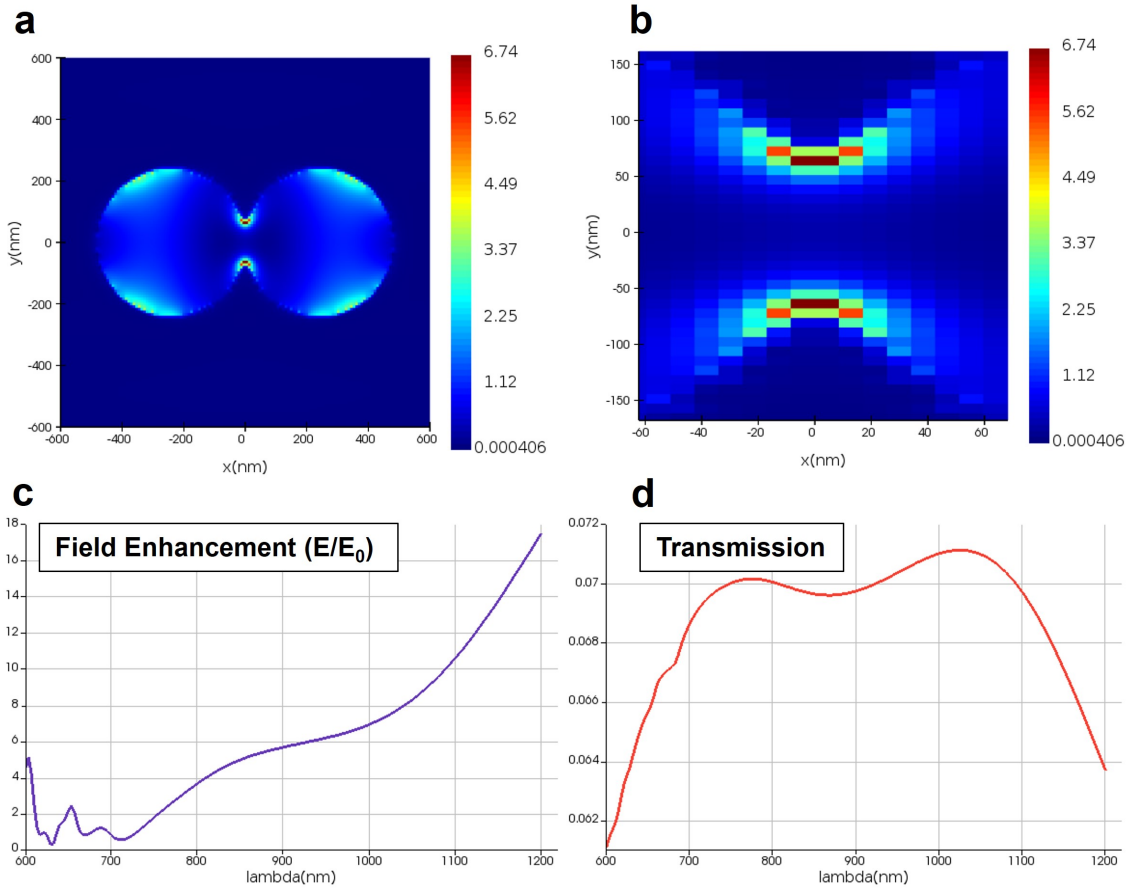

Figure 5.1: (a) FDTD field enhancement normalized to incident intensity of a 491 nm hole diameter and 114 nm cusp separation aperture and (b) zoomed in view of the cusp field enhancement. (c) Field enhancement and (d) transmission of the aperture from 600 nm to 1200 nm.

From Figure 5.1(d), the gap resonances are pronounced around 600 nm and 650 nm;however, the field enhancement at 980 nm is over 2.5× greater than at 650 nm.

Figure 5.2(a) shows representative trapping events for each of the EVs: MCF10A (non-malignant), MCF7 (non-invasive, cancerous), and MDA-MB-231 (invasive, cancerous). The number of trapping events for each EV sample are MCF10A (134), MCF7 (107), and MDA-MB-231 (76). Measurements were repeated over multiple days, on multiple DNHs, and from multiple EV isolations. A random selection of 24 traps of each EVs is shown in Figures 5.4, 5.5, and 5.6. Qualitative differences are readily seen in the trapping data, for example, MDA-MB-231 regularly showed a stronger initial step when trapped. There are also differences observed in the noise

amplitude and power spectral density which give information about the size, refractive index, and shape of the EV. A probability density function is fit to the 10 Hz low pass filtered signal showing the amplitude of the signal as well as a qualitative representation of the change in transmission through the aperture during trapping. The power spectral density with a Lorentzian fit is also shown for each signal, providing information about the trapping stiffness, which relates to the size of the trapped EV [3]. While the corner frequency does contain information about the size, shape, and refractive index of the particle, it is not used for classification here [46]. There are no statistically observed size differences between EVs, as can be seen in Figures 5.8(b) and 5.11, as well as Table 5.4. A simplified diagram of the optical tweezer is shown in Figure 5.2(b), a full review of the method may be found in past works [4, 142, 94]. The change in transmission through the nanoaperture for each line of EVs is shown in Figure 5.2(c). Due to dielectric loading of the nanoaperture, the transmission through the nanoaperture changes with a magnitude depending on the refractive index (RI) of the biomolecule. EVs are typically characterized as having an RI less than 1.42 [143, 144], which is close to the RI of PBS (1.34), leading to minimal changes in transmission. However, we show that DNH optical tweezers are sensitive enough to observe differences between EV cell lines. The percent change in transmission for MCF10A, MCF7, and MDA-MB-231 is highlighted in table 5.1 below and one way analysis of variance (ANOVA) results in table 5.5 show the statistical significance of the results. While the p value (2.2×10^{-7}) indicates a strong rejection of the null hypothesis (averages of the percent change in transmission are the same), it must be noted that the variance in MCF10A and MCF7 averages show significant overlap and cannot be used as a classification scheme.

Table 5.1: Percent change in transmission count, average, and variances for each EV.

EV	Count	Average (%ΔT/T)	Variance (%ΔT/T)
MCF10A	90	1.30	1.57
MCF7	47	1.44	1.70
MDA-MB-231	55	2.80	4.67

Previous studies have suggested that the surface charge of trapped EVs may influence the transmission signal, [145, 146, 147] with evidence indicating varying zeta potentials between cancerous and non-cancerous EVs [148, 149]. Of particular interest is the ease of trapping, with the time between turning on the laser and a single EV be-

ing trapped (latency) taking a few seconds. Stable trapping is achieved at low power (3.7 mW) to minimize sample heating and potential damage to the EV, but the laser power was increased to 9.7 mW for tens of seconds and there was no observed bursting of the trapped EV, allowing for higher strength trapping in the future. Considering a spherical particle of radius 35 nm, the diffusion coefficient in water is $6.3 \times 10^{-12}\ m^2/s$. It requires only 8 seconds for the EV to diffuse 10 μm. The laser was kept off for a minimum of 60 seconds to allow ample time for the EV to diffuse away and minimize the chance of trapping the same EV. To verify EVs weren't damaged during trapping, the laser was turned off after trapping to release the EV and videos of the trapping have been added to the database (see availability). The high thermal conductivity of the gold and low absorption at 980 nm tend the DNH to minimal heating Past works have confirmed that the EV is inside of the gap when trapped [141], adding an inherent upper limit to the size of the trapped EV. Figure 5.7 shows the average gap size is 116 nm, allowing for trapping of single exosomes and small ectosomes in mixed solutions containing small and large vesicles. A nanoparticle tracking analysis (NTA) intensity vs size plot is shown in Figure 5.8(a). An RMSD vs corner frequency plot is shown in Figure 5.8(b), showing a similar size/intensity trend, but no quantitative values are able to be obtained at this point. The size range of EVs in the solution was obtained from NTA and is shown if Figure 5.11.

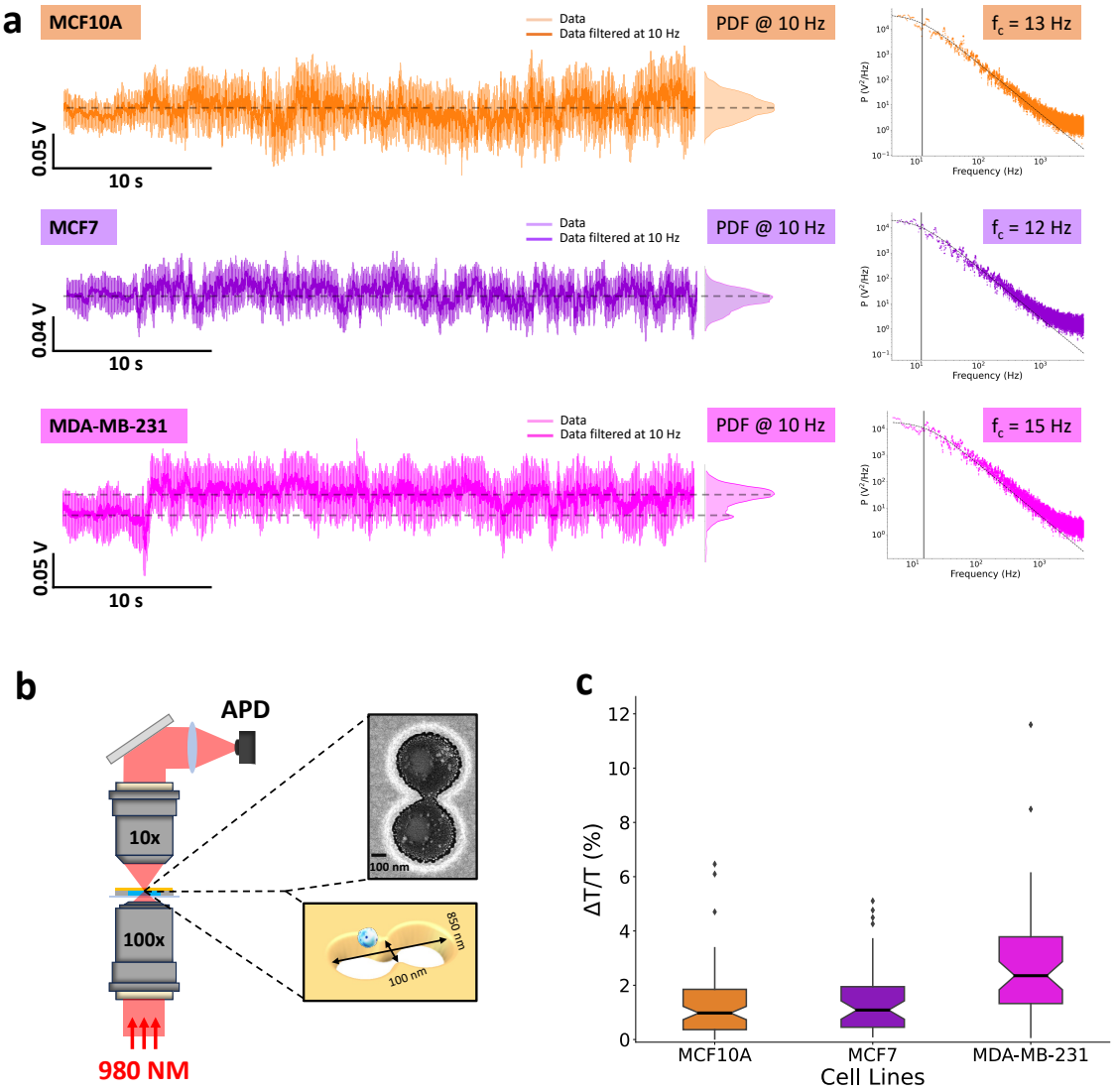

Figure 5.2: (a) Representative trapping signal, probability density function, and power spectral density boxcar average with Lorentzian fit for each line of extracellular vesicles. (b) Simplified diagram of optical nanotweezer setup with a scanning electron microscope image of a double nanohole and illustration of an exosome being trapped. (c) Change in transmission percentage through the double nanohole for each line of extracellular vesicles.

5.3 Classification

A 1D convolutional neural network (CNN) was used to classify the trapping signals. The full data sets and code are published, see availability below. CNN's have

precedent in classifying optical tweezers signals, but are largely used in image based deep learning [121, 150, 151, 152, 153]. We applied a simple 1D CNN architecture to classify the transmitted optical signal of EVs. Typically, deep learning models for computer vision have achieved tremendous success using feature learning. Unlike these models, CNNs do not require features to be identified a priori to model training: feature learning and classification are jointly learned as a result of multiple layers in the model (pooling, convolution, normalization, etc.). 1D CNNs are useful for taking short-term temporal features and identifying long-term patterns. Initial layers of CNNs identify simple features such as peaks and dips in time series data or edges in images using a Gabor-like filter. Further processing in the CNN layers identifies increasingly complex patterns until the final layer where discriminative features can be identified. Compared to a deep CNN, where the number of training parameters is given by $w \times h \times c$, where w and h are the width and height of the filter and c is the depth of the convolutional filter (including time dimensions), the 1D CNN has only c training parameters allowing for better results when training with smaller data sets. Past studies have shown 1D CNNs to have better performance for applications with limited labeled data and high signal variance [154, 155, 156, 157, 158, 159]. While traditional analysis methods (RMSD, PSD) are unable to capture the differences between the EVs, the CNN is able to extract features that are not readily apparent. Figure 5.3(a) shows a conceptual overview of the CNN model. The MATLAB function "trainNetwork" was used for creating the neural network. The data sets were built to ensure a common signal length for training and an equal amount of trapping events for each EV (50 each). Each file of trapped data was split into one second segments, preserving the temporality of the signal. The segments were downsampled from 100 kHz to 500 Hz to accentuate the main features of the signals. In addition to avoiding bias from signal length, segmenting the data works to the advantage of 1D CNNs ability to learn from short-term data to identify long-term temporal features. The segmented frames were then divided into training, validation, and testing with a 50%, 30%, and 20% ratio. The number of segments used for training, validation, and testing were 1220, 732, and 488. Each segment was only used once, ensuring that there was no contamination between training, testing, and validation. Table 5.2 shows the layers used in the CNN training and their respective sizes. Figure 5.3(b) shows the confusion matrix of our trained model with the precision, recall and F1 score of each EV shown in Table 5.3. Overfitting of the model is unlikely for two reasons. The model performs well on data that was kept out of the training and the

learning curves seen in Figure 5.12 show that the model stops learning before the validation and test performance get worse. Repeated training with the same data split (50%, 30%, 20%) but different segments in each grouping gave close results to the model shown here, within a nominal percentage difference in accuracy. The transmission change at the point of trapping was not included in the data for the model as it could not be ensured that the pre-trap information would not influence the feature identification.

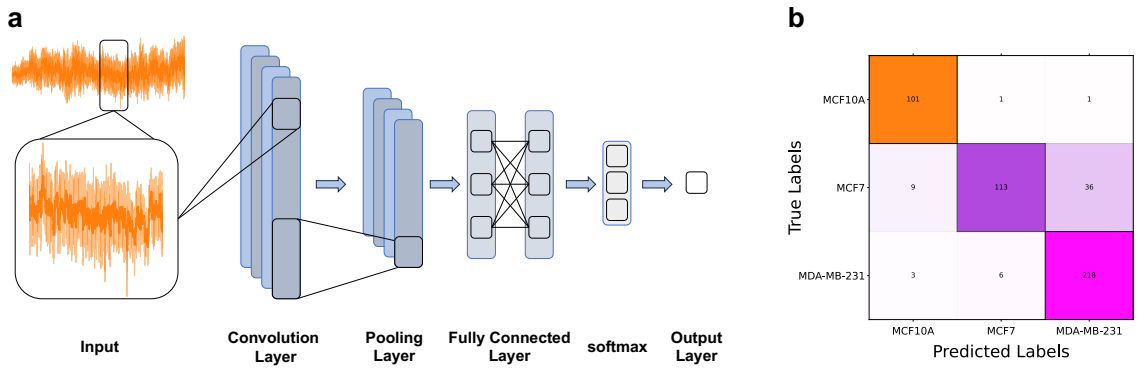

Figure 5.3: (a) Conceptual overview of the CNN training and classification of optical signal. (b) Confusion matrix of CNN model with a training/validation/testing split of 50%, 30%, and 20%.

Table 5.2: CNN layers

Layer	Size
Input	N × 1
Convolution (filterSize: 5, numFilters: 32, padding: casual)	N × 32
GlobalAveragePooling	1 × 32
fullyConnectedLayer; softmax	1 × 3
Output	1 × 1

Table 5.3: CNN training results for each EV.

EV	Precision	Recall	F1 Score
MCF10A	0.893	0.981	0.935
MCF7	0.942	0.715	0.813
MDA-MB-231	0.855	0.960	0.905

Precision is the ratio between the true positive classifications and all of the positive

classifications $\frac{TP}{TP+FP}$, or the measure of how many classifications were true out of all EV classifications. Recall is the measure of the model correctly identifying true positives $\frac{TP}{TP+FN}$, in this case the recall score tells how many EVs were correctly classified. The F1 score provides a balanced assessment between precision and recall, defined as $\frac{2\times precision\times recall}{precision+recall}$, thereby measuring how effectively the model makes the trade-off between precision and recall. The overall test accuracy from the initial model split was 88.52%. Four files from each EV dataset were removed from the training datasets for external testing, but otherwise underwent the same segmenting and filtering process as the training sets, thus there were 205 segmented data sets tested. Additional testing was performed with data kept out of the initial model split was performed with accuracies of 93.33%, 86.44%, 100.00%, and 94.12%, and the confusion matrices can be found in Figure 5.13. Each test was performed with segments from each EV type.

5.4 Extracellular vesicles

After isolating the EVs from conditioned media of the cells via ultra-centrifugation, EVs were characterized via western blot for EV markers, CD9 and CD63 and cell lysate contaminant, Calnexin. Western blot showed that CD9 and CD63 are abundant in EVs and not in the cell lysate, seen in Figure 5.9. Nanoscale flow cytometry can be employed for detection of EVs between 80 nm to 1000 nm at single particle resolution [160, 161, 162]. Here, isolated EVs were analyzed for CD63 marker with nanoscale flow cytometry using 405 nm violet side scatter trigger and showed that CD63 is abundant on the surface of EVs, seen in Figure 5.10. The nanoparticle tracking analysis sizing data is shown in Figure 5.11 and Table 5.4.

5.5 Discussion

Past works using atomic force microscopy and machine learning have shown mechanical variations of EVs that can be used to predict parent cells [163]. It is possible that these variations are also responsible for the fluctuations that allow for classification in our experiments. While the size of the EV can influence the optical signal, Figure 5.9(b) shows that there is significant size overlap between all of the EVs so this cannot be used for classification alone.

The levels of cancer cell-derived EVs in humans is low in comparison to healthy EVs. One study shows a level of 23-1900 cancer-derived EVs per mL of blood per 1 mm^3 of tumour [164]. This suggests that a substantial increase in cancerous EV concentration would not be observable until the tumor exceeds a size larger than 50 cm^3, making early stage detection difficult. The achieved specificity in identifying whether a trapped EV is cancerous or non-cancerous is 98.06%, whereas the specificity of classifying the trapped EV as either MCF10A, MCF7, or MDA-MB-231 is 96.5%, 97.9%, and 85.3%. Clinical diagnostics requires a high specificity (¿99%), however current on market exosome diagnostics have achieved 89% [165]. With improvement in the accuracy of our model, the next steps involve trapping EVs using a mixed solution comprising a small amount of cancerous EVs and non-malignant EVs. Then, using the trained CNN model, classification of the trapped signal can be performed to determine the ratio of cancerous to non-cancerous EVs, and detection capabilities at low concentration. Improvements in classification may come from a multi layer network or exploring other models. Another approach would be to use Allan variance analysis to classify the EVs on the basis of the "noise" characteristics [166]. DNH optical tweezers have shown precedent working in 'dirty solutions' with capabilities to distinguish between different proteins [167].

Compared to prior ONT experiments involving other biomolecules (DNA, proteins, peptides), and nanoparticles (quantum dots, upconverting nanoparticles, nanocrystals), the throughput of EV trapping is 20x faster (on the order of seconds) at 10x lower concentration (0.1 ug/uL). In 6 hours, it was possible to obtain 75 distinct trapping events. Throughput is currently limited to human factors involving fine alignment of the stage, laser control, and data organization between trapping events, all of which could be automated in the future for even higher throughput. Various factors affect the ability to trap including thermophoresis [168]. In the case of EVs, it is found that they are less thermophobic than proteins, which would lead to faster trapping, especially considering the lower induced temperature from the low per trapping [169]. It is possible to "trap" an EV larger than the DNH gap; however, qualitatively this was a rare event and is characterized by a distinct slow decrease in APD signal and a large change on the camera. Thus it is highly likely only EVs smaller than the DNH that are trapped. While a fluidics system was not necessary to trap the EVs, integration of a fluidic system could further improve the time-to-trap and enable additional functionality for studying EVs in different solutions after trapping, or for

sorting EVs after trapping. To apply this platform for clinical work, the throughput needs to be scaled extraordinarily, to the level of 10 million traps, with a limit of detection of 100 parts per billion. As it stands now, trapping and exporting the data takes prohibitively long to trap more than a few hundred in 8 hours. Possible ways to increase the throughput is trapping with arrays of nanostructured fiber tip trapping, automation, or microfluidic integration. An added benefit of the DNH platform is the ability to isolate specific EVs for further characterization elsewhere, such as electron microscopy [141], or sorting using a combined nanopore/optical tweezer [133]. Isolating specific EVs allows for analysis of the contents of the EV (proteins and nucleic acids), for determining their origins, or prognostics.

5.6 Conclusion

We have shown that DNH optical tweezers are capable of easily trapping extracellular vesicles without damaging them. Differences in EVs are identified through changes in transmission related to the dielectric properties, but using a convolutional neural network to identify less readily apparent features, accuracy greater than 85% is achieved in classifying trapped EVs into specific cell lines. This lays the groundwork for future work with spiked samples of low concentration cancerous EVs, and with improvements in throughput, clinical applications. One potential future avenue would be to investigate CNNs on dielectric nanoparticles of various composition, size, and shape to obtain some physical relation to the CNN parameters.

5.7 Acknowledgements

The authors acknowledge the use of the facilities of the Centre for Advanced Materials and Related Technologies. The authors acknowledge funding from the NSERC Discovery Grants RGPIN-2023-04108 and RGPIN-2020-04641. The authors also thank Dr. Russ Algar for the use of their NanoSight instrument for nanoparticle tracking analysis of extracellular vesicles.

5.8 Materials and methods

5.8.1 Isolation of EVs

To perform EV isolation using ultracentrifuge, 5×10^6 cells were seeded in 15 cm plates in 15 ml complete media for each condition. After 48 hours, conditioned media were harvested and spun at 300 *g for 10 min, at 4 °C to remove dead and floating cells, then at 2500 *g for 30 min, at 4 °C, to remove cell debris and apoptotic bodies. Next, the supernatant was transferred to polyallomer 38.5 ml open-top ultracentrifuge tubes (Beckman Coulter) and was centrifuged at 10,000 *g for 30 min, at 4 °C, to isolate large EVs. A SW32Ti Rotor (Beckman Coulter) was used in an Optima XPN-100 ultracentrifuge (Beckman Coulter). The supernatant was transferred to new ultracentrifuge tubes and ultracentrifuged at 100,000 *g for 70 min, at 4 °C, using the same ultracentrifuge tubes and rotor as above. The resulting pellets were washed by resuspension in 0.02 μm filtered Phosphate Buffered Salin (PBS) (MultiCell), and re-pelleted in the same conditions as above. EV pellets were resuspended in 30 μL 0.02 μm filtered PBS and freshly used.

5.8.2 Flow cytometry analysis of EVs

After isolating the EVs via ultracentrifuge, 10 μL of freshly isolated EVs was placed in a 1.5 ml tube and incubated with 1.1 μg CD63-FITC (abcam #ab18235) and mouse-IgG1 isotype control (abcam #ab91356) antibody for 30 minutes in the dark at room temperature. Then, the EV samples were diluted 1:10 in 90 μL 0.02 μm filtered PBS (MultiCell) and transferred into a flat bottomed 96 well plate. The analysis was conducted on a CytoFLEX S flow cytometer (Beckman) utilizing MilliQ water (ultrapure filtered and deionized water from the MilliQ water purification system) as the diluent in place of sheath fluid. The instrument was configured with the following parameters: triggering on 405 nm violet side scatter, violet side scatter detection set to 1027, and a slow speed setting for 60 seconds (analyzing 10 μL of sample per minute). Manual gating was employed to isolate populations of interest, referencing isotype controls. Gain settings were adjusted as follows: VSSC: 100, and FITC: 500.

5.8.3 Nanoparticle Tracking Analysis of EVs

Isolated EV obtained from three cell lines, MCF10A, MCF7 and MDA-MB-231, underwent a dilution of 5:1000 in 0.02 μm filtered Phosphate Buffered Saline (PBS). Subsequently, the NanoSight LM10 equipped with a blue 488 nm laser (Malvern Panalytical) facilitated the assessment of the quantity and dimensions of the diluted EVs. To ensure accurate measurements, three 30-second readings were captured employing a syringe pump to sustain EV movement within the chamber at a velocity of 40 μL/min. The camera level was adjusted to level 14. A consistent detection threshold of 5 (AU) was maintained throughout the analysis process which determines the minimum intensity for a scattered light signal to be detected as a real signal [170]. Data analysis was performed using NTA software version 3.4.

5.8.4 Western Blot

After harvesting the conditioned media for EV isolation, the remaining cells were washed with PBS twice, and then 200 μL of ice-cold RIPA buffer (Thermo Scientific #PI89900) was added to each plate. After scraping the cells with a cell scraper, cells were collected in a 1.5 ml tube and agitated on a rotating shaker for 10 min at 4 °C. Then, the tube was centrifuged at $16{\times}10^6$ for 10 min at 4 °C. After collecting the supernatant and discarding the pellet, the protein concentration of the cell lysate and the isolated EVs were measured using Pierce™ Rapid Gold BCA Protein Assay Kit and Micro BCA™ Protein Assay Kit (Thermo Fisher Scientific), respectively, according to the manufacturer's instructions. Following the protein concentration quantification, 13 μg of protein was combined with 25% loading buffer (Novex Life Technologies), and Milli-Q water was added to reach the final volume of 40 μL. The samples underwent boiling at 95 °C for 10 minutes and were subsequently loaded onto Bolt 4–12% Bis-Tris Plus gradient gels (Thermo Fisher Scientific). Gel electrophoresis was performed at 200 V for 30 minutes using MES (50 mM MES (Sigma), 50 mM Tris Base, 0.1% SDS, 1 mM EDTA, pH 7.7) running buffer. All reagents were obtained from Fisher Bioreagents unless otherwise specified. Following gel electrophoresis, proteins were transferred onto nitrocellulose 0.45 μm membrane (BioRad) through wet transfer (190 mM glycine, 25 mM Tris Base). Post-transfer, membranes were blocked in 5% milk in TBS-T (20 mM Tris base, 160 mM NaCl, 0.1% Tween) for 1 hour. Primary antibodies were applied overnight at 4 °C in 1% milk at the dilutions as follows: CD9 (EMD Millipore #CBL162) 1:1000 μL CD63 (BD Pharmingen #556019)

1:1000 μL, Calnexin (Abcam #AB22595) 1:5000 μL, β-actin (Sigma #0000120485) 1:2000 μL. Membranes underwent three washes of 10 minutes each in TBS-T. Secondary Licor IRDye 680RD and IRDye 800CW antibodies were applied in 1% milk for 1 hour in the dark, followed by repeating the washing steps. Membranes were imaged on the Licor Odyssey®CLx following the manufacturer's guidelines, employing Image Studio Lite software (5.2).

5.8.5 Colloidal Lithography of Double Nanoholes

DNHs were fabricated using a modified approach from past works [67]. Standard microscope slides (Fisherbrand 12-550C, 75×50×1.0 mm) were cut into thirds using a diamond scribe, cleaned by sonicating in ethanol for ten minutes, and dried under nitrogen. A solution was made of 10 μL of 600 nm polystyrene beads (Alpha Nanotech) and 1 mL of ethanol. Using 10 μL of the polystyrene-ethanol solution, a zig-zag pattern was deposited on the microscope slides and left overnight. Once the ethanol evaporated, the coated slides were covered with 7 nm of titanium and 70 nm of gold using a sputter deposition system (MANTIS QUBE). Polystyrene was removed from the metal using tape lift off, plasma cleaned for ten minutes, and stored in ultrapure water. We currently produce 36 chips per fabrication run, but this approach is highly scalable.

5.8.6 Trapping Solution

A 24×60-1 microscope cover glass (globe Scientific Inc.) was cleaned using isopropyl alcohol and dried under nitrogen. An image spacer (Grace Bio-Labs GBL-654008-100EA) was placed in the center of the coverslip and 9.37 μL of the solution was pipetted into the spacer. The gold DNH sample was placed on top of the spacer so the gold is in contact with the solution. EVs were diluted in phosphate buffered saline (PBS) to a concentration of 0.112 μg/μL (MCF10A), 0.494 μg/μL (MCF7), and 0.191 μg/μL (MDA-MB-231).

5.8.7 Software, Statistical Analysis, and Data Acquisition

5.8.7.1 Optical Nanotweezers

All data analysis was performed using custom python code. Data was collected at a sampling rate of 100 kS/s. Total number of trapping events analyzed is 317. The

power spectral density was calculated using a 5 second window of the trapped signal and then a boxcar average is taken with a weight of 10. Lorentzian function of the form $\frac{A}{f^2+f_c^2}$, where f_c is the corner frequency and is fit to the boxcar average PSD. The root-mean-squared-deviation (RMSD) is calculated by dividing the same 5 second portion of the trapped signal into sections based on a window length of 5000. The RMSD is then divided by the mean of the trapped signal and an average of all the sections is taken. To normalize the values, an average of all laser RMSD's was subtracted from each trapped RMSD.

5.8.7.2 Convolutional Neural Network

MATLAB convolution1dLayer was used as the platform for sequence classification. A filter size of 5, 32 filters, 1 feature, 3 classes, mini batch size of 5, 200 epochs, and learning rate of 0.001 was used for the training. The files are split between training and testing and split into smaller time segments (1 second). Additional files were kept outside of the model generation and tested afterwards. The optical signal was normalized to remove the DC offset due to day-to-day differences and small aperture variations as well as to enhance the features present in the data. The normalization was of the form Voltage = 10*(Voltage-mean(Voltage)) + 2*(mean(Voltage)), this allows for amplification of the fluctuation features in the data and the amplitude of the signal. The normalized data was then downsampled to 500 Hz from 100 kHz and all files were ensured to have the same length.

5.9 Supporting Information

A selection of 24 trapping events is shown for each of the three EVs in Figures 5.4, 5.5, and 5.6.

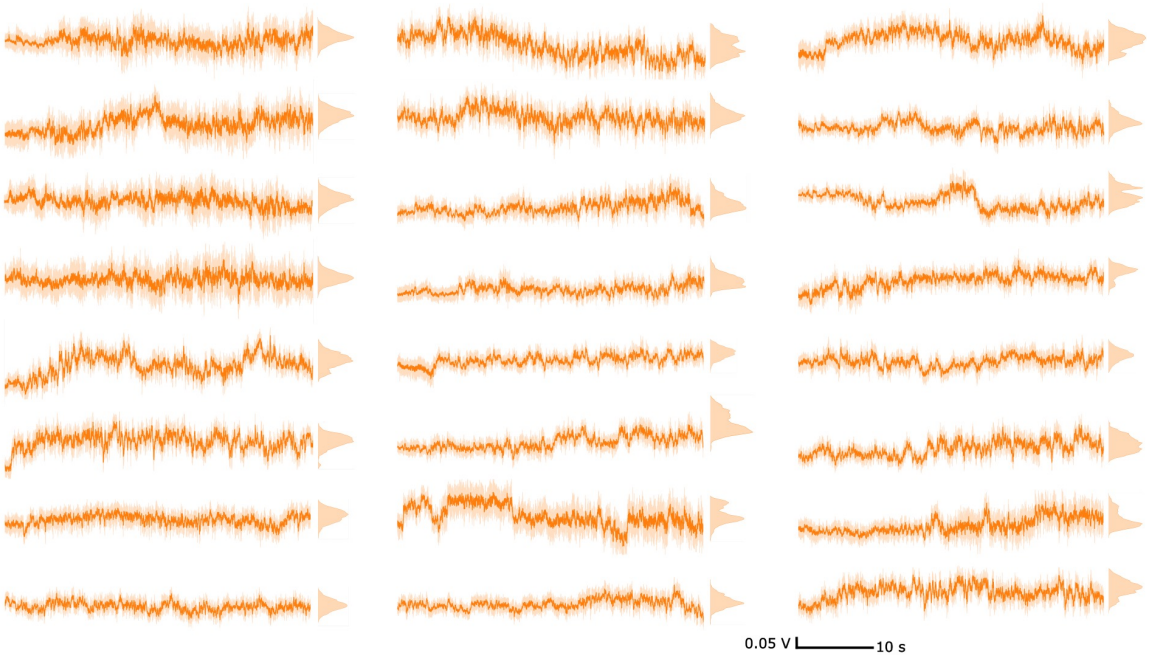

Figure 5.4: Trapping events and probability distribution function for MCF10A.

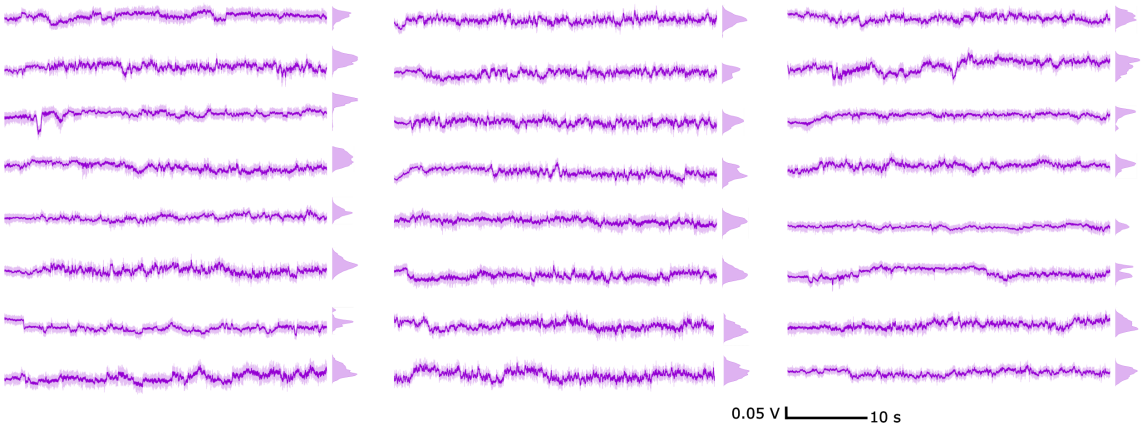

Figure 5.5: Trapping events and probability distribution function for MCF7.

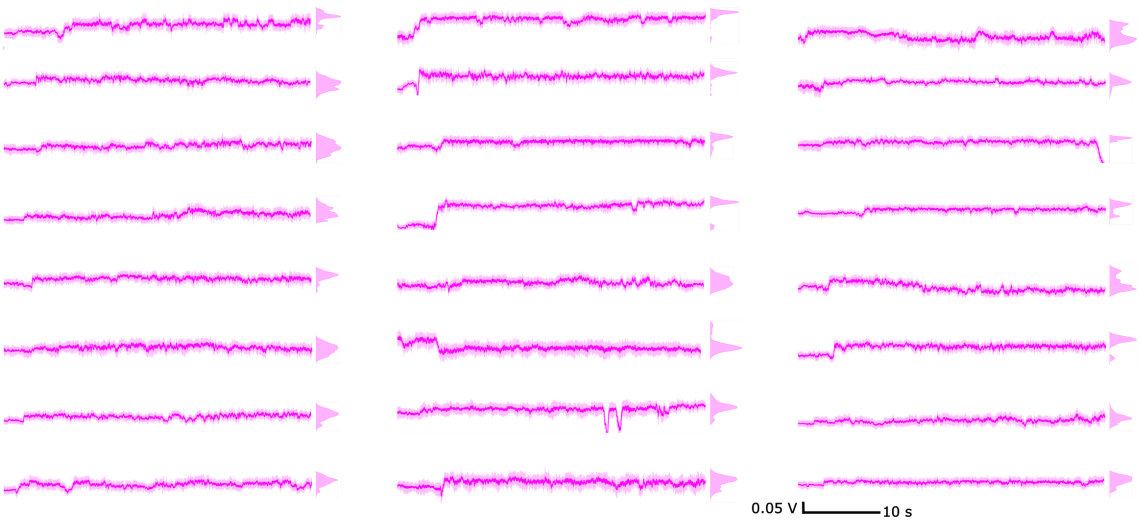

Figure 5.6: Trapping events and probability distribution function for MDA-MB-231.

The variation in DNHs fabricated colloidally is shown in Figure 5.7 along with a sample of SEM images. As is the case in optical tweezers, with sufficient power, the lower size limit of trapping is only dependent on incident power and it is expected that single proteins are able to be trapped using these DNHs. The upper size limit is determined by the physical constraints of the DNH, approximately 116 nm.

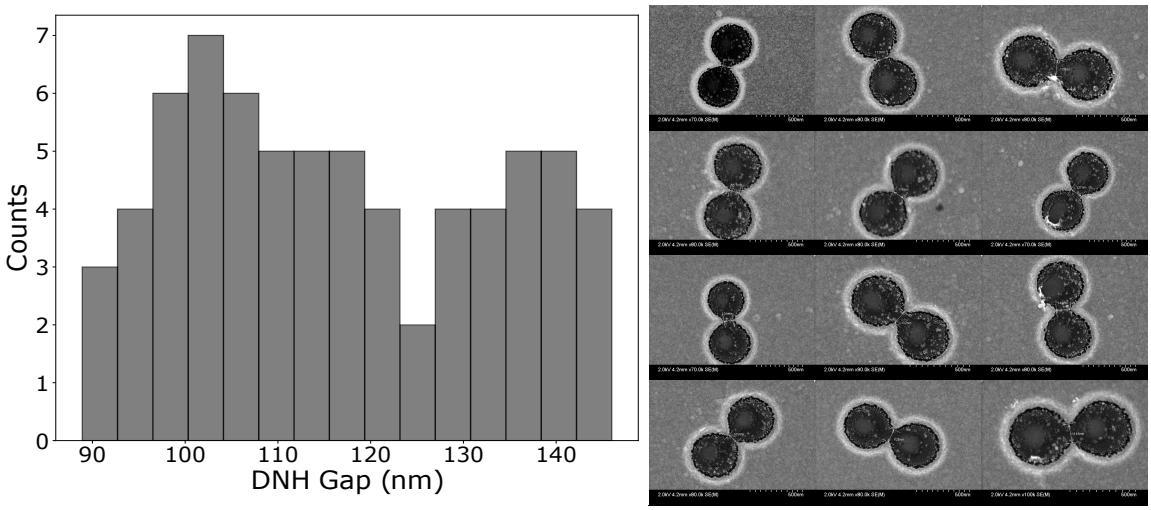

Figure 5.7: Histogram of gap values of colloidally fabricated DNHs and a sample of SEM images.

Past works have shown DNH optical tweezers can determine the radius of single

proteins in the trap [3, 66]. This theory can be applied to the trapped EVs as well, with the corner frequency having an r^2 dependence and the RMSD having an r^3 dependence, seen in equations 5.1 and 5.2 respectively, where κ is the trapping stiffness, γ is the damping coefficient, α is the polarizability, r is the radius, η is the viscosity, and E is the electric field.

$$f_c = \frac{\kappa}{\gamma} = \frac{\alpha \nabla |E|^2}{6\pi\eta r} \propto \frac{r^2 \nabla |E|^2}{6\pi\eta} \tag{5.1}$$

$$RMSD \propto \frac{1}{2} r^3 |E|^2 \tag{5.2}$$

The RMSD and corner frequency can then be related as $RMSD = a f_c^{3/2}$ and the experimental data fit to this. The RMSD is a characterization of the optical scattering, or the optical size. Conversely, the corner frequency is a characterization of the optical size and hydrodynamic size as the hydrodynamic drag is considered. Figure 5.8a shows that the relation between optical size and hydrodynamic size using nanoparticle tracking analysis and can also be seen in the DNH measurements in Figure 5.8b.

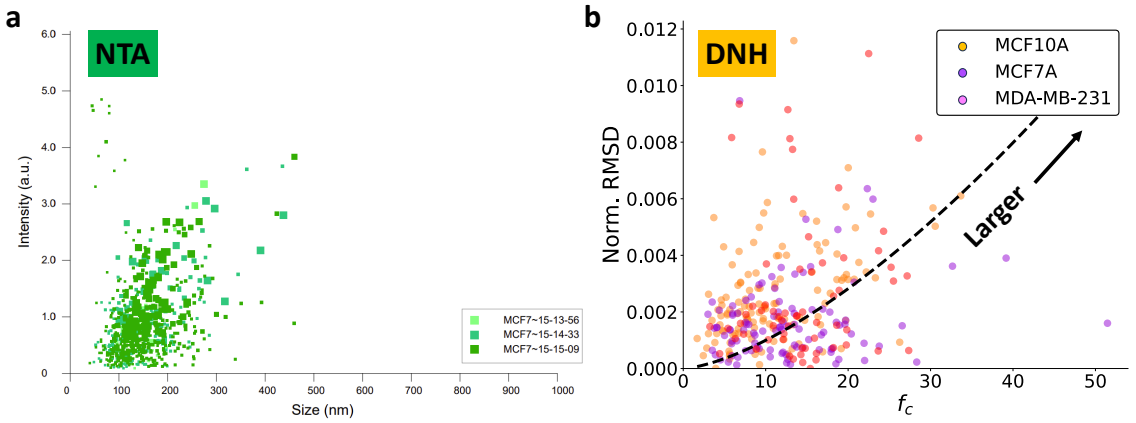

Figure 5.8: (a) Nanoparticle tracking analysis of MCF7 EV sample. (b) RMSD vs corner frequency analysis of all trapping events.

Figure 5.9 shows that the EV pellet isolated contains the EV specific markers CD9 and CD63 while the cell lysate contains little to no markers. Conversely, we show that there is no cell contamination from the cell lysate-specific protein marker Calnexin.

The β-actin is used to show that the loaded protein is similar from one well to another as an internal control.

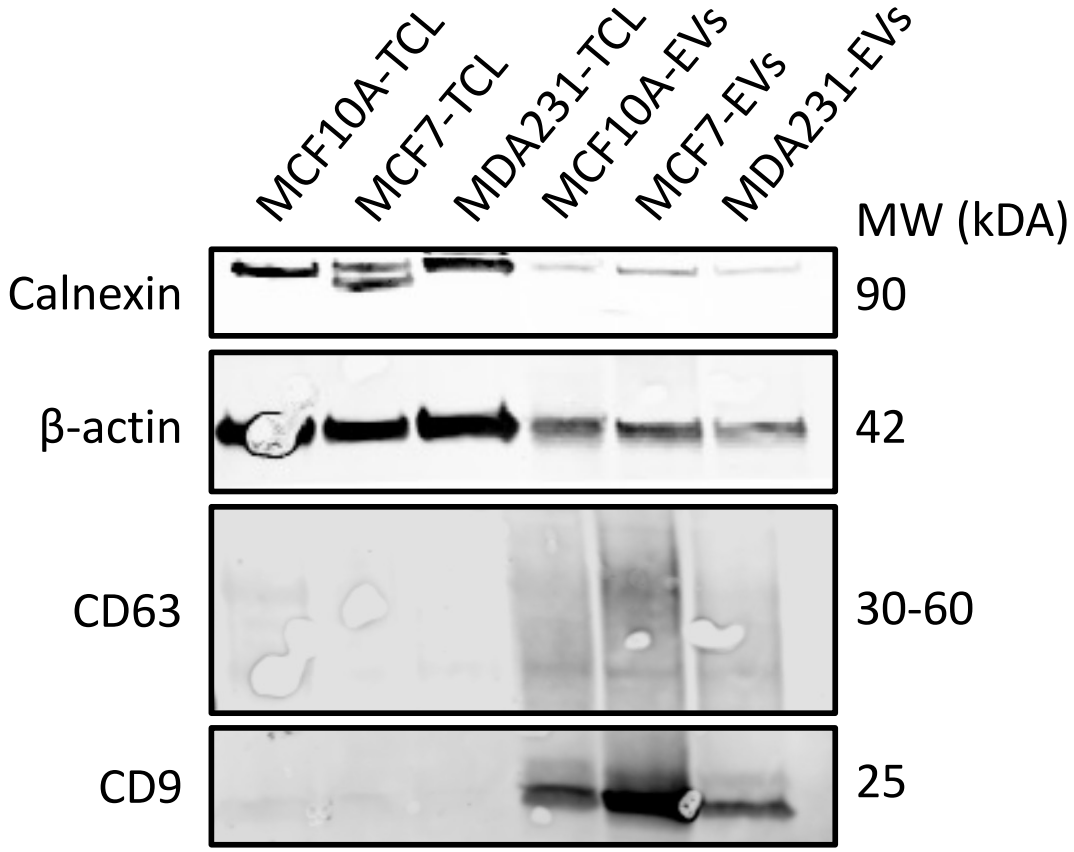

Figure 5.9: Gel electrophoresis indicating EV isolation was successful.

Figure 5.10 confirms that EVs have been isolated via ultracentrifugation. These EVs were labelled with the CD63 antibody. However, CD63 is not a universal marker so not all EVs are CD63 positive, causing variation in quantity between cell lines. MCF10A, MCF7, and MDA-MB-231 CD63 positive EVs are 7461, 2901, and 18253 respectively.

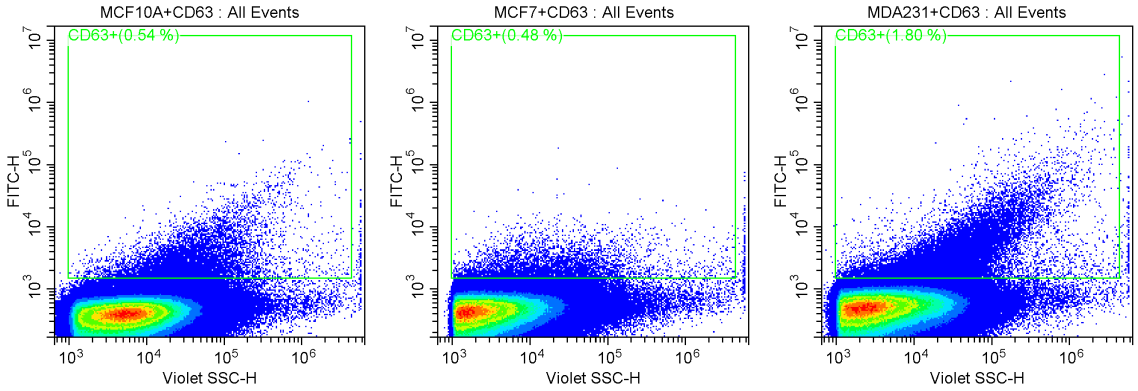

Figure 5.10: Flow cytometry results of CD63 antibody labelling confirming EV isolation by ultracentrifugation.

Figure 5.11 shows the concentration and size range of EVs used in trapping while the statistics are shown in Table 5.4.

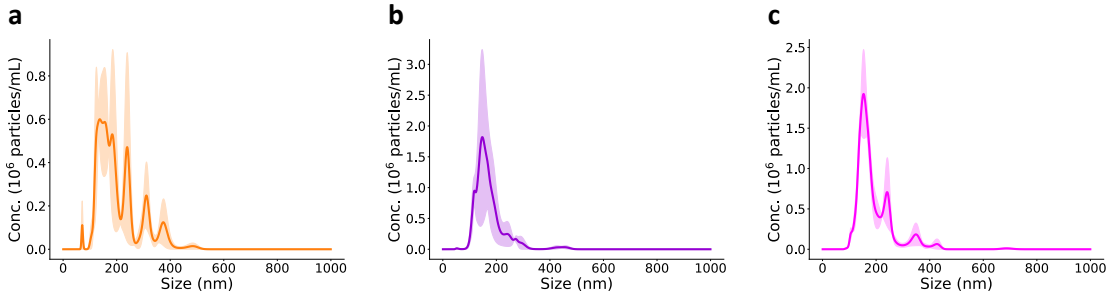

Figure 5.11: Nanoparticle tracking analysis concentration vs size results for (a) MCF10A, (b) MCF7, and (c) MDA-MB-231.

Table 5.4: Nanoparticle tracking analysis of EVs size statistics.

EV	Mean (nm)	Mode (nm)	SD (nm)
MCF10A	203.6 ± 11.1	188.8 ± 28.5	74.9 ± 8.1
MCF7	174.2 ± 2.8	126.6 ± 10.1	61.3 ± 7.9
MDA-MB-231	192.6 ± 2.5	182.9 ± 29.6	72.3 ± 6.8

Table 5.5: ANOVA results for percentage change in transmission.

Source of variation	Sum of Squares	DoF	Mean Sum of Squares	F	P-value	F critical
Between Groups	82.696	2	41.348	16.634	2.2E-07	3.043
Within Groups	469.804	181	2.486			
Total	552.500	191				

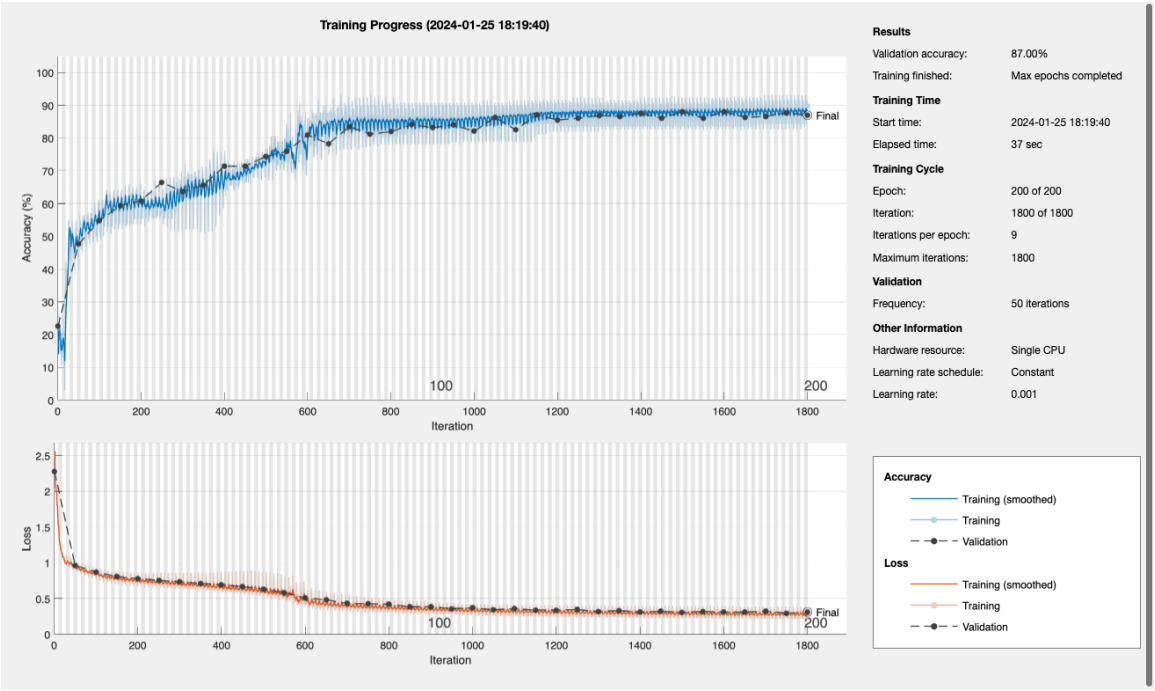

Figure 5.12: Training progress accuracy and loss for CNN.

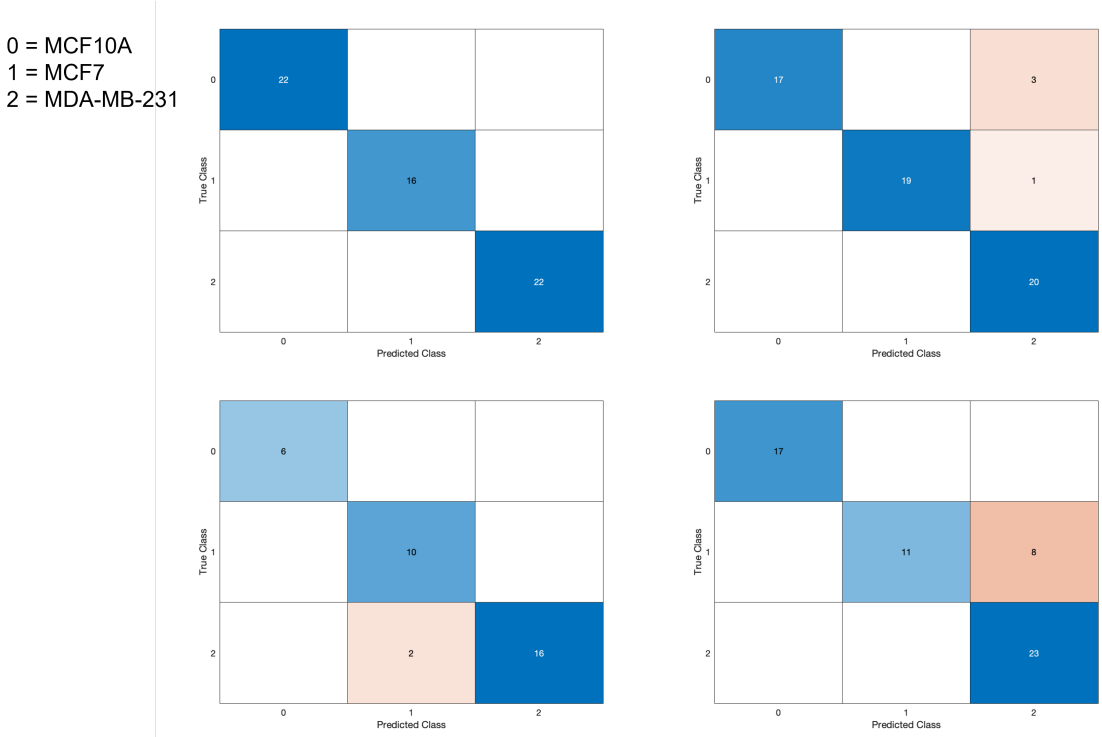

Figure 5.13: Confusion matrices for external testing of the CNN.

Chapter 6

Other Works

In this Chapter I will detail other work I have performed during my Master's degree, successful or not, I believe it will be helpful to anyone performing this work in the future.

6.1 Pulse Laser Trapping

6.1.1 Extraordinary Acoustic Raman Spectroscopy

Conventional Raman spectroscopy provides a vibrational spectrum that is unique to the analyte, essentially a fingerprint. Absorption of electromagnetic radiation facilitates transitions between different energy states and provides information about structure [171]. Raman spectroscopy is typically limited in applications for nanoparticles and small biomolecules such as proteins due to limited spectral resolution and high frequency modes. Past work in the Nanoplasmonics Lab developed a technique called Extraordinary Acoustic Raman Spectroscopy (EARS) that is able to measure the high frequency vibrational modes of single proteins. Two colinear lasers are used to trap the protein in the optical nanotweezer, once trapped, one of the lasers is tuned to different frequencies to create a "beat" frequency. When the beat frequency is resonant with the vibrational mode of the protein, an increase in the root mean square deviation of the trapped signal is seen [172].

6.1.2 New Approach

The EARS system was an incredibly powerful and useful method for obtaining the vibrational modes of proteins and "fingerprinting" them; however, it had issues with reproducibility and was complex to setup. An alternative approach is to combine two pulse laser beams, one of which is on a translation stage to delay the pulse. In theory this should create a similar "beat" frequency to EARS and excite the vibrational modes. A schematic of the setup is shown in figure 6.1.

A Calmar cfl-04rff laser is used (780 nm, 90 fs pulse width, 80 MHz repetition rate) for trapping. The beam is split using a beamsplitter and reflected using two retroreflectors. One of the retroreflectors is mounted on a translation stage and the other is stationary. The split beams are recombined and aligned so that when the translation stage is moved, the beams stay colinear. If the two beam paths are exactly the same distance, the pulses should overlap. As the translation stage is moved backwards, one of the pulses will begin to separate from the other. The speed of light is 299792458 m/s and the translation stage moves a maximum of 5cm, in 1 μm increments. This gives a maximum delay of 334 ps. Note the delay distance is multiplied by 2 as the path has to return the same distance.

$$\frac{1}{3E8}\frac{s}{m} \cdot 0.1\ m = 334\ ps \tag{6.1}$$

$$\frac{1}{3E8}\frac{s}{m} \cdot 1E-6\ m = 3.33\ fs \tag{6.2}$$

This gives a minimum frequency resolution of 2.994 GHz and a maximum of 300.3 THz: giving a very large probe range that covers the EARS spectrum. Noting that 80 MHz is a period of 12.5 ns, so there are no issues with the delay greater than the repetition rate.

6.1.3 Literature

Pulse lasers have been used in traditional optical tweezers to overcome trapping size limitations of continuous wave (CW) lasers due to their extremely high peak powers imparting large gradient forces [173, 174]. What we must consider when adding nanostructures to enhance trapping with a pulse laser is that the heat generation will be significantly higher. Roxworthy and Toussaint demonstrated for the first time

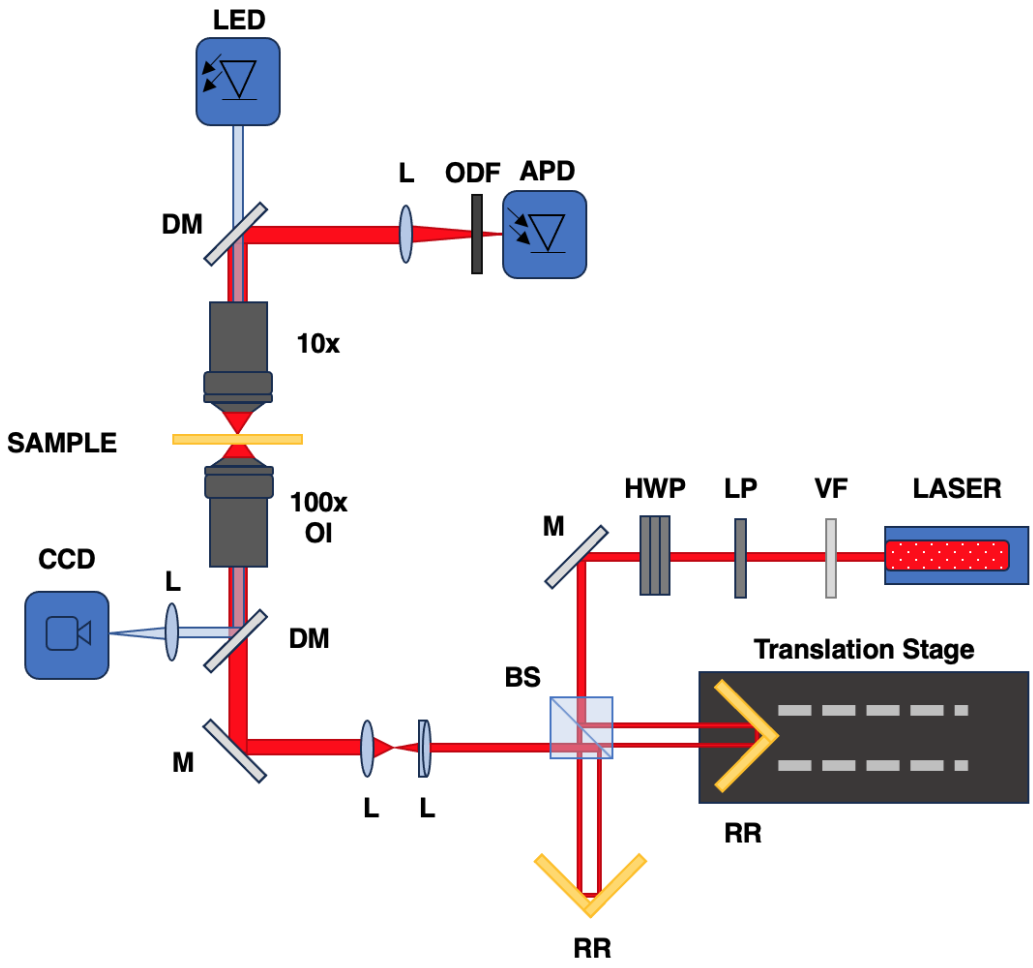

Figure 6.1: Pulse laser trapping setup: APD: Avalanche Photodiode. ODF: Optical Density Filter. LED: Light Emitting Diode. L: Lens. DM: Dichroic Mirror. M: Mirror. CCD: Charge-Coupled Device. OI: Oil-Immersion. LP: Linear Polarizer. HWP: Halfwave Plate. RR: Retroreflector. BS: Beamsplitter. VF: Variable Filter

optical trapping with a femtosecond laser (100 fs, 80 MHz) using gold bowtie nanoantenna arrays (BNAs) [175]. They found a 2x increase of trap stiffness when compared to CW NOTs. We must note that the particle they trapped was a 1.2 μm bead. They went on to trap an 80 nm Ag nanoparticle, measuring the second harmonic generation at an average input power of 60 μw. Two things are important in their results: in both the microbead and Ag nanoparticle, the trap caused the BNAs to fuse with the trapped particle, and the nanostructures were inverted from our configuration. The gold antenna arrays were formed as islands on a glass substrate, allowing for more light to be transmitted than absorbed, mitigating heating effects that would be present in our template stripped method. The fusing of the particle can most likely be attributed to the high peak powers melting the gold, when the particle is between the melted gold and laser, the gold solidifies while attached to the particle. In the case of biomolecules, this is detrimental as we need the structure to remain intact to study it, additionally, if the laser is strong enough to melt gold, then it will most likely destroy the biomolecule before it can even be trapped.

Shoji et al. demonstrated reversible trapping of DNA micropatterns on gold nanopyramid dimer arrays [176]. An 80 MHz, 120 fs, 770 nm laser was used to excite the pyramids and trap 48.5 kilobase pair (kbp) DNA, it should be noted that a conversion shows this is equivalent to 1794.5 kDa (much larger than any protein we trap). It is also important to note that it was not individual DNA loops that were trapped, but multiple that formed a ring pattern.

These are the only two results in the literature that have shown nanoaperture optical trapping with a femtosecond laser.

6.1.4 Results

Typical CW trapping in our lab uses 10 mW power for trapping, so the first attempt at fs-trapping utilized an average power of 10 mW (peak power >1 kW). SEM images from before and after trapping showed the cusps of the apertures had changed from a 25.3 nm distance to a 132 nm distance as shown in figure 6.2. The next experiments focused on trying to trap at decreasing power levels, however in CW trapping there is a minimum power needed for trapping. This creates a delicate balance with a pulse laser as the peak power is much higher than the average power, but the peaks seen are on the femtosecond scale. Using a continuously variable reflective filter at the

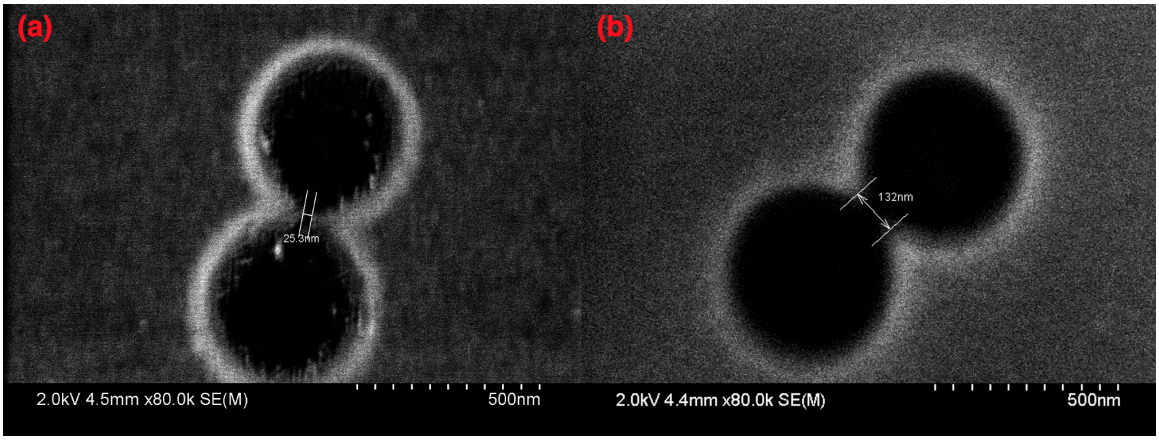

Figure 6.2: Scanning electron microscope images of DNH apertures before and after attempting to trap with 10 mW pulse laser. (a) before. (b) after.

start of the laser path, trapping was tested for 7.5 mW, 5 mW, 2.5 mW, 1 mW, 750 μW, 500 μW, and 250 μW. For all of these cases, 20 nm polystyrene was the particle of interest and in all cases, I was unable to trap it. To rule out the possibility that the samples were the issue, 20 nm polystyrene was trapped using a 980 nm CW laser on a different setup and immediately moved to the fs-trap setup where it was unable to be trapped. Some things that must be considered are the thermophoretic effects of using a pulse laser and the time scales of plasmonic processes. We have hypothesized in CW trapping that increasing temperature hinders trapping time, and with much higher peak powers, the local temperature increase will be significantly higher. Ultrafast plasmonics is still an under researched field but we do know that the plasmon dephasing process is in the order of 10 fs-1ps [177] due to electron-electron and electron-surface scattering. More energy is dissipated on slower time scales due to electron-phonon relaxation (1-100ps) and phonon-phonon scattering (100 ps-10ns) [178, 179, 180]. Since we use the plasmon enhancement to generate much stronger gradient forces, when the delay pulse exceeds 1 ps, it can be assumed that there is no plasmonic field present and thus there are no forces acting on the nanoaperture during the delay period. It is unclear whether these timescales will truly impact trapping negatively, but it must be considered.

During my time at the Light-Matter Interactions Group at Okinawa Institute of Science and Technology, I was able to succeed in unstably trapping BSA using a 780 nm, femtosecond pulsed laser at 7 mW. There is a very narrow range of a minimum power needed to trap and a maximum power before the DNH is destroyed. We experienced that below 7 mW, trapping did not occur, and above 9 mW the DNH was destroyed. In this range, there is an even narrower range where the protein is trapped stably.

6.2 Concluding Remarks

Pulse laser trapping of proteins does seem to be possible, but much more work is needed to trap efficiently and reliably. Alternative nanostructures should be investigated to minimize heating, a thorough investigation of the powers available for trapping without damage needs to be done and an examination of the effect of wavelength as well. This holds tremendous promise for measuring ultrafast dynamics of proteins.

Chapter 7

Conclusions and Future Work

In this thesis, a review of single biomolecule techniques was presented, focusing on the interferometric methods of iSCAT, PSM, and NSM (Chapter 2). Following this, a review of optical tweezers and optical nanotweezers was shown (Chapter 2). In Chapter 3, a review of methods for fabricating DNHs, building, aligning, and using an optical tweezer, and the relevant data analysis (PSD, RMSD, computer vision) was introduced. In Chapter 4, we demonstrated the ability to image and track proteins as small as 14 kDa without fluorescence using plasmon-enhanced interference, with verification of single proteins through complementary optical nanotweezer measurements. The diffusion of the proteins is slower than expected from unconstrained 3D diffusion due to the proximity to the surface and plethora of forces acting on the protein. However, the result has major implications in enhancing interference signals through plasmons and charge-based effects on plasmonics. In chapter 5, we demonstrate the capabilities of using optical nanotweezers for classifying extracellular vesicles into their parent cells using a convolutional neural network trained only on optical scattering signals. While traditional analysis (PSD and RMSD) were unable to capture any differences between EVs, the CNN was able to identify features that arise from biomechanical differences in the EVs due to composition and geometry. We achieve a greater than 90% accuracy in classifying a trapped EV into non-malignant, non-invasive cancerous, and invasive cancerous. In Chapter 6, I show other work performed during my master's. First, I present efforts to trap a single protein with a femtosecond laser for applications in vibrational spectroscopy, but was unsuccessful for the reasons outlined. Second, I present work deriving a solution to the surface

plasmon propagation length using perturbation theory, incorporating quantum effects. The results of this showed no difference between the standard definition of the propagation length and added quantum effects.

In the future, theoretical work on charge-plasmon effects needs to be studied and modifying the substrate to allow for widefield, unconstrained tracking of single proteins. This could be achieved through metasurfaces or a thin gold film modified nanochannel. Future work with extracellular vesicles should move towards working in 'dirty' samples, where a mix of EVs from different cell lines are trapped, with the goal of identifying the composition of the solution. Furthermore, it should be shown that it is possible to identify cancer derived EVs despite only being present in a much smaller ratio than healthy EVs.

Bibliography

[1] W. Yu, W. C. Jiang, Q. Lin, and T. Lu, "Cavity optomechanical spring sensing of single molecules," *Nature communications*, vol. 7, no. 1, p. 12311, 2016.

[2] Y. Pang and R. Gordon, "Optical trapping of a single protein," *Nano Letters*, vol. 12, no. 1, pp. 402–406, 2012.

[3] S. Wheaton and R. Gordon, "Molecular weight characterization of single globular proteins using optical nanotweezers," *Analyst*, vol. 140, no. 14, pp. 4799–4803, 2015.

[4] E. Babaei, D. Wright, and R. Gordon, "Fringe dielectrophoresis nanoaperture optical trapping with order of magnitude speed-up for unmodified proteins," *Nano Letters*, vol. 23, no. 7, pp. 2877–2882, 2023.

[5] M. Piliarik and V. Sandoghdar, "Direct optical sensing of single unlabelled proteins and super-resolution imaging of their binding sites," *Nature Communications*, vol. 5, no. 1, p. 4495, 2014.

[6] M. Liebel, J. T. Hugall, and N. F. Van Hulst, "Ultrasensitive label-free nanosensing and high-speed tracking of single proteins," *Nano Letters*, vol. 17, no. 2, pp. 1277–1281, 2017.

[7] G. Young, N. Hundt, D. Cole, A. Fineberg, J. Andrecka, A. Tyler, A. Olerinyova, A. Ansari, E. G. Marklund, M. P. Collier, S. A. Chandler, O. Tkachenko, J. Allen, M. Crispin, N. Billington, Y. Takagi, J. R. Sellers, C. Eichmann, P. Selenko, L. Frey, R. Riek, M. R. Galpin, W. B. Struwe, J. L. P. Benesch, and P. Kukura, "Quantitative mass imaging of single biological macromolecules," *Science*, vol. 360, no. 6387, pp. 423–427, 2018.

[8] B. Hajdusits, M. J. Suskiewicz, N. Hundt, A. Meinhart, R. Kurzbauer, J. Leodolter, P. Kukura, and T. Clausen, "Mcsb forms a gated kinase chamber to mark aberrant bacterial proteins for degradation," *Elife*, vol. 10, p. e63505, 2021.

[9] M. Dahmardeh, H. Mirzaalian Dastjerdi, H. Mazal, H. Köstler, and V. Sandoghdar, "Self-supervised machine learning pushes the sensitivity limit in label-free detection of single proteins below 10 kda," *Nature Methods*, vol. 20, no. 3, pp. 442–447, 2023.

[10] P. Zhang, G. Ma, W. Dong, Z. Wan, S. Wang, and N. Tao, "Plasmonic scattering imaging of single proteins and binding kinetics," *Nature Methods*, vol. 17, no. 10, pp. 1010–1017, 2020.

[11] Z. Wan, G. Ma, P. Zhang, and S. Wang, "Single-protein identification by simultaneous size and charge imaging using evanescent scattering microscopy," *ACS Sensors*, vol. 7, no. 9, pp. 2625–2633, 2022.

[12] G. Ma, Z. Wan, Y. Yang, P. Zhang, S. Wang, and N. Tao, "Optical imaging of single-protein size, charge, mobility, and binding," *Nature Communications*, vol. 11, no. 1, p. 4768, 2020.

[13] B. Špačková, H. Klein Moberg, J. Fritzsche, J. Tenghamn, G. Sjösten, H. Šípová-Jungová, D. Albinsson, Q. Lubart, D. van Leeuwen, F. Westerlund, D. Midtvedt, E. K. Esbjörner, M. Käll, G. Volpe, and C. Langhammer, "Label-free nanofluidic scattering microscopy of size and mass of single diffusing molecules and nanoparticles," *Nature Methods*, vol. 19, no. 6, pp. 751–758, 2022.

[14] M. Peters, D. McIntosh, A. Branzan Albu, C. Ying, and R. Gordon, "Label-free tracking of proteins through plasmon-enhanced interference," *ACS Nanoscience Au*, 2023.

[15] F. Liang, Y. Guo, S. Hou, and Q. Quan, "Photonic-plasmonic hybrid single-molecule nanosensor measures the effect of fluorescent labels on dna-protein dynamics," *Science Advances*, vol. 3, no. 5, p. e1602991, 2017.

[16] E. Kim, M. D. Baaske, I. Schuldes, P. S. Wilsch, and F. Vollmer, "Label-free optical detection of single enzyme-reactant reactions and associated conforma-

tional changes," *Science Advances*, vol. 3, no. 3, p. e1603044, 2017.

[17] N. A. Toropov, M. C. Houghton, D. Yu, and F. Vollmer, "Thermo-optoplasmonic single-molecule sensing on optical microcavities," *bioRxiv*, pp. 2023–12, 2023.

[18] M. D. Baaske, M. R. Foreman, and F. Vollmer, "Single-molecule nucleic acid interactions monitored on a label-free microcavity biosensor platform," *Nature nanotechnology*, vol. 9, no. 11, pp. 933–939, 2014.

[19] J. C. Thiele, E. Pfitzner, and P. Kukura, "Single-protein optical holography," *bioRxiv*, pp. 2023–08, 2023.

[20] L.-M. Needham, C. Saavedra, J. K. Rasch, D. Sole-Barber, B. S. Schweitzer, A. J. Fairhall, C. H. Vollbrecht, S. Wan, Y. Podorova, A. J. Bergsten, *et al.*, "Label-free detection and profiling of individual solution-phase molecules," *Nature*, pp. 1–7, 2024.

[21] U. Consortium, "Uniprot: a worldwide hub of protein knowledge," *Nucleic Acids Research*, vol. 47, no. D1, pp. D506–D515, 2019.

[22] W. Moerner and D. P. Fromm, "Methods of single-molecule fluorescence spectroscopy and microscopy," *Review of Scientific Instruments*, vol. 74, no. 8, pp. 3597–3619, 2003.

[23] K. N. Fish, "Total internal reflection fluorescence (tirf) microscopy," *Current Protocols in Cytometry*, vol. 50, no. 1, pp. 12–18, 2009.

[24] Y. Zhang, K.-Y. Park, K. F. Suazo, and M. D. Distefano, "Recent progress in enzymatic protein labelling techniques and their applications," *Chemical Society Reviews*, vol. 47, no. 24, pp. 9106–9136, 2018.

[25] S. Nie, D. T. Chiu, and R. N. Zare, "Real-time detection of single molecules in solution by confocal fluorescence microscopy," *Analytical Chemistry*, vol. 67, no. 17, pp. 2849–2857, 1995.

[26] H. Mazal and G. Haran, "Single-molecule fret methods to study the dynamics of proteins at work," *Current Opinion in Biomedical Engineering*, vol. 12, pp. 8–17, 2019.

[27] S. Spindler, J. Ehrig, K. König, T. Nowak, M. Piliarik, H. E. Stein, R. W. Taylor, E. Garanger, S. Lecommandoux, I. D. Alves, *et al.*, "Visualization of lipids and proteins at high spatial and temporal resolution via interferometric scattering (iscat) microscopy," *Journal of Physics D: Applied Physics*, vol. 49, no. 27, p. 274002, 2016.

[28] Y. S. Hu, M. Zimmerley, Y. Li, R. Watters, and H. Cang, "Single-molecule super-resolution light-sheet microscopy," *ChemPhysChem*, vol. 15, no. 4, pp. 577–586, 2014.

[29] B. Špačková, H. Klein Moberg, J. Fritzsche, J. Tenghamn, G. Sjösten, H. Šípová-Jungová, D. Albinsson, Q. Lubart, D. van Leeuwen, F. Westerlund, D. Midtvedt, E. K. Esbjörner, M. Käll, G. Volpe, and C. Langhammer, "Label-free nanofluidic scattering microscopy of size and mass of single diffusing molecules and nanoparticles," *Nature Methods*, vol. 19, no. 6, pp. 751–758, 2022.

[30] O. Ozohanics and A. Ambrus, "Hydrogen-deuterium exchange mass spectrometry: A novel structural biology approach to structure, dynamics and interactions of proteins and their complexes," *Life*, vol. 10, no. 11, p. 286, 2020.

[31] Z. Movasaghi, S. Rehman, and D. I. ur Rehman, "Fourier transform infrared (ftir) spectroscopy of biological tissues," *Applied Spectroscopy Reviews*, vol. 43, no. 2, pp. 134–179, 2008.

[32] K. Wüthrich, "Nmr with proteins and nucleic acids," *Europhysics News*, vol. 17, no. 1, pp. 11–13, 1986.

[33] E. Abbe, "Contributions to the theory of the microscope and that microscopic perception," *Arch. Microsc. Anat*, vol. 9, pp. 413–468, 1873.

[34] S. W. Hell, "Nanoscopy with focused light (nobel lecture)," *Angewandte Chemie International Edition*, vol. 54, no. 28, pp. 8054–8066, 2015.

[35] R. Henriques, C. Griffiths, E. Hesper Rego, and M. M. Mhlanga, "Palm and storm: unlocking live-cell super-resolution," *Biopolymers*, vol. 95, no. 5, pp. 322–331, 2011.

[36] P. Y. Li, B. Lin, J. Gerstenmaier, and B. T. Cunningham, "A new method for label-free imaging of biomolecular interactions," *Sensors and Actuators B: Chemical*, vol. 99, no. 1, pp. 6–13, 2004.

[37] J. Ortega-Arroyo and P. Kukura, "Interferometric scattering microscopy (iscat): new frontiers in ultrafast and ultrasensitive optical microscopy," *Physical Chemistry Chemical Physics*, vol. 14, no. 45, pp. 15625–15636, 2012.

[38] Z.-l. Li and M. Buck, "Beyond history and "on a roll": The list of the most well-studied human protein structures and overall trends in the protein data bank," *Protein Science*, vol. 30, no. 4, pp. 745–760, 2021.

[39] P. Zhang, R. Wang, Z. Wan, X. Zhou, G. Ma, J. Kolay, J. Jiang, and S. Wang, "Label-free imaging of single proteins and binding kinetics using total internal reflection-based evanescent scattering microscopy," *Analytical Chemistry*, vol. 94, no. 30, pp. 10781–10787, 2022.

[40] P. Zhang, G. Ma, Z. Wan, and S. Wang, "Quantification of single-molecule protein binding kinetics in complex media with prism-coupled plasmonic scattering imaging," *ACS Sensors*, vol. 6, no. 3, pp. 1357–1366, 2021.

[41] P. Zhang, L. Zhou, R. Wang, X. Zhou, J. Jiang, Z. Wan, and S. Wang, "Evanescent scattering imaging of single protein binding kinetics and dna conformation changes," *Nature Communications*, vol. 13, no. 1, p. 2298, 2022.

[42] S. Chu, "Observation of a single-beam gradient force optical trap for dielectric particles," *Optics Letters*, vol. 11, no. 5, pp. 288–290, 1986.

[43] A. Ashkin and J. M. Dziedzic, "Optical trapping and manipulation of viruses and bacteria," *Science*, vol. 235, no. 4795, pp. 1517–1520, 1987.

[44] A. Ashkin, J. M. Dziedzic, and T. Yamane, "Optical trapping and manipulation of single cells using infrared laser beams," *Nature*, vol. 330, no. 6150, pp. 769–771, 1987.

[45] Y. Pang, *Nanophotonics with subwavelength apertures: theories and applications.* PhD thesis, 2012.

[46] C. J. Bustamante, Y. R. Chemla, S. Liu, and M. D. Wang, "Optical tweezers in single-molecule biophysics," *Nature Reviews Methods Primers*, vol. 1, no. 1, p. 25, 2021.

[47] K. J. Laidler, J. H. Meiser, and B. C. Sanctuary, "Physical chemistry," *(No Title)*, 2003.

[48] S. M. Block, L. S. Goldstein, and B. J. Schnapp, "Bead movement by single kinesin molecules studied with optical tweezers," *Nature*, vol. 348, no. 6299, pp. 348–352, 1990.

[49] M. D. Wang, H. Yin, R. Landick, J. Gelles, and S. M. Block, "Stretching dna with optical tweezers," *Biophysical Journal*, vol. 72, no. 3, pp. 1335–1346, 1997.

[50] P. T. Li, C. Bustamante, and I. Tinoco Jr, "Real-time control of the energy landscape by force directs the folding of rna molecules," *Proceedings of the National Academy of Sciences*, vol. 104, no. 17, pp. 7039–7044, 2007.

[51] L. Bongini, L. Melli, V. Lombardi, and P. Bianco, "Transient kinetics measured with force steps discriminate between double-stranded dna elongation and melting and define the reaction energetics," *Nucleic Acids Research*, vol. 42, no. 5, pp. 3436–3449, 2014.

[52] A. Mossa, M. Manosas, N. Forns, J. M. Huguet, and F. Ritort, "Dynamic force spectroscopy of dna hairpins: I. force kinetics and free energy landscapes," *Journal of Statistical Mechanics: Theory and Experiment*, vol. 2009, no. 02, p. P02060, 2009.

[53] S. B. Smith, Y. Cui, and C. Bustamante, "Overstretching b-dna: the elastic response of individual double-stranded and single-stranded dna molecules," *Science*, vol. 271, no. 5250, pp. 795–799, 1996.

[54] M. Caldarini, P. Sonar, I. Valpapuram, D. Tavella, C. Volonté, V. Pandini, M. Vanoni, A. Aliverti, R. Broglia, G. Tiana, *et al.*, "The complex folding behavior of hiv-1-protease monomer revealed by optical-tweezer single-molecule experiments and molecular dynamics simulations," *Biophysical Chemistry*, vol. 195, pp. 32–42, 2014.

[55] P. Bechtluft, R. G. Van Leeuwen, M. Tyreman, D. Tomkiewicz, N. Nouwen, H. L. Tepper, A. J. Driessen, and S. J. Tans, "Direct observation of chaperone-induced changes in a protein folding pathway," *Science*, vol. 318, no. 5855, pp. 1458–1461, 2007.

[56] M. Jahn, K. Tych, H. Girstmair, M. Steinmaßl, T. Hugel, J. Buchner, and M. Rief, "Folding and domain interactions of three orthologs of hsp90 studied by single-molecule force spectroscopy," *Structure*, vol. 26, no. 1, pp. 96–105, 2018.

[57] P. O. Heidarsson, M. M. Naqvi, M. R. Otazo, A. Mossa, B. B. Kragelund, and C. Cecconi, "Direct single-molecule observation of calcium-dependent misfolding in human neuronal calcium sensor-1," *Proceedings of the National Academy of Sciences*, vol. 111, no. 36, pp. 13069–13074, 2014.

[58] M. L. Juan, R. Gordon, Y. Pang, F. Eftekhari, and R. Quidant, "Self-induced back-action optical trapping of dielectric nanoparticles," *Nature Physics*, vol. 5, no. 12, pp. 915–919, 2009.

[59] Y. Pang and R. Gordon, "Optical trapping of 12 nm dielectric spheres using double-nanoholes in a gold film," *Nano Letters*, vol. 11, no. 9, pp. 3763–3767, 2011.

[60] L. Rayleigh, "Xviii. on the passage of electric waves through tubes, or the vibrations of dielectric cylinders," *The London, Edinburgh, and Dublin Philosophical Magazine and Journal of Science*, vol. 43, no. 261, pp. 125–132, 1897.

[61] H. A. Bethe, "Theory of diffraction by small holes," *Physical Review*, vol. 66, no. 7-8, p. 163, 1944.

[62] T. W. Ebbesen, H. J. Lezec, H. Ghaemi, T. Thio, and P. A. Wolff, "Extraordinary optical transmission through sub-wavelength hole arrays," *Nature*, vol. 391, no. 6668, pp. 667–669, 1998.

[63] R. Gordon and A. G. Brolo, "Increased cut-off wavelength for a subwavelength hole in a real metal," *Optics Express*, vol. 13, no. 6, pp. 1933–1938, 2005.

[64] J. D. Kolbow, N. C. Lindquist, C. T. Ertsgaard, D. Yoo, and S.-H. Oh, "Nano-optical tweezers: Methods and applications for trapping single molecules and

nanoparticles," *ChemPhysChem*, vol. 22, no. 14, pp. 1409–1420, 2021.

[65] C. Wen, E. Bertosin, X. Shi, C. Dekker, and S. Schmid, "Orientation-locked dna origami for stable trapping of small proteins in the nanopore electro-osmotic trap," *Nano Letters*, vol. 23, no. 3, pp. 788–794, 2022.

[66] A. Kotnala and R. Gordon, "Quantification of high-efficiency trapping of nanoparticles in a double nanohole optical tweezer," *Nano Letters*, vol. 14, no. 2, pp. 853–856, 2014.

[67] A. L. Ravindranath, M. S. Shariatdoust, S. Mathew, and R. Gordon, "Colloidal lithography double-nanohole optical trapping of nanoparticles and proteins," *Optics Express*, vol. 27, no. 11, pp. 16184–16194, 2019.

[68] Q. Jiang, B. Rogez, J.-B. Claude, A. Moreau, J. Lumeau, G. Baffou, and J. Wenger, "Adhesion layer influence on controlling the local temperature in plasmonic gold nanoholes," *Nanoscale*, vol. 12, no. 4, pp. 2524–2531, 2020.

[69] A. Yousefi, Z. Zheng, S. Zargarbashi, M. Assadipapari, G. J. Hickman, C. D. Parmenter, C. J. Bueno-Alejo, G. Sanderson, D. Craske, L. Xu, *et al.*, "Structural flexibility and disassembly kinetics of single ferritin molecules using optical nanotweezers," *ACS Nano*, 2024.

[70] A. Yousefi, C. Ying, C. D. Parmenter, M. Assadipapari, G. Sanderson, Z. Zheng, L. Xu, S. Zargarbashi, G. J. Hickman, R. B. Cousins, C. J. Mellor, M. Mayer, and M. Rahmani, "Optical monitoring of in situ iron loading into single, native ferritin proteins," *Nano Letters*, vol. 23, no. 8, pp. 3251–3258, 2023.

[71] L. Chaparro and A. Akan, *Signals and Systems using MATLAB*. Academic Press, 2018.

[72] G. Danuser, "Computer vision in cell biology," *Cell*, vol. 147, no. 5, pp. 973–978, 2011.

[73] B. G. Weinstein, "A computer vision for animal ecology," *Journal of Animal Ecology*, vol. 87, no. 3, pp. 533–545, 2018.

[74] W. T. Freeman, K.-i. Tanaka, J. Ohta, and K. Kyuma, "Computer vision for computer games," in *Proceedings of the Second International Conference on Automatic Face and Gesture Recognition*, pp. 100–105, IEEE, 1996.

[75] L. Matthies, M. Maimone, A. Johnson, Y. Cheng, R. Willson, C. Villalpando, S. Goldberg, A. Huertas, A. Stein, and A. Angelova, "Computer vision on mars," *International Journal of Computer Vision*, vol. 75, pp. 67–92, 2007.

[76] Y. Ke, D. Hoiem, and R. Sukthankar, "Computer vision for music identification," in *2005 IEEE Computer Society Conference on Computer Vision and Pattern Recognition (CVPR'05)*, vol. 1, pp. 597–604, IEEE, 2005.

[77] P. Wiriyathammabhum, D. Summers-Stay, C. Fermüller, and Y. Aloimonos, "Computer vision and natural language processing: recent approaches in multimedia and robotics," *ACM Computing Surveys (CSUR)*, vol. 49, no. 4, pp. 1–44, 2016.

[78] C. Gilbert, "A computer programme for the analysis of human chromosomes," *Nature*, vol. 212, pp. 1437–1440, 1966.

[79] A. Farnoush, "The application of an image analyzing computer (quantimet 720) for quantitation of biological structures–the automatic counting of mast cells.," *Microscopica Acta*, vol. 80, no. 1, pp. 43–47, 1977.

[80] S. Y. Elhabian, K. M. El-Sayed, and S. H. Ahmed, "Moving object detection in spatial domain using background removal techniques-state-of-art," *Recent Patents on Computer Science*, vol. 1, no. 1, pp. 32–54, 2008.

[81] Z. Zivkovic, "Improved adaptive gaussian mixture model for background subtraction," in *Proceedings of the 17th International Conference on Pattern Recognition, 2004. ICPR 2004.*, vol. 2, pp. 28–31, IEEE, 2004.

[82] U. Kubitscheck, *Fluorescence microscopy: from principles to biological applications*. New Jersey: John Wiley & Sons, 2017.

[83] M. Quinn, N. Gnan, S. James, A. Ninarello, F. Sciortino, E. Zaccarelli, and J. McManus, "How fluorescent labelling alters the solution behaviour of proteins," *Physical Chemistry Chemical Physics*, vol. 17, no. 46, pp. 31177–31187, 2015.

[84] A. Gajraj and R. Y. Ofoli, "Effect of extrinsic fluorescent labels on diffusion and adsorption kinetics of proteins at the liquid- liquid interface," *Langmuir*, vol. 16, no. 21, pp. 8085–8094, 2000.

[85] S. Bingaman, V. H. Huxley, and R. E. Rumbaut, "Fluorescent dyes modify properties of proteins used in microvascular research," *Microcirculation*, vol. 10, no. 2, pp. 221–231, 2003.

[86] M. Kim, J. C. Foster, M. D. Moore, and M. Chen, "Improving single-molecule antibody detection selectivity through optimization of peptide epitope presentation in ompg nanopore," *ACS Sensors*, vol. 8, no. 7, pp. 2673–2680, 2023.

[87] L. S. Booth, E. V. Browne, N. P. Mauranyapin, L. S. Madsen, S. Barfoot, A. Mark, and W. P. Bowen, "Modelling of the dynamic polarizability of macromolecules for single-molecule optical biosensing," *Scientific Reports*, vol. 12, no. 1, p. 1995, 2022.

[88] J. Ortega Arroyo, J. Andrecka, K. Spillane, N. Billington, Y. Takagi, J. Sellers, and P. Kukura, "Label-free, all-optical detection, imaging, and tracking of a single protein," *Nano Letters*, vol. 14, no. 4, pp. 2065–2070, 2014.

[89] E. D. Foley, M. S. Kushwah, G. Young, and P. Kukura, "Mass photometry enables label-free tracking and mass measurement of single proteins on lipid bilayers," *Nature Methods*, vol. 18, no. 10, pp. 1247–1252, 2021.

[90] D. Cole, G. Young, A. Weigel, A. Sebesta, and P. Kukura, "Label-free single-molecule imaging with numerical-aperture-shaped interferometric scattering microscopy," *ACS Photonics*, vol. 4, no. 2, pp. 211–216, 2017.

[91] M. P. McDonald, A. Gemeinhardt, K. König, M. Piliarik, S. Schaffer, S. Völkl, M. Aigner, A. Mackensen, and V. Sandoghdar, "Visualizing single-cell secretion dynamics with single-protein sensitivity," *Nano Letters*, vol. 18, no. 1, pp. 513–519, 2018.

[92] P. Kukura, H. Ewers, C. Müller, A. Renn, A. Helenius, and V. Sandoghdar, "High-speed nanoscopic tracking of the position and orientation of a single virus," *Nature Methods*, vol. 6, no. 12, pp. 923–927, 2009.

[93] R. W. Taylor and V. Sandoghdar, "Interferometric scattering (iscat) microscopy and related techniques," in *Label-free super-resolution microscopy*, pp. 25–65, Springer, 2019.

[94] R. Gordon, "Biosensing with nanoaperture optical tweezers," *Optics & Laser Technology*, vol. 109, pp. 328–335, 2019.

[95] L. Neumeier, R. Quidant, and D. E. Chang, "Self-induced back-action optical trapping in nanophotonic systems," *New Journal of Physics*, vol. 17, no. 12, p. 123008, 2015.

[96] S. S. S. Peri, M. K. Sabnani, M. U. Raza, S. Ghaffari, S. Gimlin, D. D. Wawro, J. S. Lee, M. J. Kim, J. Weidanz, and G. Alexandrakis, "Detection of specific antibody-ligand interactions with a self-induced back-action actuated nanopore electrophoresis sensor," *Nanotechnology*, vol. 31, no. 8, p. 085502, 2019.

[97] C. Hong, S. Yang, and J. C. Ndukaife, "Stand-off trapping and manipulation of sub-10 nm objects and biomolecules using opto-thermo-electrohydrodynamic tweezers," *Nature Nanotechnology*, vol. 15, no. 11, pp. 908–913, 2020.

[98] D. Verschueren, X. Shi, and C. Dekker, "Nano-optical tweezing of single proteins in plasmonic nanopores," *Small Methods*, vol. 3, no. 5, p. 1800465, 2019.

[99] N. Mirkin, J. Jaconcic, V. Stojanoff, and A. Moreno, "High resolution x-ray crystallographic structure of bovine heart cytochrome c and its application to the design of an electron transfer biosensor," *Proteins: Structure, Function, and Bioinformatics*, vol. 70, no. 1, pp. 83–92, 2008.

[100] S. H. Hristova and A. M. Zhivkov, "Isoelectric point of free and adsorbed cytochrome c determined by various methods," *Colloids and Surfaces B: Biointerfaces*, vol. 174, pp. 87–94, 2019.

[101] V. La Verde, P. Dominici, and A. Astegno, "Determination of hydrodynamic radius of proteins by size exclusion chromatography," *Bio-protocol*, vol. 7, no. 8, pp. e2230–e2230, 2017.

[102] J. B. Feldstein and D. N. Silverman, "Purification and characterization of carbonic anhydrase from the saliva of the rat.," *Journal of Biological Chemistry*, vol. 259, no. 9, pp. 5447–5453, 1984.

[103] J. D. Harvey, R. Geddes, and P. R. Wills, "Conformational studies of bsa using laser light scattering," *Biopolymers: Original Research on Biomolecules*, vol. 18, no. 9, pp. 2249–2260, 1979.

[104] Q. Shi, Y. Zhou, and Y. Sun, "Influence of ph and ionic strength on the steric mass-action model parameters around the isoelectric point of protein," *Biotechnology Progress*, vol. 21, no. 2, pp. 516–523, 2005.

[105] D. Crosby, S. Bhatia, K. M. Brindle, L. M. Coussens, C. Dive, M. Emberton, S. Esener, R. C. Fitzgerald, S. S. Gambhir, P. Kuhn, *et al.*, "Early detection of cancer," *Science*, vol. 375, no. 6586, p. eaay9040, 2022.

[106] N. E. Navin, "Cancer genomics: one cell at a time," *Genome Biology*, vol. 15, no. 8, pp. 1–13, 2014.

[107] S. A. Joosse, T. M. Gorges, and K. Pantel, "Biology, detection, and clinical implications of circulating tumor cells," *EMBO Molecular Medicine*, vol. 7, no. 1, pp. 1–11, 2015.

[108] M. Yáñez-Mó, P. R.-M. Siljander, Z. Andreu, A. Bedina Zavec, F. E. Borràs, E. I. Buzas, K. Buzas, E. Casal, F. Cappello, J. Carvalho, *et al.*, "Biological properties of extracellular vesicles and their physiological functions," *Journal of Extracellular Vesicles*, vol. 4, no. 1, p. 27066, 2015.

[109] R. Xu, A. Rai, M. Chen, W. Suwakulsiri, D. W. Greening, and R. J. Simpson, "Extracellular vesicles in cancer—implications for future improvements in cancer care," *Nature Reviews Clinical Oncology*, vol. 15, no. 10, pp. 617–638, 2018.

[110] A. Möller and R. J. Lobb, "The evolving translational potential of small extracellular vesicles in cancer," *Nature Reviews Cancer*, vol. 20, no. 12, pp. 697–709, 2020.

[111] D. S. Chulpanova, K. V. Kitaeva, V. James, A. A. Rizvanov, and V. V. Solovyeva, "Therapeutic prospects of extracellular vesicles in cancer treatment," *Frontiers in Immunology*, vol. 9, p. 1534, 2018.

[112] M. S. Panagopoulou, A. W. Wark, D. J. Birch, and C. D. Gregory, "Phenotypic analysis of extracellular vesicles: a review on the applications of fluorescence," *Journal of Extracellular Vesicles*, vol. 9, no. 1, p. 1710020, 2020.

[113] I. Helwa, J. Cai, M. D. Drewry, A. Zimmerman, M. B. Dinkins, M. L. Khaled, M. Seremwe, W. M. Dismuke, E. Bieberich, W. D. Stamer, and Y. Liu, "A com-

parative study of serum exosome isolation using differential ultracentrifugation and three commercial reagents," *PLOS ONE*, vol. 12, no. 1, p. e0170628, 2017.

[114] A. Cheruvanky, H. Zhou, T. Pisitkun, J. B. Kopp, M. A. Knepper, P. S. Yuen, and R. A. Star, "Rapid isolation of urinary exosomal biomarkers using a nanomembrane ultrafiltration concentrator," *American Journal of Physiology-Renal Physiology*, vol. 292, no. 5, pp. F1657–F1661, 2007.

[115] B. J. Tauro, D. W. Greening, R. A. Mathias, H. Ji, S. Mathivanan, A. M. Scott, and R. J. Simpson, "Comparison of ultracentrifugation, density gradient separation, and immunoaffinity capture methods for isolating human colon cancer cell line lim1863-derived exosomes," *Methods*, vol. 56, no. 2, pp. 293–304, 2012.

[116] T. Soares Martins, J. Catita, I. Martins Rosa, O. AB da Cruz e Silva, and A. G. Henriques, "Exosome isolation from distinct biofluids using precipitation and column-based approaches," *PLOS ONE*, vol. 13, no. 6, p. e0198820, 2018.

[117] J. Wang, P. Ma, D. H. Kim, B.-F. Liu, and U. Demirci, "Towards microfluidic-based exosome isolation and detection for tumor therapy," *Nano Today*, vol. 37, p. 101066, 2021.

[118] N. Ludwig, T. L. Whiteside, and T. E. Reichert, "Challenges in exosome isolation and analysis in health and disease," *International Journal of Molecular Sciences*, vol. 20, no. 19, p. 4684, 2019.

[119] R. P. Carney, S. Hazari, M. Colquhoun, D. Tran, B. Hwang, M. S. Mulligan, J. D. Bryers, E. Girda, G. S. Leiserowitz, Z. J. Smith, and K. S. Lam, "Multispectral optical tweezers for biochemical fingerprinting of cd9-positive exosome subpopulations," *Analytical Chemistry*, vol. 89, no. 10, pp. 5357–5363, 2017.

[120] S. G. Kruglik, F. Royo, J.-M. Guigner, L. Palomo, O. Seksek, P.-Y. Turpin, I. Tatischeff, and J. M. Falcón-Pérez, "Raman tweezers microspectroscopy of circa 100 nm extracellular vesicles," *Nanoscale*, vol. 11, no. 4, pp. 1661–1679, 2019.

[121] D. Boateng, K. Chu, Z. J. Smith, J. Du, and Y. Dai, "Deep learning-based size prediction for optical trapped nanoparticles and extracellular vesicles from limited bandwidth camera detection," *Biomedical Optics Express*, vol. 15, no. 1, pp. 1–13, 2024.

[122] Q. Gao, P. Zang, J. Li, W. Zhang, Z. Zhang, C. Li, J. Yao, C. Li, Q. Yang, S. Li, Z. Guo, and Z. Lianqun, "Revealing the binding events of single proteins on exosomes using nanocavity antennas beyond zero-mode waveguides," *ACS Applied Materials & Interfaces*, vol. 15, no. 42, pp. 49511–49526, 2023.

[123] J. Min, T. Son, J.-S. Hong, P. S. Cheah, A. Wegemann, K. Murlidharan, R. Weissleder, H. Lee, and H. Im, "Plasmon-enhanced biosensing for multiplexed profiling of extracellular vesicles," *Advanced Biosystems*, vol. 4, no. 12, p. 2000003, 2020.

[124] J. Park, H. Im, S. Hong, C. M. Castro, R. Weissleder, and H. Lee, "Analyses of intravesicular exosomal proteins using a nano-plasmonic system," *ACS Photonics*, vol. 5, no. 2, pp. 487–494, 2018.

[125] E. L. Gool, I. Stojanovic, R. B. Schasfoort, A. Sturk, T. G. van Leeuwen, R. Nieuwland, L. W. Terstappen, and F. A. Coumans, "Surface plasmon resonance is an analytically sensitive method for antigen profiling of extracellular vesicles," *Clinical Chemistry*, vol. 63, no. 10, pp. 1633–1641, 2017.

[126] Y. Yang, C. Zhai, Q. Zeng, A. L. Khan, and H. Yu, "Multifunctional detection of extracellular vesicles with surface plasmon resonance microscopy," *Analytical Chemistry*, vol. 92, no. 7, pp. 4884–4890, 2020.

[127] C. Zhai, J. Long, J. He, Y. Zheng, B. Wang, J. Xu, Y. Yang, L. Jiang, H. Yu, and X. Ding, "Precise identification and profiling of surface proteins of ultra rare tumor specific extracellular vesicle with dynamic quantitative plasmonic imaging," *ACS Nano*, vol. 17, no. 17, pp. 16656–16667, 2023.

[128] D. Yoo, K. L. Gurunatha, H.-K. Choi, D. A. Mohr, C. T. Ertsgaard, R. Gordon, and S.-H. Oh, "Low-power optical trapping of nanoparticles and proteins with resonant coaxial nanoaperture using 10 nm gap," *Nano Letters*, vol. 18, no. 6, pp. 3637–3642, 2018.

[129] W. Yang, M. van Dijk, C. Primavera, and C. Dekker, "Fib-milled plasmonic nanoapertures allow for long trapping times of individual proteins," *iScience*, vol. 24, no. 11, 2021.

[130] J. Berthelot, S. S. Acimovic, M. L. Juan, M. P. Kreuzer, J. Renger, and R. Quidant, "Three-dimensional manipulation with scanning near-field optical

nanotweezers," *Nature Nanotechnology*, vol. 9, no. 4, pp. 295–299, 2014.

[131] R. A. Jensen, I.-C. Huang, O. Chen, J. T. Choy, T. S. Bischof, M. Loncar, and M. G. Bawendi, "Optical trapping and two-photon excitation of colloidal quantum dots using bowtie apertures," *ACS Photonics*, vol. 3, no. 3, pp. 423–427, 2016.

[132] S. Kerman, C. Chen, Y. Li, W. Van Roy, L. Lagae, and P. Van Dorpe, "Raman fingerprinting of single dielectric nanoparticles in plasmonic nanopores," *Nanoscale*, vol. 7, no. 44, pp. 18612–18618, 2015.

[133] M. U. Raza, S. S. S. Peri, L.-C. Ma, S. M. Iqbal, and G. Alexandrakis, "Self-induced back action actuated nanopore electrophoresis (sane)," *Nanotechnology*, vol. 29, no. 43, p. 435501, 2018.

[134] A. Kotnala, P. S. Kollipara, J. Li, and Y. Zheng, "Overcoming diffusion-limited trapping in nanoaperture tweezers using opto-thermal-induced flow," *Nano Letters*, vol. 20, no. 1, pp. 768–779, 2019.

[135] S. J. Yoon, D. I. Song, J. Lee, M.-K. Kim, Y.-H. Lee, and C.-K. Kim, "Hopping of single nanoparticles trapped in a plasmonic double-well potential," *Nanophotonics*, vol. 9, no. 16, pp. 4729–4735, 2020.

[136] Q. Jiang, B. Rogez, J.-B. Claude, G. Baffou, and J. Wenger, "Quantifying the role of the surfactant and the thermophoretic force in plasmonic nano-optical trapping," *Nano Letters*, vol. 20, no. 12, pp. 8811–8817, 2020.

[137] D. G. Kotsifaki, V. G. Truong, and S. N. Chormaic, "Fano-resonant, asymmetric, metamaterial-assisted tweezers for single nanoparticle trapping," *Nano Letters*, vol. 20, no. 5, pp. 3388–3395, 2020.

[138] B. Wu, Y. Lou, D. Wu, Q. Min, X. Wan, H. Zhang, Y. Yu, J. Ma, G. Si, and Y. Pang, "Directivity-enhanced detection of a single nanoparticle using a plasmonic slot antenna," *Nano Letters*, vol. 22, no. 6, pp. 2374–2380, 2022.

[139] C. Hong and J. C. Ndukaife, "Scalable trapping of single nanosized extracellular vesicles using plasmonics," *Nature Communications*, vol. 14, no. 1, pp. 4601(1–8), 2023.

[140] I. Hong, C. Hong, O. S. Tutanov, C. Massick, M. Castleberry, Q. Zhang, D. K. Jeppesen, J. N. Higginbotham, J. L. Franklin, K. Vickers, R. J. Coffey, and J. C. Ndukaife, "Anapole-assisted low-power optical trapping of nanoscale extracellular vesicles and particles," *Nano Letters*, vol. 23, no. 16, pp. 7500–7507, 2023.

[141] C. Hong, S. Yang, and J. C. Ndukaife, "Exosomes trapping, manipulation and size-based separation using opto-thermo-electrohydrodynamic tweezers," *Nanoscale Advances*, vol. 5, no. 11, pp. 2973–2978, 2023.

[142] G. Hajisalem, E. Babaei, M. Dobinson, S. Iwamoto, Z. Sharifi, J. Eby, M. Synakewicz, L. S. Itzhaki, and R. Gordon, "Accessible high-performance double nanohole tweezers," *Optics Express*, vol. 30, no. 3, pp. 3760–3769, 2022.

[143] L. Rikkert, P. Beekman, J. Caro, F. Coumans, A. Enciso-Martinez, G. Jenster, S. Le Gac, W. Lee, T. G. Van Leeuwen, G. Loozen, *et al.*, "Cancer-id: toward identification of cancer by tumor-derived extracellular vesicles in blood," *Frontiers in Oncology*, vol. 10, p. 608, 2020.

[144] C. Gardiner, M. Shaw, P. Hole, J. Smith, D. Tannetta, C. W. Redman, and I. L. Sargent, "Measurement of refractive index by nanoparticle tracking analysis reveals heterogeneity in extracellular vesicles," *Journal of Extracellular Vesicles*, vol. 3, no. 1, p. 25361, 2014.

[145] P. Apell and Å. Ljungbert, "Red shift of surface plasmons in small metal particles," *Solid State Communications*, vol. 44, no. 9, pp. 1367–1369, 1982.

[146] X. Shan, S. Wang, and N. Tao, "Study of single particle charge and brownian motions with surface plasmon resonance," *Applied Physics Letters*, vol. 97, no. 22, 2010.

[147] H. Šípová-Jungová, L. Jurgová, K. Mrkvová, N. S. Lynn, B. Špačková, and J. Homola, "Biomolecular charges influence the response of surface plasmon resonance biosensors through electronic and ionic mechanisms," *Biosensors and Bioelectronics*, vol. 126, pp. 365–372, 2019.

[148] I. I. Hosseini, Z. Liu, X. Capaldi, T. AbdelFatah, L. Montermini, J. Rak, W. Reisner, and S. Mahshid, "Nanofluidics for simultaneous size and charge

profiling of extracellular vesicles," *Nano Letters*, vol. 21, no. 12, pp. 4895–4902, 2021.

[149] T. Akagi and T. Ichiki, "Evaluation of zeta-potential of individual exosomes secreted from biological cells using a microcapillary electrophoresis chip," *Encyclopedia of Biocolloid and Biointerface Science 2V Set*, pp. 469–473, 2016.

[150] A. Uthamacumaran, M. Abdouh, K. Sengupta, Z.-h. Gao, S. Forte, T. Tsering, J. V. Burnier, and G. Arena, "Machine intelligence-driven classification of cancer patients-derived extracellular vesicles using fluorescence correlation spectroscopy: results from a pilot study," *Neural Computing and Applications*, vol. 35, no. 11, pp. 8407–8422, 2023.

[151] J. Zhao, C. Bai, Z. Zhang, and Q. Zhang, "Deep learning-based method for analyzing the optically trapped sperm rotation," *Scientific Reports*, vol. 13, no. 1, p. 12575, 2023.

[152] D. Zhang and M. R. Kabuka, "Protein family classification from scratch: a cnn based deep learning approach," *IEEE/ACM Transactions on Computational Biology and Bioinformatics*, vol. 18, no. 5, pp. 1996–2007, 2020.

[153] G. Lo Bosco and M. A. Di Gangi, "Deep learning architectures for dna sequence classification," in *Fuzzy Logic and Soft Computing Applications: 11th International Workshop, WILF 2016, Naples, Italy, December 19–21, 2016, Revised Selected Papers 11*, pp. 162–171, Springer, 2017.

[154] S. Kiranyaz, T. Ince, R. Hamila, and M. Gabbouj, "Convolutional neural networks for patient-specific ecg classification," in *2015 37th Annual International Conference of the IEEE Engineering in Medicine and Biology Society (EMBC)*, pp. 2608–2611, IEEE, 2015.

[155] S. Kiranyaz, T. Ince, and M. Gabbouj, "Real-time patient-specific ecg classification by 1-d convolutional neural networks," *IEEE Transactions on Biomedical Engineering*, vol. 63, no. 3, pp. 664–675, 2015.

[156] O. Avci, O. Abdeljaber, S. Kiranyaz, B. Boashash, H. Sodano, and D. J. Inman, "Efficiency validation of one dimensional convolutional neural networks for structural damage detection using a shm benchmark data," in *Proc. 25th Int. Conf. Sound Vib.(ICSV)*, pp. 4600–4607, 2018.

[157] O. Abdeljaber, O. Avci, M. S. Kiranyaz, B. Boashash, H. Sodano, and D. J. Inman, "1-d cnns for structural damage detection: Verification on a structural health monitoring benchmark data," *Neurocomputing*, vol. 275, pp. 1308–1317, 2018.

[158] S. Kiranyaz, A. Gastli, L. Ben-Brahim, N. Al-Emadi, and M. Gabbouj, "Real-time fault detection and identification for mmc using 1-d convolutional neural networks," *IEEE Transactions on Industrial Electronics*, vol. 66, no. 11, pp. 8760–8771, 2018.

[159] A. Javidani and A. Mahmoudi-Aznaveh, "Learning representative temporal features for action recognition," *Multimedia Tools and Applications*, vol. 81, no. 3, pp. 3145–3163, 2022.

[160] N. Salmond, K. Khanna, G. R. Owen, and K. C. Williams, "Nanoscale flow cytometry for immunophenotyping and quantitating extracellular vesicles in blood plasma," *Nanoscale*, vol. 13, no. 3, pp. 2012–2025, 2021.

[161] G. C. Brittain IV, Y. Q. Chen, E. Martinez, V. A. Tang, T. M. Renner, M.-A. Langlois, and S. Gulnik, "A novel semiconductor-based flow cytometer with enhanced light-scatter sensitivity for the analysis of biological nanoparticles," *Scientific Reports*, vol. 9, no. 1, p. 16039, 2019.

[162] A. Morales-Kastresana, B. Telford, T. A. Musich, K. McKinnon, C. Clayborne, Z. Braig, A. Rosner, T. Demberg, D. C. Watson, T. S. Karpova, G. J. Freeman, R. H. DeKruyff, G. N. Pavlakis, M. Terabe, M. Robert-Guroff, J. A. Berzofsky, and J. C. Jone, "Labeling extracellular vesicles for nanoscale flow cytometry," *Scientific Reports*, vol. 7, no. 1, p. 1878, 2017.

[163] K. Ito, Y. Ogawa, K. Yokota, S. Matsumura, T. Minamisawa, K. Suga, K. Shiba, Y. Kimura, A. Hirano-Iwata, Y. Takamura, *et al.*, "Host cell prediction of exosomes using morphological features on solid surfaces analyzed by machine learning," *The Journal of Physical Chemistry B*, vol. 122, no. 23, pp. 6224–6235, 2018.

[164] S. Ferguson and R. Weissleder, "Modeling ev kinetics for use in early cancer detection," *Advanced Biosystems*, vol. 4, no. 12, p. 1900305, 2020.

[165] A. Yekula, K. Muralidharan, K. M. Kang, L. Wang, L. Balaj, and B. S. Carter, "From laboratory to clinic: Translation of extracellular vesicle based cancer biomarkers," *Methods*, vol. 177, pp. 58–66, 2020.

[166] N. F. Zhang, "Allan variance of time series models for measurement data," *Metrologia*, vol. 45, no. 5, p. 549, 2008.

[167] N. Hacohen, C. J. Ip, and R. Gordon, "Analysis of egg white protein composition with double nanohole optical tweezers," *ACS Omega*, vol. 3, no. 5, pp. 5266–5272, 2018.

[168] Q. Jiang, B. Rogez, J.-B. Claude, G. Baffou, and J. Wenger, "Temperature measurement in plasmonic nanoapertures used for optical trapping," *ACS Photonics*, vol. 6, no. 7, pp. 1763–1773, 2019.

[169] H. Xu, X. Zheng, and X. Shi, "Surface hydrophilicity-mediated migration of nano/microparticles under temperature gradient in a confined space," *Journal of Colloid and Interface Science*, vol. 637, pp. 489–499, 2023.

[170] C. Gardiner, Y. J. Ferreira, R. A. Dragovic, C. W. Redman, and I. L. Sargent, "Extracellular vesicle sizing and enumeration by nanoparticle tracking analysis," *Journal of Extracellular Vesicles*, vol. 2, no. 1, p. 19671, 2013.

[171] D. N. Sathyanarayana, *Vibrational spectroscopy: theory and applications*. New Age International, 2015.

[172] S. Wheaton, R. M. Gelfand, and R. Gordon, "Probing the raman-active acoustic vibrations of nanoparticles with extraordinary spectral resolution," *Nature Photonics*, vol. 9, no. 1, pp. 68–72, 2015.

[173] A. K. De, D. Roy, A. Dutta, and D. Goswami, "Stable optical trapping of latex nanoparticles with ultrashort pulsed illumination," *Applied Optics*, vol. 48, no. 31, pp. G33–G37, 2009.

[174] Y. Jiang, T. Narushima, and H. Okamoto, "Nonlinear optical effects in trapping nanoparticles with femtosecond pulses," *Nature Physics*, vol. 6, no. 12, pp. 1005–1009, 2010.

[175] B. J. Roxworthy and K. C. Toussaint Jr, "Femtosecond-pulsed plasmonic nanotweezers," *Scientific Reports*, vol. 2, no. 1, p. 660, 2012.

[176] T. Shoji, J. Saitoh, N. Kitamura, F. Nagasawa, K. Murakoshi, H. Yamauchi, S. Ito, H. Miyasaka, H. Ishihara, and Y. Tsuboi, "Permanent fixing or reversible trapping and release of dna micropatterns on a gold nanostructure using continuous-wave or femtosecond-pulsed near-infrared laser light," *Journal of the American Chemical Society*, vol. 135, no. 17, pp. 6643–6648, 2013.

[177] A. N. Koya, M. Romanelli, J. Kuttruff, N. Henriksson, A. Stefancu, G. Grinblat, A. De Andres, F. Schnur, M. Vanzan, M. Marsili, *et al.*, "Advances in ultrafast plasmonics," *Applied Physics Reviews*, vol. 10, no. 2, 2023.

[178] M. Ahlawat, D. Mittal, and V. Govind Rao, "Plasmon-induced hot-hole generation and extraction at nano-heterointerfaces for photocatalysis," *Communications Materials*, vol. 2, no. 1, p. 114, 2021.

[179] C. Boerigter, U. Aslam, and S. Linic, "Mechanism of charge transfer from plasmonic nanostructures to chemically attached materials," *ACS nano*, vol. 10, no. 6, pp. 6108–6115, 2016.

[180] G. V. Hartland, "Optical studies of dynamics in noble metal nanostructures," *Chemical reviews*, vol. 111, no. 6, pp. 3858–3887, 2011.